Lattice Thermal Conductivities and Phonon Properties of FPU based Lattices and Graphene with Layers, Grain Boundaries and Strain

Submitted in partial fulfillment of the requirements

of the degree of

Doctor of Philosophy

by

Kunwar Abhikeern
(Roll No. 184106014)

Supervisor
Prof. Amit Singh

Department of Mechanical Engineering
INDIAN INSTITUTE OF TECHNOLOGY BOMBAY
2024

Dedicated to my advisor

Prof. Amit Singh

Dedicated to my *parents*

and *friends*

APPROVAL SHEET

This thesis entitled 'Lattice Thermal Conductivities and Phonon Properties of FPU based Lattices and Graphene with Layers, Grain Boundaries and Strain' by Kunwar Abhikeern is approved for the degree of Doctor of Philosophy.

Examiners

Abhishek Dhar.

Prof. Abhishek Dhar

Dasgupta

Prof. Titas Dasgupta

Supervisors

Amit Singh

Prof. Amit Singh

Chairperson

[signature]

Prof. Bhaskaran

Muralidharan

Date: 15/04/2025

Place: IIT Bombay, Mumbai

Declaration

I declare that this written submission represents my ideas in my own words, and where others' ideas or words have been included, I have adequately cited and referenced the original sources. I also declare that I have adhered to all principles of academic honesty and integrity and have not misrepresented or fabricated, or falsified any idea/data/fact /source in my submission. I understand that any violation of the above will cause disciplinary action by the Institute and can also evoke penal action from the sources which have thus not been properly cited or from whom proper permission has not been taken when needed.

Date:

_____

Kunwar Abhikeern

Roll No. 184106014

INDIAN INSTITUTE OF TECHNOLOGY BOMBAY, INDIA

CERTIFICATE OF COURSE WORK

This is to certify that **Kunwar Abhikeern** (Roll No. 184106014) was admitted to the candidacy of Ph.D. degree on 01 January 2019, after successfully completing all the courses required for the Ph.D. programme. The details of the course work done are given below.

S.No	Course Code	Course Name	Credits
1	ME 751	Mechanics of Deformable Bodies	6
2	MES 801	Seminar	4
3	MM 722	Molecular Simulations for Mateirals Engineering	6
4	HS 613	Finite Element and Boundary Element Methods	6
5	ME 775	Mechanisms in Crystal Plasticity	6
6	HS 791	Communication Skills -I	PP
7	HS 791	Communication Skills -II	PP
8	GC 101	Gender in the workplace	PP
9	ME 673	Mathematical Methods in Engineering	AU
10	ME 673	Introduction to Condensed Matter Physics I	AU
		Total Credits	**28**

IIT Bombay

Date: Dy. Registrar (Academic)

Abstract

In the field of graphene and other two-dimensional (2D) materials, significant progress has been made in understanding the thermal conductivity (TC) using various computational methods. Using nonequilibrium molecular dynamics (NEMD) based direct method and spectral energy density (SED) based normal mode decomposition (NMD) method, we calculate the size-dependent TCs of single layer graphene (SLG), AB-stacked bilayer graphene (AB-BLG) and $21.78°$ twisted BLG (tBLG) in a robust and consistent manner. Our NEMD analysis reveals discrepancies in the high TC reported for graphene systems in some of the earlier studies. Similarly, some of the previous NMD based studies were done with unreliable SED Φ' approach. We conduct size-dependent analysis of the graphene systems by the NMD method for the first time and report that bulk TCs for SLG and tBLG systems are nearly the same when calculated by either the direct or the NMD method. Contrary to studies which claim that phonon group velocities of AB-BLG and tBLG samples do not change, we find that although average group velocities in SLG and AB-BLG are almost the same but they are around 30% higher when compared to tBLG samples with different twist angles. On the other hand, average phonon lifetimes are almost similar for AB-BLG and $21.78°$ tBLG samples but around 43% lower than SLG's average phonon lifetime. Together these trends suggest the reason behind the decreasing order of TCs across three systems. We also systematically study the basic phonon mode contributions to TCs and their properties and find that the high-symmetry modes contribute the most in all three systems.

In one of the other studies using NMD method, we predict the phonon scattering mean lifetimes of polycrystalline graphene (PC-G) having polycrystallinity only along x-axis with seven different misorientation (tilt) angles at room temperature. Contrary to other studies on PC-G samples, our results indicate strong dependence of the TC on the tilt angles. We also show that the square of the group velocity components along x

and y axes and the phonon lifetimes are uncorrelated and the phonon density of states are almost the same for all samples with different tilt angles. Further, a distribution of the group velocity component along x or y axis as function of normal frequency is found to be exponentially decaying whereas that of phonon lifetime showed piecewise constant function behavior with respect to frequency. We provide parameters for these distribution functions and suggest another measure of the TC based on these distributions. Finally, we perform a size-dependent analysis for two tilt angles, $21.78°$ and $32.20°$, and find that bulk TC components decrease by around 34% to 62% in comparison to the bulk TC values of the pristine graphene. Our analysis reveals intriguing insights into the interplay between grain orientation, phonon scattering and TC in graphene.

In another related study, we investigated the impact of applied strain on the TC of SLG, with a focus on phonon behavior and energy transport mechanisms. Using NMD analysis, we decompose the phonon modes across the frequency spectrum to understand how strain affects thermal transport. Molecular dynamics (MD) simulations are conducted to calculate phonon group velocities, phonon lifetimes and TC for SLG under varying degrees of strain. The results reveal significant changes in the phonon dispersion curves, particularly for the out-of-plane acoustic (ZA) modes, which exhibit a shift from quadratic to linear behavior as strain increases. Additionally, the study shows a decrease in phonon group velocities with strain, while phonon lifetimes remain relatively unaffected. These findings provide insights into the scattering mechanisms and energy transport properties in strained graphene, offering valuable information for potential applications in nanoelectronics and thermal management systems.

Finally, in order to further deepen our understanding of thermal transport in real solids, a study was conducted to explore the use of the Fermi-Pasta-Ulam (FPU)-β potential model in examining TC in 2D materials. For the very first time this study investigates the thermal transport properties of 2D anharmonic solids using the FPU-β potential model, providing insights into the nonlinear phonon interactions that govern TC behavior. By employing a dual-method approach, comprising equilibrium molecular dynamics-based Green-Kubo (GK) analysis and the NMD method, we explain the mechanisms influencing TC of such system. Through GK method we reveal a logarithmic dependence of TC on time, underscoring the significance of temporal evolution in heat conduction dynamics. While on the other hand, using NMD method, we exam-

ine phonon lifetimes and group velocities for the first time within this framework. The study highlights size-dependent behavior, with TC exhibiting logarithmic divergence as system size increases, attributed to the characteristic behaviour of the phonon lifetime and group velocity dependence on the system size. The combined insights from GK and NMD methods present a comprehensive understanding of thermal transport in the FPU-β system, laying the groundwork for future research that aims to develop a generalized analytical model for TC by varying the anharmonicity parameter, β. This work is expected to enhance the design of materials with optimized thermal properties for advanced applications in electronics and energy technologies.

Contents

List of Tables

x

List of Figures

List of Symbols

a lattice constant

c_v volumetric specific heat

$\mathbf{D}$ dynamical matrix

$\mathbf{e}$ normal mode polarization vector

k_{B} Boltzmann constant, 1.3806×10^{-23} J/K

$\mathbf{k}$, k thermal conductivity

K kinetic energy

U potential energy

$\mathcal{W}$ work done

E total energy $(= K + U)$

$\boldsymbol{f}_i$ interatomic force

$\boldsymbol{F}$ force

L MD simulation cell size

m mass

n number of atoms in unit cell

N number of atoms in simulation cell

N_o number of unit cells in each direction of a cubic simulation cell

$\mathbf{q}$ heat flux

Q normal mode coordinate

$\mathbf{r}$ particle position

$\mathbf{J}$, J heat current

t time

T temperature

$\mathbf{u}$, u particle displacement from equilibrium

$\mathbf{v}_g$, v_g group velocity

V	volume
η	relative distance

Greek symbols

Γ	line width
$\boldsymbol{\kappa}, \kappa$	wave vector, wave number
l	mean free path
ν	polarization branch
τ	lifetime
$\boldsymbol{\Phi}$	force constant matrix
ϕ	spectral energy density
ω	angular frequency
ϵ	strain

Subscripts

b	summation index, particle label
i	summation index, particle label
j	summation index, particle label
l	summation index, unit cell label
o	equilibrium
α, β, γ	x, y, or z direction

Superscripts

*	complex conjugate
†	transpose complex conjugate

Abbreviations

BTE	Boltzmann transport equation
DFT	density functional theory
HCACF	heat current autocorrelation function
LJ	Lennard-Jones

MD   molecular dynamics

NMD   normal mode decomposition

SED   spectral energy density

TWD   thermostat work done

APMPW average per mode per wavevector

DOS   density of states

FPU   Fermi-Pasta-Ulam

TC   thermal conductivity

SLG   single layer graphene

BLG   bilayer graphene

tBLG   twisted bilayer graphene

GB   grain boundary

PC-G   polycrystalline graphene

Chapter 1

Introduction

1.1   Motivation

As technology continues to advance, industries such as aerospace, nuclear science, and electronics are facing significant challenges related to thermal management. Conventional materials like copper, silicon, and aluminum, which have been the cornerstone of these industries, are unable to meet the demands for efficient heat dissipation, especially in high-performance and miniaturized systems. Overheating remains a critical bottleneck in these fields, leading to decreased efficiency, reduced lifespan, and, in some cases, catastrophic failure of devices. Graphene, with its extraordinary thermal conductivity (TC), presents a groundbreaking solution to these challenges. This two-dimensional carbon material offers thermal performance far superior to traditional materials, making it as a key contender for future technologies where heat management is essential.

Graphene's ability to adjust its TC through structural modifications like grain boundaries (GBs) and nano-inclusions makes it highly versatile for technical applications. For example, in thermal interface materials (TIMs), graphene with controlled thermal

properties significantly improves heat transfer between processors and heat sinks, enhancing the performance of electronics [1, 2]. In thermoelectric generators, modified graphene reduces heat conduction while maintaining electrical properties, improving energy conversion efficiency [3]. Due to its exceptionally high TC, graphene is regarded as an ideal filler for producing polymer composites with superior TC [4]. Graphene-based composites offer significant potential for the space industry by enhancing the electrothermal properties of lightweight polymer components, enabling efficient temperature control and de-icing, while maintaining the polymer's structural integrity. This scalable and cost-effective approach makes them ideal for aerospace applications [5]. In the electronics industry, graphene can be used as a heat spreader to manage thermal loads in high-performance transistors and light-emitting diodes (LEDs) [6]. Additionally, graphene's thermal properties are being explored in energy storage systems, such as batteries and supercapacitors, to manage heat during charge and discharge cycles, enhancing safety and performance [7, 8].

Thus, the motivation for utilizing graphene lies in its potential to transform how heat is handled in critical technologies, pushing the boundaries of what is possible in sectors that depend on reliable, high-performance thermal solutions. By harnessing graphene's exceptional properties, we can address the current limitations of existing materials and pave the way for more efficient, sustainable, and safer technologies across multiple industries.

1.2 Background

Graphene, the first truly two-dimensional material, was discovered in 2004 by Andre Geim and Konstantin Novoselov using a simple yet ingenious technique known as the "Scotch tape method". By peeling off layers from bulk graphite with adhesive tape, they successfully isolated a single layer of carbon atoms arranged in a hexagonal lattice Fig. 1.1. This groundbreaking discovery, which earned them the Nobel Prize in Physics in 2010, opened up an entirely new field in materials science [9].

Graphene has the sp^2 hybridization of carbon atoms which forms a stable, highly conductive honeycomb lattice with strong carbon-carbon bonds. These robust bonds
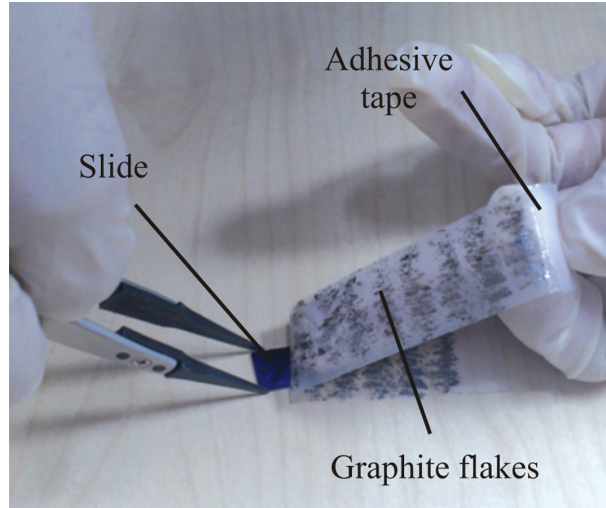
Figure 1.1: 'Scotch tape' procedure, reported by Novoselov and Geim in 2004. Picture adapted from [9]

.

allow efficient energy transfer between atoms, making graphene an exceptional heat conductor. These energy carriers in the case of graphene are "phonons", which are quantized vibrational modes within a crystal lattice and the primary carriers of heat in non-metallic materials. In bulk materials, phonon transport is typically limited by various scattering mechanisms, such as phonon-phonon interactions and impurities. However, in 2D structures like graphene, phonons behave differently due to the restricted dimensionality. The reduction in available scattering channels allows phonons to travel over longer distances with minimal resistance, resulting in a nearly ballistic transport regime. This unique phonon behavior is crucial to graphene's exceptional thermal performance and highlights the importance of studying 2D materials.

Another important consideration is the study of thermal transport in solids which requires an understanding of both harmonic and anharmonic phonon interactions. While Pierre Debye [10] laid the foundation for describing phonon dispersions and equilibrium thermodynamic properties, subsequent studies by Peierls [11] and Ziman [12] extended these ideas to include phonon-phonon interactions and heat conduction mechanisms in solids, emphasizing the role of nonlinearity in relaxation and transport. The simplest model, which assumes a lattice of harmonic oscillators, leads to an unrealistic scenario - any initial disturbance does not settle into equilibrium but instead frequently returns to a state close to its starting point. Additionally, energy transport

in such a model is purely ballistic, with each Fourier component carrying energy unchanged through the lattice at the speed of sound. Recognizing these limitations, Peierls introduced the concept of phonon-phonon scattering, which allowed for a more realistic description of heat conduction by incorporating anharmonic effects [11]. This marked the transition from purely harmonic models to a more comprehensive picture of thermal transport that included relaxation processes. In the 1930s, the inclusion of nonlinear terms in a perturbative quantum-mechanical framework allowed Rudolph Peierls to successfully explain the thermodynamic behavior of solids at very low temperatures. However, while these studies primarily focused on equilibrium properties, advancements in non-equilibrium statistical mechanics later revealed new complexities in phonon transport, particularly in low-dimensional systems where fluctuations dominate. Later, Enrico Fermi, John Pasta, and Stanley Ulam took on the challenge of studying the relaxation and transport properties of lattices of nonlinear classical oscillators. Their pioneering numerical experiments sparked an immense wave of research, shaping the understanding of nonlinear dynamics. These studies laid the foundation for exploring anomalous heat conduction in low-dimensional systems, where strong long-range correlations lead to deviations from standard hydrodynamic behavior and even violations of Fourier's law [13]. Initial studies of phonon dynamics were done in 1D systems, and this has led us to further extend the investigation to 2D systems. Unlike bulk materials, where heat transport follows well-established diffusion laws, low-dimensional materials exhibit unique transport mechanisms governed by collective phonon interactions, making their thermal properties fundamentally different from their three-dimensional counterparts. Originally developed to investigate nonlinear dynamics in lattice systems [14], the Fermi-Pasta-Ulam (FPU)-β model effectively captures the essence of anharmonic phonon interactions, key factors that influence TC [15]. By studying the 2D FPU-β potential, researchers can explore how nonlinearities affect phonon dynamics, offering new insights into the behaviour of heat conduction in 2D materials. This has direct implications for nanoscale thermal management, where engineering phonon interactions can lead to enhanced control over heat transport in nanomaterials and next-generation energy applications. Thus, this research can pave the way for designing the next generation of high TC materials, as it provides a detailed view of phonon interactions that are otherwise difficult to observe experimentally.

1.3 Challenges in the Study of 2D Materials

1.3.1 Experimental Challenges

Experimental challenges in the production of graphene significantly impact the accuracy of TC measurements. Variability in measurement techniques, such as Raman spectroscopy [16], electrical self-heating [17], and opto-thermal methods [18, 19, 20, 21, 22], can lead to a wide range of reported TC values due to their inherent limitations and potential sources of error. Additionally, the quality and preparation of graphene samples are critical; defects, impurities, and grain boundaries can reduce TC, and variations in sample preparation methods like chemical vapor deposition (CVD) [21] or mechanical exfoliation [23] can further influence measurements. Size and edge effects also play a role, as graphene nanoribbons exhibit different TCs compared to larger graphene sheets due to edge scattering and confinement effects. Environmental factors and substrate interactions can also affect thermal properties, with supported graphene often showing lower TC compared to suspended graphene [24]. Given these challenges, computational studies of graphene become essential to complement experimental data, providing detailed insights into its thermal behavior and helping to bridge the gaps caused by variability in experimental techniques and sample conditions Fig. 1.2.

1.3.2 Theoretical Challenges

Given the complexities involved in understanding the atomic-level mechanisms behind TC, computational studies have become indispensable. Experimental methods, while crucial, often fall short when it comes to probing the microscopic details of phonon transport. Computational simulations allow scientists to model phonon behavior in graphene under a variety of conditions, offering a detailed analysis of how structural and environmental changes impact TC. These studies not only complement experimental efforts but also provide predictive power, guiding the discovery of materials with tailored thermal properties and pushing the boundaries of what is achievable with 2D systems [1, 2].
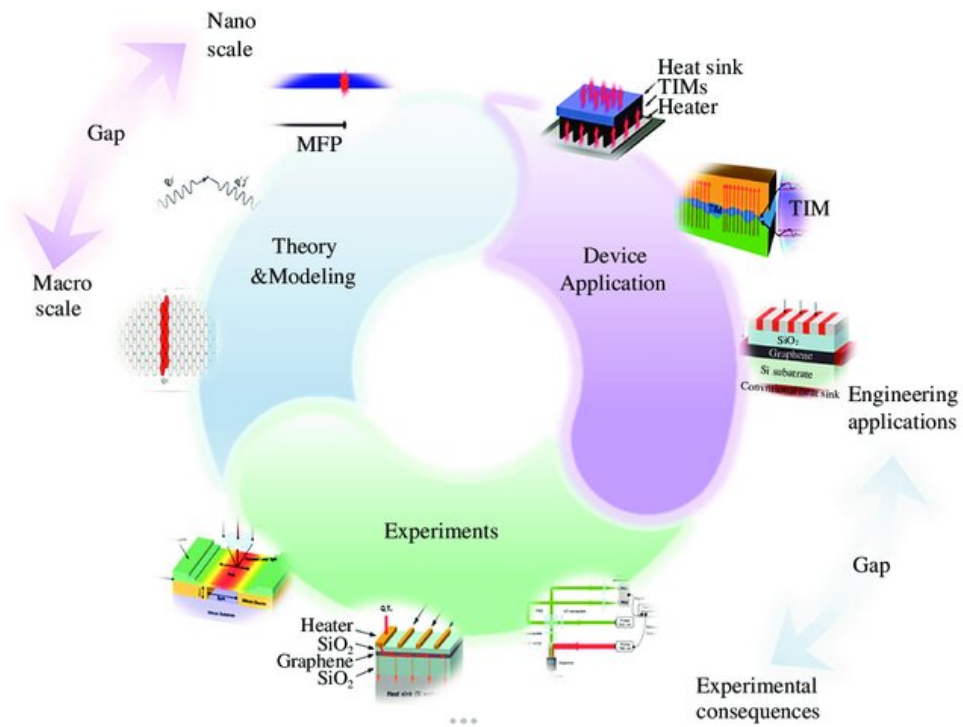
Figure 1.2: Schematic illustrating the theory and modeling, experimental processes, and device applications of graphene. There are gaps between theories at various scales and between experimental outcomes and their real-world impacts [25]

.

Theoretical Method	Theoretical Basis	Temperature	Statistics	Drawbacks
Kinetic Theory of Gases [26]	Treats phonons as particles in a gas.	Limited to simple, bulk materials.	Basic statistical mechanics.	Limited applicability for low-dimensional systems and complex interactions.
Debye Model [27]	Considers quantum mechanical nature of phonons and their distribution.	Applicable at low temperatures.	Uses Debye's approximation for phonon modes.	Assumes simple linear phonon dispersion; less accurate for complex materials.
Ab Initio Methods (DFT + BTE) [28]	Solves quantum mechanical equations for phononic properties using first-principles calculations.	Highly accurate across temperature ranges.	Uses first-principles methods.	Extremely computationally demanding, often requiring access to high-performance computing systems.
Boltzmann Transport Equation (BTE) [29, 30, 31]	Incorporates phonon scattering mechanisms and detailed phonon dispersion relations.	Broad temperature range.	Solves BTE numerically.	Complex analytical solutions and computational demands.
Green-Kubo Formalism [32]	Uses time-correlation functions from equilibrium MD simulations.	Effective across various temperatures.	Relies on Green-Kubo relations.	Requires long simulation times and significant computational resources.
Non-equilibrium Green's Function (NGEF) [33]	Quantum transport theory that calculates thermal transport in nanostructures by modeling phonon and electron interactions.	Broad temperature range.	Non-equilibrium statistics.	Complex setup and highly computational; sensitive to boundary conditions and scaling to large systems.

Table 1.1: Comparative overview of theoretical methods used for studying thermal conductivity

The table [1.1](#) provides a comparative overview of various theoretical methods used to study TC in materials. It outlines the theoretical basis, temperature applicability, statistical approaches, and drawbacks of each method. This comprehensive comparison helps in understanding the evolution of these methods and their respective strengths and limitations, offering valuable insights into their application in TC research.

Thus, the combined use of experimental and computational approaches in studying graphene and other 2D materials enhances our understanding of thermal transport mechanisms and drives the development of innovative materials. By exploring the high TC of graphene and utilizing models like the 2D FPU-β potential, researchers are unlocking new possibilities for the next generation of smart materials, capable of revolutionizing applications in electronics, energy management, and beyond.

1.4 Overview and Scope

The primary aim of this thesis is to explore how different factors influence TC in graphene and related 2D materials. This research delves into the comparative analysis of single layer and bilayer graphene, the thermal properties of polycrystalline graphene, and the application of the FPU potential model to investigate TC in 2D systems. Each chapter builds upon the methodologies and findings, providing a comprehensive understanding of TC in these advanced materials.

Chapter 2 serves as a literature survey, laying the groundwork for the subsequent chapters. It provides an in-depth review of the existing studies on TC in graphene and related 2D materials, highlighting key advancements and identifying gaps that this thesis aims to address. This background sets the stage for the methodologies and research questions explored in the later chapters.

Chapter 3 details the various methodologies employed throughout the thesis, offering a thorough understanding of the computational and theoretical techniques used. This chapter includes discussions on molecular dynamics simulations, spectral energy density analysis, and the implementation of the FPU beta potential model. It acts as a guide to the methods applied across the thesis, ensuring that the approaches are robust and appropriate for studying TC in 2D materials.

Chapter 4 focuses on comparing the TCs and phonon properties of single layer graphene (SLG) and bilayer graphene (BLG). By examining the phonon behavior and scattering mechanisms in these materials, the chapter provides insights into how the addition of layers affects thermal transport. Both theoretical models and experimental data are used to reveal the differences between SLG and BLG, contributing valuable information for designing graphene-based materials with tailored thermal properties.

Chapter 5 focuses on the TC of polycrystalline graphene, which is investigated using the Spectral Energy Density (SED) method. This chapter emphasizes the role of grain boundaries in heat conduction by analyzing the contributions of individual phonon modes. The preparation of polycrystalline samples and the application of the SED method are discussed in detail, highlighting the significant impact of grain boundaries on TC compared to single-crystal graphene.

Chapter 6 explores the effects of strain and ripple on graphene's thermal properties. This chapter examines how mechanical deformations influence phonon transport and TC in graphene, providing insights into the mechanical-thermal coupling that can be leveraged to engineer materials with desired thermal characteristics.

Chapter 7 delves into the FPU-β potential model to study TC in 2D materials. The FPU model is employed to capture the non-linear and anharmonic phonon interactions in graphene and other 2D structures, offering a novel perspective on phonon transport mechanisms. The chapter covers the theoretical foundation of the FPU model, its implementation in molecular dynamics simulations, and the implications of the findings for future high-TC materials.

Finally, **Chapter 8** summarizes the key results and insights gained throughout the thesis. It discusses the broader implications of the research, highlighting how the findings enhance our understanding of thermal transport in 2D materials. The chapter concludes with recommendations for future work, particularly in the context of designing the next generation of high-performance 2D systems.

This page was intentionally left blank.

Chapter 2

Literature Survey

This chapter provides a comprehensive review of the existing literature on the thermal properties of graphene and other two-dimensional (2D) materials, with a particular focus on their atomistic-scale behaviors. Graphene, with its exceptional thermal and mechanical properties, has been extensively studied; however, the complexity of real-world conditions introduces various factors that significantly influence its behavior. This survey focuses on four critical aspects of graphene research: bilayer graphene (BLG), single layer graphene (SLG) with grain boundaries, graphene under strain and ripples, and the application of the Fermi-Pasta-Ulam (FPU)-β potential to 2D materials.

Section 2.1 explores bilayer graphene (BLG), stressing its practical application due to its high thermal conductivity (TC). Next, we discuss the varied reported experimental studies, which is then followed by the theoretical and computational study of its thermal properties in previous studies which have used inconsistent especially highlighting use of some of the inconsistent methods.

In Section 2.2 we focus our attention to the TC of single layer graphene (SLG) across grain boundaries (GBs). While SLG is known for its exceptional TC, the presence of GBs, especially in polycrystalline graphene (PC-G), disrupts phonon transport and

reduces thermal efficiency. This section reviews both experimental and computational studies examining the influence of grain size, GB orientation, and dislocation density on TC. Additionally, it highlights the need for further investigation into phonon dynamics, such as phonon lifetimes and group velocities, in these systems as none of these works investigate the microstructural properties of the TC of PC-G samples.

While SLG is renowned for its high TC, the introduction of strain and ripples alters its phonon transport behavior, leading to its reduced efficiency. Section 2.3 reviews experimental and computational studies that explore how in-plane strain and ripple formation affect TC. Previous findings show that ripple and strain together can cause significant reductions in TC, largely due to changes in phonon dispersion and out-of-plane distortions while stressing on the fact that none had been able to decouple the strain and ripple while studying the changes in the TC of graphene.

Finally, Section 2.4 discusses the thermal transport in the FPU-β potential in 2D system such as square and triangular lattices. The section highlights about the limited study that have been done in terms of study of phonon dynamics in 1D system but we found a clear gap in the study of phonon dynamics in 2D systems. Additionally, we also address the previous studies with regards to the non-linearity, disorder, and temperature dependence, anharmonicity effects, etc in 2D system.

Together, these sections will provide a critical evaluation of the current research landscape and highlight the gaps that this thesis aims to address. By integrating findings across these four domains, this literature survey will lay the foundation for understanding the atomistic-scale thermal behavior of 2D materials and contribute to the development of advanced applications in thermal management and nano-engineering.

2.1 Thermal Conductivity of Single and Bilayer Graphene

The thermal conduction in single and bilayer graphene has received significant attention over the years and several applications have also emerged considering very high TC of graphene e.g. in thermal interface materials, hybrid phase change materials [34], heat spreaders [35], etc. Some potential applications have also been suggested such as temperature sensors, thermoelectric sensors and thermal biosensors [36]. A range

of values has been reported for the high TC of suspended single layer graphene (SLG) from the perspective of both experimental and computational techniques. Using micro-Raman spectroscopy, Balandin et al. [37] and Ghosh et al. [38] showed that the TC of SLG near room temperature is in the range from 2000 W/mK to 5300 W/mK depending upon different sample sizes and qualities. When SLG was grown by chemical vapor deposition method and the TC was measured with the Raman optothermal method, Cai et al. [39] reported the value to be around 2500 ± 1100 W/mK. On the theoretical and computational side, Renteria et al. [34] reviewd several studies for the TC of supported SLG and noted a range of values between 100 W/mK and 8000 W/mK depending upon different sizes, defect concentrations and methods used for calculating the TC. Using classical molecular dynamics (MD) simulations, the optimized REBO [40] as the classical interatomic potential between carbon-carbon (C-C) atoms and the Green-Kubo method for the TC calculation where heat flux was calculated using Irving and Kirkwood's [41] or Hardy's [42] definition, Hengzi Zhang et al. [43] found the TC of pristine SLG to be around 2903 ± 93 W/mK at 300 K. In another work, Y. Y. Zhang et al. [44] performed non-equilibrium molecular dynamics (NEMD) simulations over 254.2×60.9 Å^2 SLG where the C-C bond interaction was modeled by AIREBO [45] potential, used Muller-Plathe's approach for maintaining the temperature gradient between hot and cold ends, and obtained the TC around 550 W/mK near the room temperature. In another NEMD simulation based study, Cao [46] used the optimized Tersoff [40] potential and employed two different methods, heat flux control and temperature control methods, for setting up the temperature gradient between hot and cold regions and calculating the heat flux, and found the TC of 2.8 μm long-SLG to be around 2360 W/mK. Park et al. [47] similarly used the same optimized Tersoff potential for their NEMD simulations and obtained 3200 W/mK as the bulk (length $L \to \infty$) [48, 49] TC value, however, it has to be noted that they used the rate of change of difference in energy of the thermostatted hot and cold regions for the calculation of the heat flux which we call "thermostat work done (TWD)" method. In another Green-Kubo method based MD work, Chen and Kumar [50] used the optimized Tersoff potential and calculated the TC of 60×60 Å^2 suspended SLG as 1779.7 W/mK at 300 K temperature with the help of Irving and Kirkwood's [41] heat flux derivation. Using Boltzmann transport equation (BTE) based relaxation time approach (RTA), they also calculated the TCs of both sus-

pended SLG and SLG supported on copper where the values of phonon lifetimes were obtained by fitting the spectral energy density (SED) curves to the Lorentzian function. This approach revealed the in-plane TC around 1606.7 W/mK for the suspended SLG of 28 unit cell size ($\approx 69\,\text{Å}$) along x-axis. Qiu and Ruan [51] performed MD simulations in combination with SED analysis over 4.4×4.3 nm^2 suspended SLG and SLG supported on a silicon dioxide substrate where C-C interactions were modeled by the optimized Tersoff potential. They reported the phonon relaxation times for the suspended SLG up to 50 ps. They also calculated the TC [52] of SLG whose value before the quantum correction was found to be 1626 W/mK at 300 K. Zou et al. [53] studied the effect of different interatomic potentials on the dispersion curves and thermal transport properties such as phonon relaxation time and TC and found that the optimized Tersofff [40] gives the highest relaxation times for low-frequency acoustic phonons. For 20×20 primitive unit cell SLG system, they found the TC close to 2500 W/mK from the SED method and 1192 W/mK from the Green-Kubo method. Very recently, Han and Ruan [54] showed that four-phonon scattering plays a dominant role in SLG thermal transport, leading to a finite thermal conductivity (~ 1300 W/mK) at 10 μm system size, which is lower than diamond, contrary to previous predictions of TC divergence.

Some experimental and computational works have also been done on the suspended AB-stacked bilayer graphene (AB-BLG) and AA-stacked twisted bilayer graphene (tBLG). The twisting of graphene layers when placed over each other leads to Moiré pattern, as shown in Fig. 2.1. Pettes et al. [56] measured the TC of turbostratic bilayer graphene with a rotation of 11.7° between two graphene layers using the electrical self-heating method and a value of around 600 W/mK was revealed at the room temperature. Using an opto-thermal Raman technique, Hongyang Li et al. [57] estimated the TCs of AB-BLG and tBLG with a twist angle of 32.2° and found them to be 1896 ± 410 W/mK at 314 K and 1413 ± 390 W/mK at 323 K, respectively. The authors attributed the reduction in the TC of tBLG to the modification in the phonon dispersion curves and the emergence of numerous folded acoustic phonon branches which led to additional mini-Umklapp scattering channels for phonons. Later, using similar technique, Han et al. [58] quantified the TCs of AB-BLG as 2071 ± 149 W/mK and TCs of tBLGs with 2°, 11°, 27° and 30° as 1753 ± 126, 1666 ± 149, 1817 ± 178 and 1929 ± 212, respectively, near room temperature conditions. Using a linearized BTE and perturba-
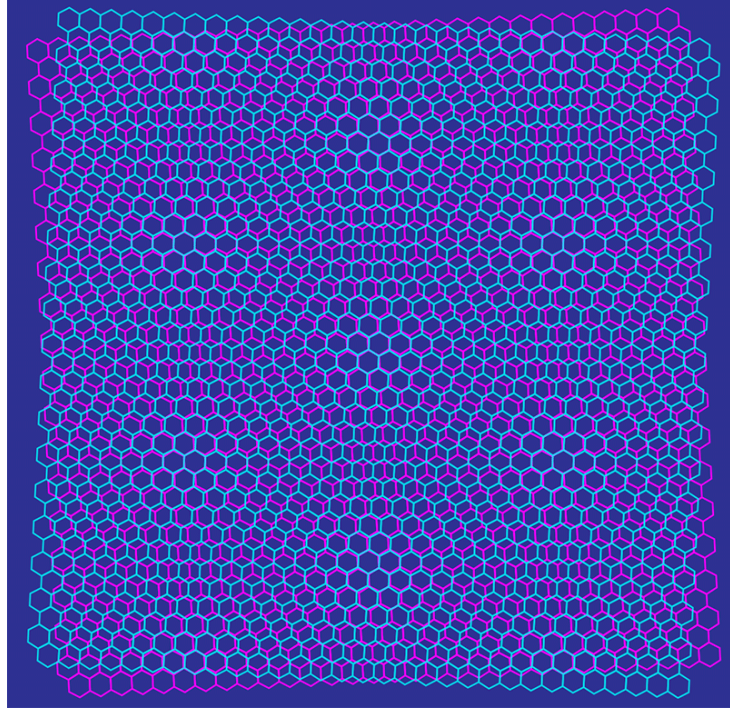
Figure 2.1: Overlaying two honeycomb lattices of single layer graphene and creating a relative twist between them results in twisted bilayer graphene (tBLG) which is also known as the Moiré pattern [55].

tion theory, Lindsay et al. [59] used optimzed Tersoff potential [40] for the intralayer and the Lennard-Jones (LJ) potential for the interlayer C-C atoms and calculated the TCs of AA-stacked $5\,\mu$m length SLG and BLG samples close to 2600 and 2200 W/mK at 300 K. In all the works cited below, the interlayer C-C atoms have been modeled using the LJ potential, however, with different LJ parameters. With a similar methodology but changed LJ parameters and full iterative solution of the BTE, Singh et al. [60] reported the TCs of SLG and BLG samples close to 3200 and 2200 W/mK, respectively at 300 K. In the NEMD setting, Wei et al. [61] used Tersoff potential [62] for the intralayer atoms and the LJ for the interlayer atoms, imposed a constant heat flux between hot and cold regions by scaling the velocities of the atoms, and obtained the bulk TC for AA-stacked SLG and BLG as 870 W/mK and 820 W/mK, respectively, at room temperature. In another NEMD work, Chenyang Li et al. [63] used the REBO [64] potential for the in-plane atoms and then they employed the Muller-Plathe algorithm for the calculation of heat flux and finally reported the bulk TCs of AB-BLG around 1050 W/mK and those of tBLGs with twist angles of 21.8°, 32.2° and 13.2° as around 800, 640 and 560 W/mK,

respectively, at 300 K. They also obtained phonon dispersion curves with the help of Fix-Phonon package of the LAMMPS code [65] and found that the phonon velocities and energies are not changed by misorientation angles in tBLG. Instead, they attributed the reduction in phonon lifetimes and the consequent increase in the Umklapp scattering as the dominant reason behind the reduction in the TCs of tBLGs. This was backed up by density functional theory (DFT) based calculations of phonon lifetimes of AB-BLG and tBLG with twist angle of $21.78°$. Nie et al. [66] used optimized Tersoff [40] for the intra-layer interactions and performed NEMD simulations over 22×10 nm^2 samples of BLGs, 4-layer and 6-layer graphenes with different twist angles where temperatures of hot and cold regions were controlled by the Langevin thermostats. Their reported values of the TCs for the tBLGs with twist angles between 1 and 30 degrees are in the range of approximately 320 to 450 W/mK at 300 K temperature. The corresponding quantum corrected [46] values are in the range of 270 to 370 W/mK. Liu et al. [67] also performed NEMD simulations by setting the temperature of hot and cold regions with the Langevin thermostats over 20×10 nm^2 tBLG samples using the optimized Tersoff potential for the intralayer interactions, and obtained the TCs along the length axis in the range of 361 to 473 W/mK when the twisting angle changes from $0°$ to $30°$. The heat flux was calculated by the TWD method [47]. They also reported anisotropy in TCs for these samples which tend to decrease as the twisting angle increases, calculated the phonon lifetimes by fitting the SED curves to the Lorentzian function for different branches of phonon dispersion for the same samples and calculated the bulk TCs as 699.44 and 401.61 W/mK corresponding to the twist angle $0°$ and $21.78°$, respectively.

The TC of bilayer graphene has received significantly less attention than that of single layer graphene, despite its promising applications in thermal management. Previous studies have reported a wide range of TC values without fully addressing the unique properties of bilayer structures. This gap in research highlights the need for further investigation into the thermal transport mechanisms specific to bilayer graphene, as understanding these factors could lead to improved performance in practical applications. Exploring the TC of bilayer graphene will provide valuable insights into its potential uses in advanced materials.

2.2 Grain Boundary in Single Layer Graphene

One crucial aspect often overlooked is the influence of grain boundaries (GBs) on the TC of polycrystalline graphene (PC-G) with some notable exceptions. Experimentally, it has been found that the TC of PC-G increases with increase in grain size. Ma et al. [68] reported that the TC exponentially increased from almost 610 to 5230 W/mK at the room temperature as the grain size increased from almost 200 nm to 10 μm. Similarly, Woomin Lee et al. [69] found the in-plane TC in the temperature range from 320 K to 510 K to be 680–340, 1890–1020 and 2660–1230 W/mK for average grain sizes of 0.5, 2.2, and 4.1 μm, respectively. Dongmok Lee et al. [70] measured significantly smaller TCs (412-572 W/mK) for PC-G samples with reduced grain sizes of less than 1 μm. They also showed almost no dependence on misorienation (tilt) angles of GBs for the TCs of PC-G samples whereas there was strong dependence on misorienation angles for bicrystalline graphene (BC-G) samples.

Numerically, one of the earliest studies to investigate the GB effect on the TCs of PC-G samples was done by Bagri et al. [71], who performed reverse non-equilibrium molecular dynamics simulations with modified Tersoff interatomic potential on tilt GBs based graphene samples with misorientation angles $5.5°$, $13.2°$ and $21.7°$, and estimated the bulk TCs to be around 2220, 2380 and 2380 W/mK, respectively, thereby showing a very week dependence on the misorientation angles. They also calculated boundary conductance (inverse of Kapitza resistance) which decreased with increase in misorientation angles. Following non-equilibrium Green's function approach, Serov et al. [33] showed strong increasing dependence of the TCs of PC-G samples on grain sizes ranging from close to 1 nm to 1000 nm at room temperature, for which the TCs vary from close to 100 W/mK to 550 W/mK. However, the dependence on the misorientation angle was found to be negligible. In another study, using REBO potential for interatomic potential and Green-Kubo method for the calculation of the TC, Mortazavi et al. [72] prepared PC-G samples with average grain size from 1 nm to 5 nm and found the TCs of PC-G samples to be one order of magnitude smaller than that of pristine graphene. With the same REBO potential and approach-to-equilibrium molecular dynamics simulations, Hahn et al. [73] estimated the bulk TC of PC-G with an average grain size

of 1 nm as 26.6 W/mK at 300 K, which was almost 3% of the crystalline sample. The presence of GBs significantly decreased the estimated mean free path from 451 nm for crystalline graphene to around 30 nm for PC-G, which suggested increased scattering of phonons with GBs. With the help of Green-Kubo method and optimized Tersoff potential, Liu et al. [74] showed that the TC decreases exponentially with increasing GB energy for PC-G samples.

With the help of the non-equilibrium molecular dynamics (NEMD) method [48], another set of computational works [75, 76, 77] on BC-G samples show strong dependence of the tilt angle and average density defects along GB on the Kapitza resistance. In a detailed comprehensive NEMD based study, Fox et al. [78] performed simulations on bicrystalline graphene nanoribbons (bi-GNR) [1] for a wide range of tilt angles (θ) under arbitrary in-plane thermal loading directions (ϕ). They showed that the TCs decrease from 0° to 32.2° tilt angles and then increase almost symmetrically up to 60° tilt angles. Having done the size-dependent analysis for $\phi = 10°$, they calculated the bulk TCs for $\theta = 9.4°, 32.2°, 44.8°$ and found them to be close to 416, 312 and 476 W/m K, respectively. This dependence on misorientation angles is similar to the experimental work done by Dongmok Lee et al. [70] for BC-G samples. Using similar NEMD method, another study found that 10.98^o BC-G displays anomalous higher TC compared to other misorientation angles [79], which was not observed by Fox et al. [78]. In both works, it has been established that the TC is inversely proportional to the dislocation density of GB. In a recent NEMD based work done by Tong et al. [80], where the heat flux was calculated with the incorrect thermostat work done method [81], which overestimates the TC value in comparison to that obtained by a more consistent Irving-Kirkwood based calculation of heat flux, the TCs of BC-G samples were found to first decrease with the tile angle from 0° to 13.18°, but then contrary to Fox et al. [78] was shown to have increased for 21.78° tilt angle.

These works mostly focus upon the calculation of the TCs of PC-G or BC-G samples using Green-Kubo or NEMD approaches [48, 49] and show that the TCs increase with increasing grain size. The TC of BC-G depends upon the misorientation angle [70, 79, 78, 74], however, the dependence has been found to be weak for PC-G samples [71, 33].

---

[1]Although they write polycrystalline but their simulation details suggest bi-GNR samples because periodicity along x-axis is not present.

The NEMD based works also explore the effect of GBs and misorientation angles on the Kapitza conductance and some studies have also been able to capture the dependence on GB energy and dislocation density, however, none of these works investigate the microstructural properties of the TC of PC-G samples such as phonon mean lifetimes and group velocities of different phonon modes in detail. We found only one study done by Tong et al. [80] which discusses the contribution of phonon lifetimes and group velocities, obtained from the Spectral Energy Density (SED) method and the lattice dynamics, respectively, for the GBs with three different misorientation angles, $\theta = 4.41°, 13.18°, 21.78°$, however, the treatment and the discussion remain brief. Moreover, the sample preparation does not seem to have followed proper procedures to maintain stable dislocation core structure [82]. The study also adopts the alternative phonon SED Φ' [83] approach for the extraction of spectral phonon relaxation times which does not involve eigenvectors and, therefore, does not represent the phonon spectral energy [83] accurately. Further, the calculation of phonon lifetimes and group velocities has been performed for polycrystalline samples because the SED method assumes periodicity along all three coordinate axes, however, they have been cited as supporting evidences for the TCs of BC-G samples obtained by the NEMD method.

As grain boundaries can significantly influence phonon scattering and thermal transport, yet existing literature often neglects the specific effects of different grain boundary angles. Research on graphene with grain boundaries (GB) at various angles offers a promising area for further investigation, as there are few studies examining how these orientations affect TC. Exploring this relationship could provide valuable insights into the mechanisms behind changes in TC, emphasizing the need for dedicated research to understand the impact of grain boundary interactions on graphene's thermal properties.

2.3   Single Layer Graphene with Strain and Ripple

The impact of strain on the TC of bulk materials has been extensively studied over the years of which few are mentioned here [84, 85, 86, 87, 88]. In conventional three-dimensional materials, compressive strain typically increases TC by stiffening phonon
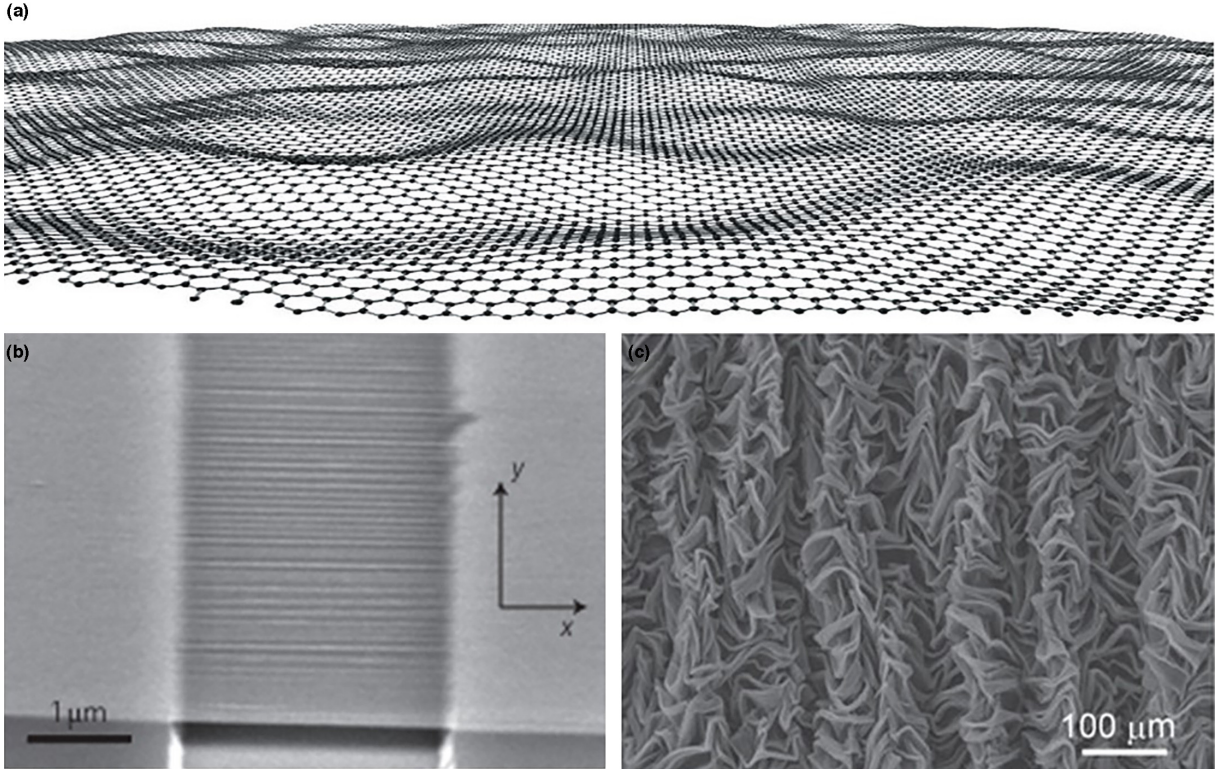
Figure 2.2: Graphene in various structural forms: (a) rippled graphene, (b) wrinkled graphene, and (c) crumpled graphene. [93].

modes, while tensile strain decreases it by softening these modes [86, 87, 89, 90]. This relationship follows a power-law dependence as described by the Peierls–Boltzmann framework [86]. However, this rule does not hold for low-dimensional materials, particularly one-dimensional structures like carbon nanotubes (CNTs). Under compressive strain, localized buckling structures form, increasing phonon scattering and significantly reducing TC [91, 90].

By default, the 2D single layer graphene sheet has corrugations [92]. From literature [93], out-of-plane displacements have been categorized as wrinkles, ripples and crumples based on their aspect ratio, physical dimensions, topology and order, as follows: wrinkles and ripples occur nominally on two-dimensional plane, where wrinkles have a high aspect ratio with width between one and tens of nm, height below 15 nm, and length above 100 nm (aspect ratio > 10); and ripples are more isotropic (aspect ratio = 1) valleys and peaks with feature size below 10 nm Fig. 2.2 [94]. On the other hand, crumples are dense deformations (folds and wrinkles) occurring isotropically (ordered or unordered) in two or three dimensions (similar to crumpled paper) [95, 96]. Other

experiments have also revealed that suspended graphene membranes commonly form spontaneous ripples [97, 92, 98, 99].

Since graphene has a two-dimensional structure, its strain response differs from three-dimensional bulk materials and one-dimensional CNTs because strain-induced stress can partially dissipate perpendicular to the sheet. Especially in the presence of intrinsic ripples in graphene [100], the effect of strain makes the case all the more interesting where earlier studies have failed in order to decouple the strain and the ripple in effect while studying the TC of graphene.

Experimentally, the effect of bi-axial strain has been studied by Nakagawa et. al. [101] where they showed that with small strain the TC of graphene decreased significantly. Another study done by Kuang et. al. [102] reported size dependency and strain effect on the TC of SLG. Another study done by Kuang et. al. [102] reported size dependency and strain effect on the TC of SLG. Guo et. al. [103] in their work on suspended graphene with strain have shown that the TC decreases as the strain increases owing to the fact that the applied strain softens the higher frequency phonons and also reduces the phonon group velocities. Another recent experimental study done by Wang and Zhang [104] have shown similar decrease in the TC with increasing uniaxial strain using opto-thermal Raman technique to characterize the thermal transport properties.

Theoretically, in 2009, Bao et al. [105] were the first to explore the modulation of ripples in graphene through its negative thermal expansion. Li et al. [91] observed a decrease in TC in single layer graphene (SLG) under strain, attributing it to changes in the dispersion curve, as seen in Fig. Fig. 2.3, where the frequency shifts with increasing strain. Wei et al. [106] 2011 published their research in which they studied the strain effects on the TC of GNRs with different edges (ZGNR, AGNR) based on the reverse non-equilibrium molecular dynamics (RNEMD) method. They found that Under tensile strain, TC is reduced by softening the phonon modes, while under compressive strain the phonon modes are almost constant. In another study, it was observed that under a compressive strain, as the size of the graphene sheet increases, the wavelength and amplitude of the ripples increase as well [107]. In 2012, Baimova et al. [108] used molecular simulations to control these ripples by applying in-plane strain. Dmitriev et al. [109] further showed that the simultaneous application of shear and tensile forces

21
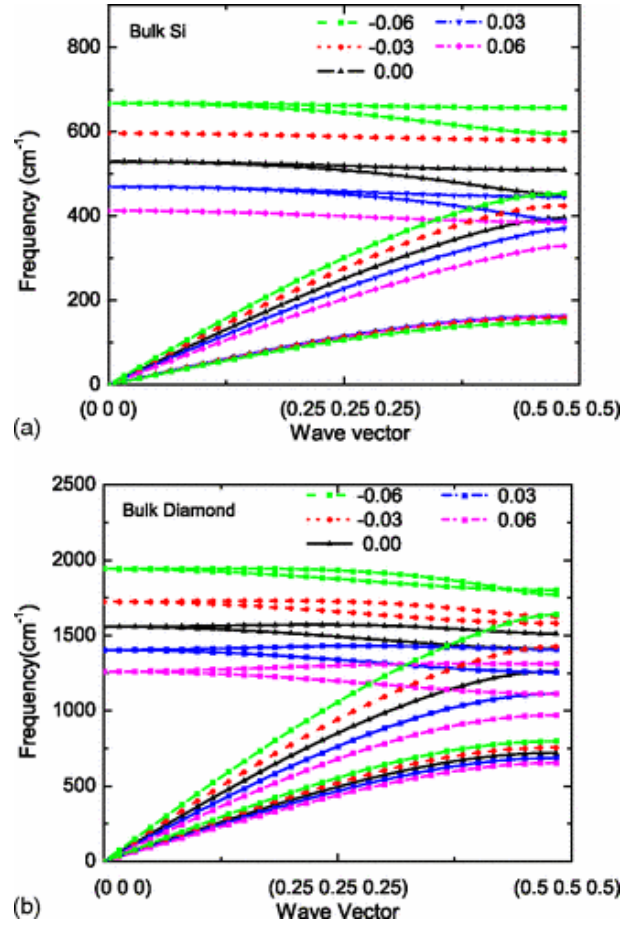
Figure 2.3: Phonon dispersion curves for: a) bulk silicon and b) bulk diamond under varying strain conditions [91].

can produce ripples with adjustable size and orientation. In 2013, Zhang et al. [110] found through molecular simulations that applying strain transforms the ripples in graphene into structural ridges, resulting in a 20% to 30% reduction in TC. Similarly, in 2015, Lee et al. [111] observed a decrease in TC, alongside an increase in ripples, when studying silicon-doped graphene using molecular dynamics. In 2016, Hahn et al. [112] used NEMD simulations to show that higher out-of-plane corrugation in graphene also leads to reduced TC. Continuing this line of research, Park et al. [113] in 2017 introduced a technique using molecular dynamics simulations to develop uniformly distributed ripples with different heights through strain engineering. They found that as the ripple height increased, the TC decreased.

Thus, previous studies have offered insights into the effects of strain and ripple on the TC of single layer graphene (SLG), but they often lack a quantitative analysis of these interactions. Many investigations focused on qualitative observations without systematically evaluating how strain influences phonon dispersion and group velocity. Additionally, while some explored the ripple effect, they did not adequately quantify its impact on TC, particularly concerning out-of-plane fluctuations. The studies so far have found that strain-induced increase in ripples reduces the TC of the flat graphene sheet, however, the MD-based calculations have shown only the combined effects of both strains and ripples on the TC. There have not been any attempts to decouple the effect of strains and ripples on the TC of graphene sheets. In the present work, we attempt to fill this gap by distinguishing the individual effects of strains and ripples using equilibrium MD simulations with GK and SED methods.

2.4 2D FPU-β Lattices

The FPU problem is about how energy spreads between different vibrational modes in a weakly non-linear system, starting from an initial state far from statistical equilibrium. Despite 70 years of study and advances in both theory and computing, the main question remains: how is this problem related to classical statistical physics? From the first numerical experiment performed by Fermi, Pasta, Ulam, and Tsingou in order to observe the energy sharing in one-dimensional lattices with non-linear coupling among

rigid masses, there have been an immense number of studies related to the 1D chain study of its thermal properties. This eventually led to the study of 2D systems. The earliest studies to understand heat transport in the 2D system were done in [114, 115]. These authors examined the combined effects of non-linearity and disorder on heat conduction in two-dimensional harmonic and anharmonic lattices using Lennard-Jones pair potentials. Their research also focused on analyzing how TC varies with temperature and impurity concentration, which serves as a measure of disorder. They observed an increase in conductivity in disordered non-linear systems compared to the harmonic case. Later, Mountain and MacDonald [116] conducted a more detailed study on the temperature dependence of TC. They examined a two-dimensional triangular lattice composed of unit-mass atoms interacting through a Lennard-Jones 6/12 potential. Unlike earlier studies, no disorder was introduced, and their numerical results aligned with the expected classical law, showing TC proportional to T^{-1}. However, the dependence on system size was not explored in their research [116]. The interplay between disorder and anharmonicity, initially explored by Payton, Rich, and Visscher, was revisited by Poetzsch and Böttger [117, 118], who studied percolating and compositionally disordered 2D systems. They focused on identifying the contributions of third- and fourth-order anharmonicity, concluding that, at the same temperature, the latter results in a higher TC than the former. Additionally, the authors investigated the system size dependence of conductivity. While they adopted the same perspective as Michalski [119], a closer analysis of Fig. 2.4 in [117] suggests that their data also support a systematic increase in TC with system size.

During the early 2000s, the divergence of the heat conductivity in the thermodynamic limit was investigated in 2D-lattice models of anharmonic solids with nearest-neighbour interaction from single-well potentials [120]. They studied the size effect and the asymptotic behavior of the TC in 2D square FPU lattice. For a large δ (where $\delta = N_y/N_x$; N_x and N_y are the number of units cells in the x and y direction respectively), the simulation results show that δ has a logarithmic divergence for the 2D lattices. It shows that the dimensional crossover happens in $\delta^* \to 0$ for $N_x \to \infty$ [121]. Studies related to defects have [122] found that the missing bond defects give rise to finite TC due to a thermal gradient formation. Otherwise, the TC is infinite in the 2D generic disordered harmonic lattice. There are some inconsistent results, indicating that
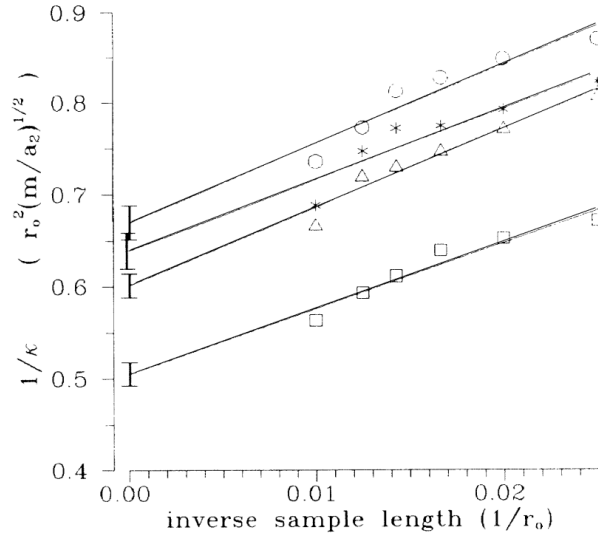
Figure 2.4: The reciprocal heat conductivity as a function of the reciprocal sample length (Error bars according to statistical fluctuations for the extrapolated values). The temperatures of the heat baths T_1 and T_2 are held constant at $0.0024a_2/k_B$ and $0.0071a_2/k_B$, respectively, where a_2 is the constant of the second order in LJ potential. The constant width is 40 layers. In a percolation system, the sites (bonds) on a lattice are randomly chosen with probability p = 0.85. Pairs of (f_3, f_4) are represented as $*, (0, \frac{1}{2})$; $o, (1, \frac{1}{2})$; $\square, (0, 8)$; $\triangle, (4, 8)$ where f_3 and f_4 are numerical factors introduced for studying the dependence of heat conduction on the strength of anharmonicity in the Lennard-Jones potential [117].

an in-depth study of the 2D cases has not been done. For example, [123] shows that for strong chaotic regime, k(N)$\sim ln(N)$ and the weak chaotic regime follows a power law, k$\sim N^{\alpha}$ where $\alpha \sim 0.77$ using NEMD method with FPU-β potential [120]. In another study, the weak chaotic regime shows the power law behavior, but the ambiguity lies in the $\alpha \sim 0.22$ value. The argument given is that as one keeps on increasing the size of the system, the weak chaotic regime's power law tends towards the logarithmic law [124]. Although they perform the simulation for larger system size, the criticism of [124] lies in the fact that the temperature chosen is in the strong chaotic range, and their argument for such α values is not backed by any of the current theoretical support. Another study showing the size effect in the 2D case is done in [121] using NEMD method with FPU-β. It is shown that the TC nature will change from logarithmic nature in 2D case to power law in 1D case as $\delta^* \to 0$ where $\delta = N_y/N_x$ (as the strip gets thinner and thinner, 2D tend towards 1D). Another study on 2D lattices using Toda lattice disregards the study of Umklapp processes while calculating TC, a phenomenon far from thermal equilibrium, in lattices [125]. Analysis performed with mass-disordered harmonic solids using NEMD method gave $\alpha \sim 0.59 - 0.59$ with two different types of stochastic baths [126].

The most recent studies done in the field of getting the associated thermal properties of 1D systems were done using Lorentzian fitting of Spectral Energy Density and getting mean free path, phonon lifetime, etc., using FPU-β potential [127]. The phonon lifetimes followed $\tau \sim k^{-1.7}$ for small κ at different temperatures. This study showed the divergent power law behaviour $k \sim N^{\alpha}$. The relation of α and μ given by $\alpha = 1 - \frac{1}{\mu}$ [128, 129] shows that α comes out to be ~ 0.41 and which agrees with previous studies. Similar study has been extended in order to study diatomic [130, 131], defect [132] and interfacial [133, 134] systems. Thus, apart from [127], there has been no study for the 2D system related to the phonon dynamics and their properties. Hence, for the first time, we have studied the phonon properties of the 2D FPU-β based potential system in order to investigate its thermal properties.

Chapter 3

Methodology

In this chapter, we present a detailed methodology for calculating the thermal conductivity (TC) of 2D systems, outlining the three primary approaches used in this study. We begin with the direct method, which employs non-equilibrium molecular dynamics (NEMD) simulations. It is then followed by two equilibrium molecular dynamics (EMD) methods, which include the spectral energy density (SED) based normal mode decomposition (NMD) method and the Green-Kubo (GK) method. Each method is explained in the order in which it was applied during the study of different types of systems, providing a comprehensive understanding of their implementation and relevance to 2D thermal transport studies.

3.1 Non-equilibrium Molecular Dynamics

The NEMD "direct method" is a standard approach based on steady state heat conduction governed by Fourier's law which linearly relates the steady-state heat flux vector
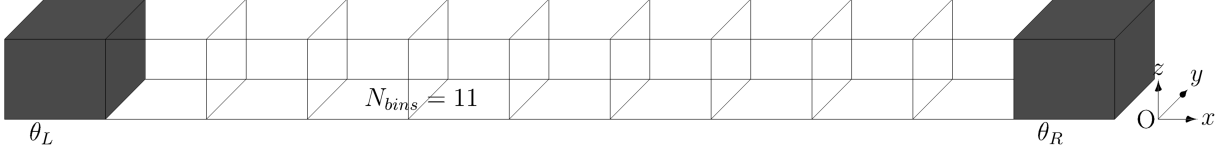
Figure 3.1: Schematic diagram of a nanoribbon partitioned into bins with free BCs. Shaded regions are thermostatted.

$q(x)$ at position x in the current configuration and the temperature gradient $\nabla\theta$ as

$$q(x) = -k\nabla\theta(x), \tag{3.1}$$

where $\theta(x)$ is the temperature at position x. Further, k is the TC tensor of the system, which can be represented by a diagonal matrix

$$k = \begin{bmatrix} k_{xx} & 0 & 0 \\ 0 & k_{yy} & 0 \\ 0 & 0 & k_{zz} \end{bmatrix}.$$

for our studied systems. We model these systems as nanoribbons and divide them into N_{bins} bins of equal size as shown for example in Fig. 3.1 for $N_{\text{bins}} = 11$. The heights of the SLG and BLG nanoribbons were taken as 3.34 Å and 6.68 Å, respectively. The center of mass of each bin serves as a macroscopic probe position x. A temperature gradient is established only along x-axis by thermostatting the left and right ends of the nanoribbons at two different temperatures θ_L and θ_R, respectively, with free boundary conditions (BCs) in all directions. Thus, we impose the following BCs for the nanoribbons:

$$\theta(x=0, t) = \theta_{\text{L}}, \quad \theta(x=L, t) = \theta_{\text{R}}, \tag{3.2}$$

where $x = 0$ and $x = L$ correspond to the x coordinates of the center-of-mass of the first and the last bin, respectively. For this set-up, the corresponding steady-state behavior

28

is governed by 1D form of the Fourier's law in Eq. (3.1):

$$q(x) = -k\frac{\partial \theta}{\partial x}(x),\qquad(3.3)$$

where q is the only available heat flux along x-axis and $k_{xx} = k$ is the xx-component of the TC tensor $\boldsymbol{k}$.

In MD, we obtain time-dependent positions and momenta of all particles in the system after integrating the equations of motion [135]. As a function of the spatial average of the kinetic energy of all atoms in a given bin, the instantaneous temperature of bin n becomes [48]

$$\theta_n^{\text{inst}} = \frac{2\mathcal{K}}{3N_n k_{\text{B}}},\qquad(3.4)$$

where $\mathcal{K}$ is kinetic energy (with rigid-motion removed [136]) of all N_n atoms in bin n and k_{B} is Boltzmann's constant. For the calculation of the heat flux $\boldsymbol{q}$, we consider a system of N atoms with mass of ith atom as m_i, position as $\boldsymbol{r}_i$, distance between atoms i and j as $r_{ij} = \|\boldsymbol{r}_j - \boldsymbol{r}_i\|$, and $\tilde{\boldsymbol{v}}_i$ as the velocity of atom i relative to the center-of-mass velocity of the system. The heat current $\boldsymbol{J}$ for systems with pair potential interactions is [41, 48]:

$$\boldsymbol{J} = \sum_{i=1}^{N} e_i\tilde{\boldsymbol{v}}_i + \sum_{\substack{i,j \\ i<j}}^{N} \left[\boldsymbol{f}_{ij} \cdot \frac{\tilde{\boldsymbol{v}}_i + \tilde{\boldsymbol{v}}_j}{2}\right](\boldsymbol{r}_i - \boldsymbol{r}_j).\qquad(3.5)$$

Here, e_i represents the local site energy of atom i which includes both kinetic and potential energy terms and $\boldsymbol{f}_{ij}$ is the force on atom i because of atom j [48]. This definition, known as obtained through Irving-Kirkwood (I-K) procedure [41], can further be extended to interatomic potentials with three-body terms [41, 137]. The x-component of the heat current in Eq. (3.5), J_x, with $N = N_n$ atoms for bin n provides the expression for the instantaneous heat flux at center-of-mass of bin n as $q_n^{\text{inst}} = J_x/V_n$, where V_n is the volume of bin n. The steady-state value of any thermodynamic property $\mathcal{A}$, such as temperature and heat flux, is its phase average, which following *ergodic hypothesis* [135]

is obtained by performing a long-run time average in an MD simulation:

$$\mathcal{A}_n = \left\langle \mathcal{A}_n^{\text{inst}} \right\rangle = \frac{1}{t_{\text{ss}}} \int_0^{t_{\text{ss}}} \mathcal{A}_n^{\text{inst}}(\tau) \, d\tau, \tag{3.6}$$

where the subscript n refers to the bin n and t_{ss} is a long time at which steady-state has been assumed to be achieved. Calculating temperature and heat flux along x-axis for each bin gives us corresponding temperature and heat flux profiles. The temperature gradient is calculated by fitting straight lines to the steady-state temperature profiles in the regions considerable away from the thermostats. We exclude the two nearest bins to both left and right thermostatted bins for the linear fitting. This gives us the TC, k, in Eq. (3.3) as

$$k = \langle q \rangle \left(\frac{\Delta\theta}{\Delta x} \right)^{-1}, \tag{3.7}$$

where $\Delta\theta/\Delta x$ is the linearly-fitted temperature gradient and $\langle q \rangle$ is the average of the x-component of the heat flux vector of all bins included in the fitting. The obtained k is both length and width dependent. We first obtain a converged value of k by increasing the width and then we keep increasing the length of the nanoribbon so that an extrapolated bulk TC can be obtained.

3.2 Normal Mode Decomposition

The TC tensor of a system can also be calculated using phonon properties such as group velocities and phonon relaxation times in an expression derived from the Fourier's law in Eq. (3.1) and the phonon BTE under the relaxation time approximation (RTA) [138, 83]:

$$\boldsymbol{k} = \sum_{\boldsymbol{\kappa}} \sum_{\nu} c_v(\tfrac{\boldsymbol{\kappa}}{\nu}) \, \boldsymbol{v}_g(\tfrac{\boldsymbol{\kappa}}{\nu}) \otimes \boldsymbol{v}_g(\tfrac{\boldsymbol{\kappa}}{\nu}) \, \tau(\tfrac{\boldsymbol{\kappa}}{\nu}), \tag{3.8}$$

where the summation is over all phonon modes, also known as normal modes, in the first Brillouin zone (BZ), denoted by wavevector $\boldsymbol{\kappa}$ and dispersion branch ν. Also, $c_v(\tfrac{\boldsymbol{\kappa}}{\nu})$,

$v_g(^{\boldsymbol{\kappa}}_\nu)$ and $\tau(^{\boldsymbol{\kappa}}_\nu)$ are the mode specific volumetric specific heat, group velocity and relaxation time or phonon lifetime, respectively. The symbol $\otimes$ represents the dyadic product of two vectors which turns the TC $\boldsymbol{k}$ into a tensor. The group velocity comes from the dispersion curve's gradient, i.e. $v_g(^{\boldsymbol{\kappa}}_\nu) = \frac{\partial \omega(^{\boldsymbol{\kappa}}_\nu)}{\partial \boldsymbol{\kappa}}$, which can be obtained by defining a fine grid of wavevectors around the given mode $(^{\boldsymbol{\kappa}}_\nu)$ and then using finite difference method over this grid. The frequency $\omega(^{\boldsymbol{\kappa}}_\nu)$ is obtained by harmonic lattice dynamics calculation [139, 83] based GULP package [140]. In the quantum sense, $c_v(^{\boldsymbol{\kappa}}_\nu)$ in terms of Planck's constant $\hbar$, Boltzmann's constant k_B and temperature θ is given by

$$c_v(^{\boldsymbol{\kappa}}_\nu) = \frac{k_B}{V} \left(\frac{\hbar\omega(^{\boldsymbol{\kappa}}_\nu)}{k_B\theta} \right)^2 \frac{\exp\left(\hbar\omega(^{\boldsymbol{\kappa}}_\nu)/k_B\theta\right)}{\left[\exp\left(\hbar\omega(^{\boldsymbol{\kappa}}_\nu)/k_B\theta\right) - 1\right]^2}, \tag{3.9}$$

where V is the volume of the simulation domain.

The NMD utilises the basic concept of projecting the atomic trajectories coming from an equilibrium MD simulation onto the normal mode coordinates of the system using Fourier transformation technique. Briefly, the phonon lifetimes can be obtained as follows. The time derivative of the normal mode coordinate, $\dot{Q}(^{\boldsymbol{\kappa}}_\nu; t)$, is given by

$$\dot{Q}(^{\boldsymbol{\kappa}}_\nu; t) = \sum_{\alpha, b, l}^{3, n, N} \sqrt{\frac{m_b}{N}} \dot{u}_\alpha \left(^l_b; t\right) e^*(^{\boldsymbol{\kappa}\,b}_{\nu\,\alpha}) \exp\left[i\boldsymbol{\kappa} \cdot \boldsymbol{r}_0 \left(^l_0\right)\right], \tag{3.10}$$

where n and N are number of atoms in a unit cell and total number of unit cells, respectively. And, $e^*(^{\boldsymbol{\kappa}\,b}_{\nu\,\alpha})$ represents the time-independent eigenvectors of normal modes, m_b is the mass of the bth atom residing inside the lth unit cell while $\boldsymbol{r}_0(l, 0)$ is the equilibrium position vector of the lth unit cell and $\dot{u}_\alpha \left(^l_b; t\right)$ is the α-component of velocity of this b^{th} atom at time t, where integer α index varies from 1 to 3.

Once the set of atomic velocities from the MD simulation and phonon mode eigenvectors $e^*(^{\boldsymbol{\kappa}\,b}_{\nu\,\alpha})$ for different allowed wave vectors [83], calculated with the help of GULP [140], are obtained, the phonon SED for a given mode is derived as [141]

$$\Phi(^{\boldsymbol{\kappa}}_\nu; \omega) = \lim_{\tau_0 \to \infty} \frac{1}{\tau_0} \left| \frac{1}{\sqrt{2\pi}} \int_0^{\tau_0} \dot{Q}\left(^{\boldsymbol{\kappa}}_\nu; t\right) \exp(-i\omega t)\, dt \right|^2. \tag{3.11}$$

With the help of the anharmonic LD theory and the Wiener-Khinchin theorem [141, 83],

31

it can further be shown that the phonon SED for a given mode is

$$\Phi(^{\boldsymbol{\kappa}}_{\nu};\omega) = \frac{I}{1 + \left[\frac{\omega - \omega_0(^{\boldsymbol{\kappa}}_{\nu})}{\Gamma(^{\boldsymbol{\kappa}}_{\nu})}\right]^2}, \tag{3.12}$$

where I is intensity of the Lorentzian peak whose center lies at $\omega_0(^{\boldsymbol{\kappa}}_{\nu})$ with its line width $\Gamma(^{\boldsymbol{\kappa}}_{\nu})$ equal to $1/2\tau(^{\boldsymbol{\kappa}}_{\nu})$. Now, $\Phi(^{\boldsymbol{\kappa}}_{\nu};\omega)$ is calculated with the help of Eq. (3.11) and the data as a function of ω is fit to the Lorentzian function in Eq. (3.12) to extract $\omega_0(^{\boldsymbol{\kappa}}_{\nu})$ and $\tau(^{\boldsymbol{\kappa}}_{\nu})$. It should be noted that the lifetimes obtained by this SED technique contains both the normal and the Umklapp scattering processes.

3.3 Green-Kubo

The Green-Kubo technique, based on linear response theory and the fluctuation-dissipation theorem, uses time autocorrelation functions (ACF) to characterize the system's behavior. In equilibrium molecular dynamics (EMD), dynamic properties such as thermal conductivity are calculated using these principles, where the heat flow in an equilibrium system fluctuates around zero. Heat flux vectors and their correlations are computed throughout the simulations, and the time required for the Heat Auto-Correlation Functions (HACF) to decay to zero is used through the Green–Kubo relation to predict the thermal conductivity. Statistical thermodynamics coupled with extensive algebra, resulting in the following equation for thermal conductivity [142]:

$$\mathrm{k}_{\alpha\beta} = \lim_{\tau_\mathrm{I} \to \infty} \frac{1}{\mathrm{k_B V T^2}} \int_0^{\tau_\mathrm{I}} \langle \mathrm{J}_\alpha(0) \otimes \mathrm{J}_\beta(\mathrm{t}) \rangle \mathrm{dt}, \tag{3.13}$$

where $\mathrm{k_B}$ is the Boltzmann constant, V and T are the system volume and temperature, respectively, $\tau_I (= I\Delta t_{MD})$ is the integration timestep, Δt_{MD} is the time step in the molecular dynamics simulation and I is the total integration steps. J_α is the α component of the lattice heat current vector **J** which is defined as

$$\mathbf{J}(t) = \frac{d}{dt} \sum_i \mathbf{R}_i E_i = \sum_i E_i \mathbf{v}_i + \sum_i \mathbf{R}_i \frac{dE_i}{dt}, \qquad (3.14)$$

where, $\mathbf{R}_i$, $\mathbf{v}_i$, and E_i represent the position vector, velocity, and the total energy (including both potential and kinetic) of atom i. The first term on the right-hand side of Eq. (3.14) accounts for atomic diffusion, commonly referred to as the convection term. The second term represents the correlation of energy transfer between neighbouring atoms [143]. The $\langle \mathbf{J}_\alpha(0) \otimes \mathbf{J}_\alpha(t) \rangle$ is the ensemble averaged HCACF.

In MD , time is discrete, so the integral becomes a sum over discrete time steps, and the HCACF is computed numerically. The Eq. (3.15) reflects this discretization and adds a statistical averaging approach to improve accuracy where averaging over multiple time origins (starting points for the autocorrelation function) helps reduce noise in the computed thermal conductivity.

$$\mathbf{k} = \lim_{\substack{S,I \to \infty \\ S \gg I}} \frac{\Delta t_{\mathrm{MD}}}{V k_{\mathrm{B}} T^2} \sum_{a=1}^{I} \frac{1}{S-a} \sum_{b=1}^{S-a} \mathbf{J}_{a+b} \otimes \mathbf{J}_b \qquad (3.15)$$

Eq. (3.15) is a discrete form of the GK relation for calculating thermal conductivity (k) from molecular dynamics (MD) simulations where, $\mathbf{J}_{a+b}$ and $\mathbf{J}_b$ are heat current vectors at time steps $a+b$ and b, respectively. When $S \gg I$, it ensures enough independent data points from the long-time series to average over, improving the statistical reliability of the results. The inner sum with a factor $\frac{1}{S-a}$ represents the ensemble average and the outer sum represents the integration in time.

The following table gives a brief description and comparison of the above mentioned MD-based techniques.

Criteria	NEMD	NMD	GK
Type of Method	Non-equilibrium, Direct Method	Equilibrium, Normal Mode Analysis	Equilibrium, Auto-correlation Function
Boundary Conditions	Requires thermal gradient, temperature boundary conditions	Periodic boundary conditions	Periodic boundary conditions
System Size Dependence	Thermal conductivity is length and width dependent	System-size independent in terms of calculated phonon properties	Size-dependent and requires long simulation times for convergence
Key Output	One component of **k** tensor	Phonon lifetimes, group velocities and full **k** tensor	Full **k** tensor
Accuracy	Can be affected by system size and non-linear temperature gradients	High accuracy due to detailed phonon mode analysis	High, but requires accurate correlation decay and long timescales
Method Limitation	May not capture all scattering processes, e.g., Umklapp scattering	Limited temperature range as it assumes harmonic lattice dynamics	Limited by noise in the autocorrelation function, long times required for accurate decay
Time Scale Requirement	Requires steady-state conditions to be achieved, moderate timescale	Long simulations required for accurate phonon mode decomposition	Long simulation time required for decay of autocorrelation functions
Physical Insights	Provides a straightforward interpretation of heat conduction following Fourier's law	Offers insights into mode-specific heat transport mechanisms	Directly links equilibrium fluctuations to macroscopic thermal properties

Table 3.1: Comparison summary of NEMD, NMD, and GK methods for TC Calculation

Chapter 4

A Consistent Comparison of Lattice Thermal Conductivities and Phonon Properties of Single Layer and Bilayer Graphene Systems

In the present chapter, we study the size-dependent thermal transport in suspended SLG, AB-BLG and tBLG with a twist angle of $21.78°$ samples with the help of robust and consistent NEMD [48, 49] simulations based direct method and normal mode decomposition (NMD) analysis based SED method [144, 145, 146, 83]. Our work partially overlaps with the work done by Chen and Kumar [50], Qiu and Ruan [51, 52], Park et al. [47] and Zou et al. [53] for the SLG samples and Chenyang Li [63], Nie et al. [66] and Liu et al. [67] for the BLG samples, however, there are significant differences. Chen and Kumar [50] neglect the anisotropy in the phonon dispersion in the full Brillouin zone (BZ) in their relaxation time approximation approach whereas we sample all the available normal modes in the BZ without neglecting the anisotropy.

On the other hand, Qiu and Ruan [51, 52] and Zou et al. [53] adopt the alternative phonon SED Φ' [147] approach for the extraction of spectral phonon relaxation times which does not involve eigenvectors and, therefore, does not represent the phonon spectral energy [147] and leads to more scattering in the relaxation time calculation. We perform lattice dynamics (LD) calculations with the help of the GULP [140] package, calculate eigenvector for each phonon mode and extract the phonon relaxation times from the LD theory based SED Φ approach [147]. With regard to direct method based NEMD work, we calculate the heat flux using Irving and Kirkwood's [41] expression whose derivation is based upon the mass, momentum and energy balance equations by means of the Liouville equation based classical statistical mechanics. This is in contrast to Park et al. [47] and Liu et al. [67], who use the TWD method for calculating the heat flux in the NEMD direct method setting. With the help of thermodynamic arguments and our own NEMD simulations, we show that this method does not provide correct heat flux. Chenyang Li et al. [63] adopt an inconsistent approach in the sense that they calculated the bulk TCs of AB-BLG and tBLG samples with the NEMD direct method using classical interatomic potentials, however, the calculation of phonon lifetimes was achieved with the help of the DFT based ShengBTE package. Nie et al. [66] set up the temperature gradient using the Langevin thermostats but do not mention the method for calculating the heat flux in their NEMD direct method setting.

In the earlier Section 3.1 and 3.2 we described the methodology for the NEMD direct method and the SED method. The latter calculates the thermal conductivity in the BTE framework by adopting the relaxation time approximation approach. The phonon relaxation times are obtained by fitting the SED curves to the Lorentzian function. In Section 4.1, we prepare the samples, perform the direct method simulations and other MD simulations required for the SED analysis over different sizes of suspended SLG, AB-BLG and $21.78°$ tBLG systems. In Section 4.2, we discuss the results obtained for the NEMD and SED methods and also provide a critique of the TWD method used for the calculation of the heat flux. We also obtain bulk TCs of three graphene systems using the NEMD direct and SED methods. Finally, we conclude in Section 4.3 with a summary and suggestions for future work.

4.1 Sample Preparation

Firstly, in this chapter the two methods (direct and NMD method) have been used to get the TC for the SLG, AB-BLG and tBLG systems. The direct method (see Section 3.1) is based on NEMD simulations and the NMD method (see Section 3.2) is based on both equilibrium MD simulations and lattice dynamics calculations. Like many workers cited in Section 2.2, we also model the intralayer C-C interactions of the suspended SLG, AB-BLG and $21.78°$ tBLG systems using the optimized Tersoff [40] potential and the interlayer C-C interactions using an LJ pair potential with LJ parameters $\sigma = 3.34$ Å and $\epsilon = 2.96$ meV [63]. The cutoff radius was taken to be $r_{\text{cut}} = 3\sigma = 10.02$ Å. Next, we describe the construction of SLG and BLG samples. The two planar lattice vectors taken for the formation of the primitive unit cell of the SLG samples are $\boldsymbol{a}_1 = a\hat{\mathbf{i}}$ and $\boldsymbol{a}_2 = a(\cos 60°\hat{\mathbf{i}} + \sin 60°\hat{\mathbf{j}})$ in Å, where $\hat{\mathbf{i}}$ and $\hat{\mathbf{j}}$ are unit vectors along x and y axes, respectively, as shown in Fig. 4.1a, and lattice constant $a = 2.492$ Å . The choice of such lattice parameter value depends upon the choice of interatomic potential and comes from the work of Lindsay and Broido [40]. The construction of commensurate tBLG labelled by (M, N) is achieved by stacking two graphene layers with a twist (misorientation) angle α [148], where M and N are non-negative integers. The upper layer has the commensurate primitive superunit cell defined by two vectors, $\boldsymbol{c}_{U1} = N\boldsymbol{a}_1 + M\boldsymbol{a}_2$ and $\boldsymbol{c}_{U2} = -M\boldsymbol{a}_1 + (M+N)\boldsymbol{a}_2$, followed by an anticlockwise twist rotation with an angle $\alpha/2 - \pi/6$ along z-axis. The lower layer is constructed by the superunitcell vectors defined by $\boldsymbol{c}_{L1} = M\boldsymbol{a}_1 + N\boldsymbol{a}_2$ and $\boldsymbol{c}_{L2} = -N\boldsymbol{a}_1 + (M+N)\boldsymbol{a}_2$, followed by a clockwise twist rotation with an angle $\alpha/2 + \pi/6$ along z-axis. This makes sure that the twist angle α becomes

$$\alpha = \arccos\left(\frac{N^2 + 4NM + M^2}{2(N^2 + NM + M^2)}\right). \tag{4.1}$$

The initial distance between the two layers is kept at 3.34 Å. Thus, we obtain a commensurate tBLG unit cell with cell size $L_{\text{cell}} = a\sqrt{N^2 + NM + M^2}$ such that the top or the bottom view represents a parallelogram as shown in Figs. 4.1b–4.1c, defined by two vectors $\boldsymbol{p}_1 = L_{\text{cell}}\hat{\mathbf{i}}$ and $\boldsymbol{p}_2 = L_{\text{cell}}(\cos 60°\hat{\mathbf{i}} + \sin 60°\hat{\mathbf{j}})$. In this framework, SLG samples

(a) SLG
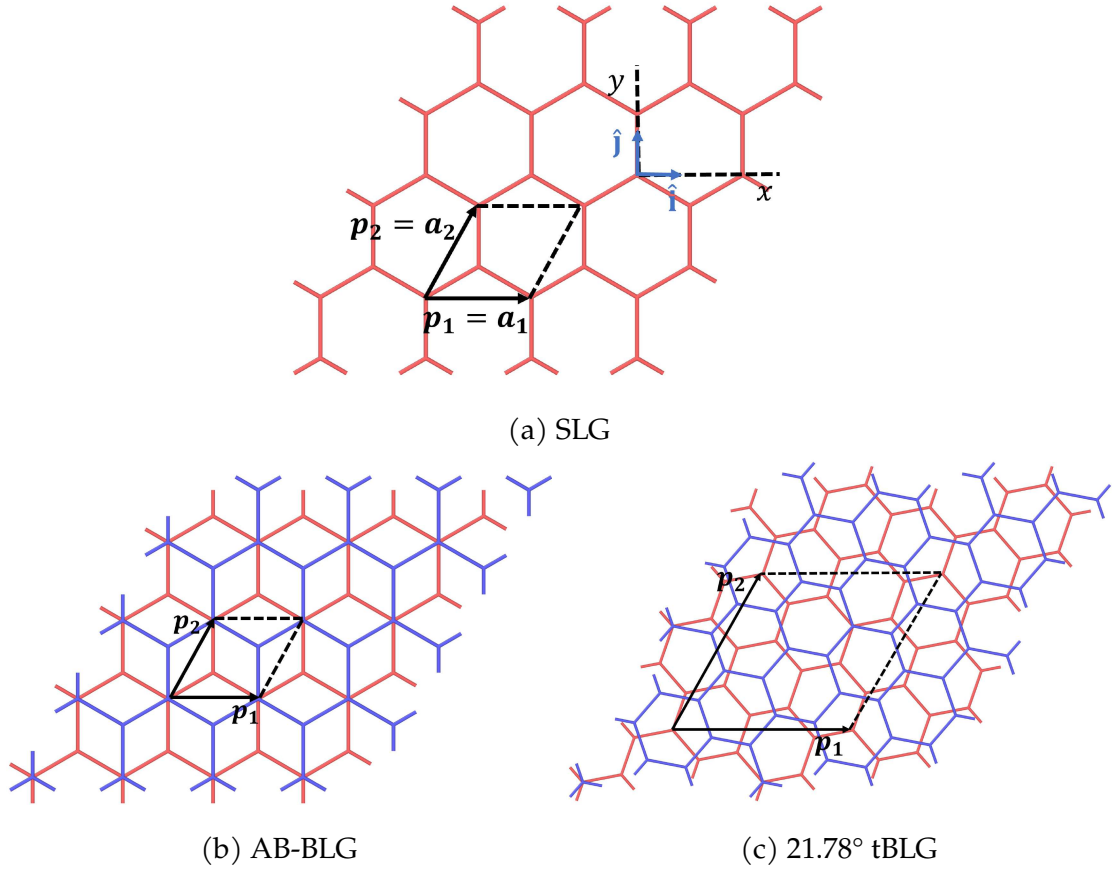
(b) AB-BLG

(c) 21.78° tBLG

Figure 4.1: The primitive unit cells for (a) SLG (b) AB-BLG, and (c) 21.78° tBLG such that the resultant parallelogram can be defined by two vectors $\boldsymbol{p}_1 = L_{\text{cell}}\hat{\mathbf{i}}$ and $\boldsymbol{p}_2 = L_{\text{cell}}(\cos 60°\hat{\mathbf{i}} + \sin 60°\hat{\mathbf{j}})$.

are $(1,0)$ samples with only the lower layer whose unit cells are defined by $\boldsymbol{p}_1 = a\hat{\mathbf{i}}$ and $\boldsymbol{p}_2 = a(\cos 60°\hat{\mathbf{i}} + \sin 60°\hat{\mathbf{j}})$. AB-BLG samples are labeled as $(M, N) \equiv (1, 0)$ with the twist angle $\alpha = 0°$ in AB-stacked sense, whereas $21.78°$ tBLG samples are labeled as $(M, N) \equiv (2, 1)$ with the twist angle $\alpha = 21.78°$. The reason for choosing $21.78°$ as the twist angle in bilayer graphene system is because the commensurate tBLG unit cell size given by $L_{\mathrm{cell}} = a\sqrt{N^2 + NM + M^2}$ is smallest for this angle where $(M, N) \equiv (2, 1)$ [148]. This gives $L_{\mathrm{cell}} = 6.593$ Å , which has a total of 28 atoms in the commensurate unit cell. Choosing such a unit cell makes the thermal properties investigation computationally affordable for the spectral energy density(SED) based normal mode decomposition(NMD) analysis.

The simulations for the SED method have the configurations defined by the primitive unit cells as shown in Figs. 4.1a–4.1c. On the other hand, the NEMD direct method simulations are done on rectangular nanoribbons such that their lengths, widths and heights are along x, y and z-axes which coincide with $\boldsymbol{p}_1$, $2\boldsymbol{p}_2 - \boldsymbol{p}_1$ and $\hat{\mathbf{k}}$ directions, where $\hat{\mathbf{k}}$ is a unit vector along z-axis. The temperature gradient and the corresponding heat flux are developed along the x-axis which in the case of SLG samples coincides with the zig-zag direction.

The MD package LAMMPS [149] has been used for all our simulations. We have modified the code such that temperature and heat flux for each bin have been calculated after removing rigid-body translation as suggested by Jellinek and Li [136, 48].

4.2 Results

4.2.1 NEMD

The left and the right end regions with 1 Å width for all SLG, AB-BLG and tBLG samples are kept fixed. On the remaining innercore region, the binning is done as described in Section 3.1 and an initialization stage is first performed for all simulations during which the region is equilibrated to 300 K. Free BCs are applied in all directions and the MD time step is set as $\Delta t_{\mathrm{MD}} = 1$ fs. The velocities of the atoms are adjusted to

ensure zero linear and angular momentum of the system. After this, the nanoribbon is evolved for 80 ps subject to NVT conditions with the temperature set to $\theta = 300$ K using a Nose-Hoover chain thermostat (chain-length = 3) for the first 40 ps and then using the Langevin thermostat for the next 40 ps. This is enough for bringing the whole innercore region to equilibrated temperature, which is followed by setting a temperature gradient across the length of the region by thermostatting the two end bins only and evolving the rest of the region atoms under NVE conditions for another 40 ps. Thus, the left (first) and the right (last) end bins are thermostatted at $\theta_L = 280$ K and $\theta_R = 320$ K, respectively, with the help of the Langevin dynamics so that the average temperature of the innercore region remains at 300 K. Once the non-equilibrium steady-state is achieved with a temperature gradient, the system is run under this condition for another $t_{ss} = 2000$ ps, during which the instantaneous temperature and heat flux are calculated for all bins and averaged over time to obtain the phase averages using Eq. (3.6), which are then used to calculate the size-dependent TCs in Eq. (3.7).

For a typical example to show the results of the method, we consider an SLG nanoribbon of size 800×500 Å^2 with $N_{bins} = 11$ and 89412 atoms.

As shown in Fig. 4.2a, the temperature profile is almost linear away from the thermostats (three bins on either ends), barring the Kapitza jump [49] observed near the thermostatted regions. The average of the heat flux values obtained for these bins, shown in Fig. 4.2b from bin number 4 to 8, is taken in Eq. (3.7) for the TC calculation. Having obtained a size-dependent TC of a given sample, we keep increasing the width so that a width-convergent TC can be obtained. For a constant length of 20 nm along x-axis, the converged values for widths are 50, 30 and 30 nm, respectively, for SLG, AB-BLG and $21.78°$ tBLG samples. Figure 4.3 shows the TCs of SLG, AB-BLG and $21.78°$ tBLG nanoribbons as the width L_y increases. This exercise is followed by keeping the widths at their converged values and increasing the length of the samples. The TCs obtained as a function of length have been shown in Fig. 4.4a.

These values are used in extrapolating the TC with the help of the following model:

$$\frac{1}{k} = \frac{1}{k_\infty} + \frac{c}{L_x}, \tag{4.2}$$
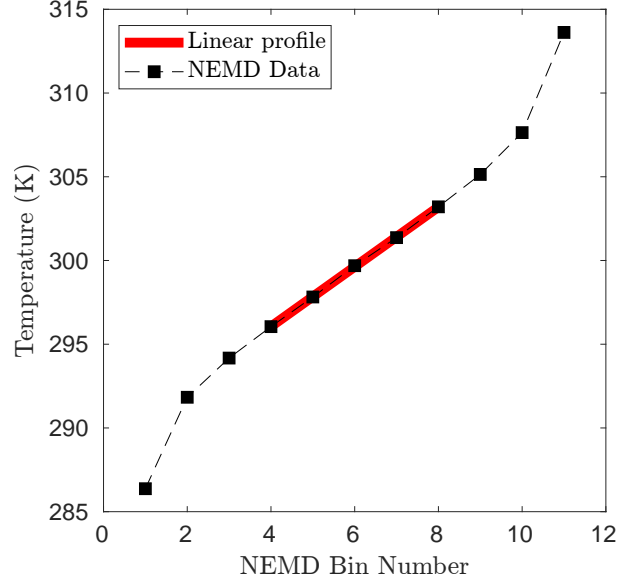
(a) Temperature
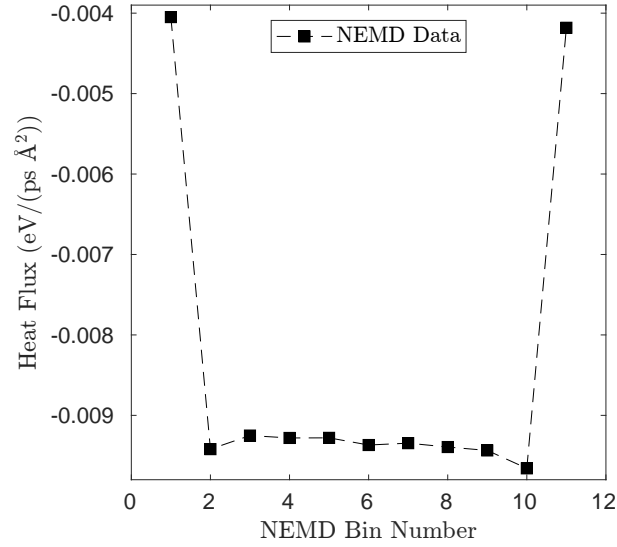
(b) Heat flux

Figure 4.2: Steady-state (a) temperature, and (b) heat flux profile for an SLG nanoribbon of size 800×500 Å . The nanoribbon is partitioned into $N_{\text{bins}} = 11$ bins and the first and the eleventh bin are thermostatted. The heat flux has been calculated with the Irving-Kirkwood (I-K) procedure as described in 3.2.
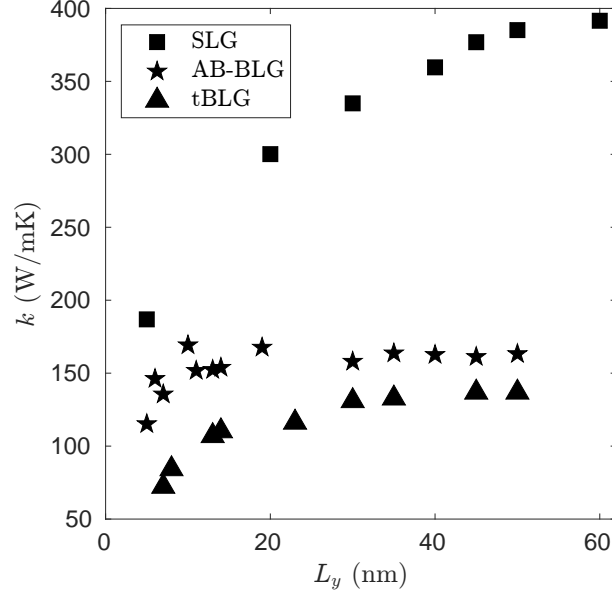
Figure 4.3: Width convergence of k (W/mK) for SLG, AB-BLG and tBLG samples. The length along x-axis (L_x) is 20 nm for all the samples.

where c is a constant and L_x is length of the sample. The model suggests fitting a linear plot between $\frac{1}{L_x}$ and $\frac{1}{k}$ so that the intercept at the y-axis gives the bulk TC, k_∞. Fig. 4.4b presents this linear fitting for all three systems. The bulk TCs obtained by this extrapolation are 1287.2, 582.8, 389.7 W/mK for the SLG, AB-BLG and tBLG samples, respectively. The bulk TC can also be obtained by the size-dependent TC expression suggested by Alvarez and Jou [150], who included memory and nonlocal effects within the framework of extended irreversible thermodynamics in their study of transition of heat transport from diffusive to ballistic and came up with the following expression:

$$k(L_x) = \frac{k_\infty L_x^2}{2\pi^2 l^2} \sqrt{\left(1 + \frac{4\pi l}{L_x}\right)^2 - 1}, \tag{4.3}$$

where k_∞ is the bulk TC and l is the mean free path of phonons in an average sense. As shown in Fig. 4.4a, the length-dependent TCs data fit nicely over the expression in Eq. (4.3), which provides the values of the bulk TCs (k_∞) close to 842.2, 435.5 and 306.8 W/mK and the values of l close to 172 nm, 134 nm and 112 nm for SLG, AB-BLG and tBLG samples, respectively. These values are smaller than those reported by Park et al. [47] for SLG samples, most likely, because of the heat flux and the temperature gradient calculated with the help of the TWD method which we critique below.

$$k(L_x) = \frac{k_\infty L_x^2}{2\pi^2 l^2}\sqrt{\left(1 + \frac{4\pi l}{L_x}\right)^2 - 1}$$
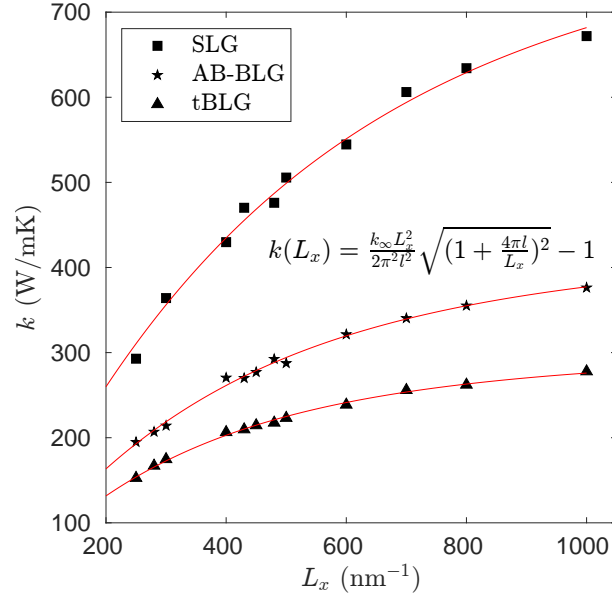
(a) TC vs length
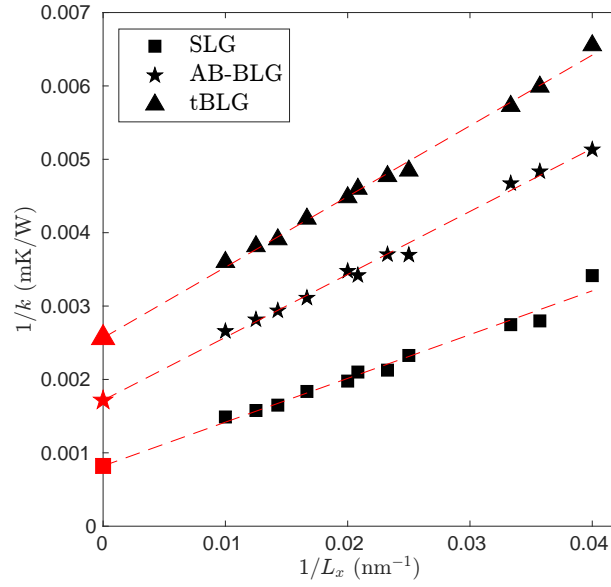
(b) Extrapolated bulk TC

Figure 4.4: (a) Thermal conductivity k as a function of length L_x at 300 K, (b) $\frac{1}{k}$ vs $\frac{1}{L_x}$ data points and the linear plots estimating the bulk TCs based upon the extrapolation.

4.2.2 Thermostat Work Done

In several works such as Park et al. [47], Liu et al. [67] and many others, the rate of energy added or subtracted to the thermostat per unit area is taken as the heat flux in the system. We show its incorrectness through thermodynamic arguments and our own simulations. We consider three regions in a system under the NEMD direct method setting as discussed above, the first bin (cold thermostatted left region), the last bin (hot thermostatted right region) and the region comprising bin number $n = 2$ to $n = N_{\text{bins}} - 1$, named as the middle region. We use the indices L, R and M to denote these regions, which are also used as subscripts to define the properties of the regions. If the rate of change of total energy of any of these regions is $\dot{\mathcal{E}}_i$, the rate of heat supplied is $\dot{\mathcal{Q}}_i$ and the rate of external work done on the region is $\dot{\mathcal{W}}_i$, where $i = L, R, M$, then the first law of thermodynamics states that $\dot{\mathcal{E}}_i = \dot{\mathcal{Q}}_i + \dot{\mathcal{W}}_i$. In the time average sense, where $\overline{\mathcal{P}} = \frac{1}{t} \int_0^t \mathcal{P} dt$, and $\mathcal{P} = \mathcal{E}, \mathcal{W}, \mathcal{Q}$ are different properties, we have

$$\overline{\dot{\mathcal{E}}}_i = \overline{\dot{\mathcal{Q}}}_i + \overline{\dot{\mathcal{W}}}_i, \quad i = L, R, M. \tag{4.4}$$

The thermostat (hot or cold infinite reservoir) acts as a surrounding to the thermostatted bins, which supplies heat to or extracts heat from the first and the last bin, respectively, and also does external work on the thermostatted bins. We use the subscript c and h to describe these thermostats. Moreover, the middle region acts as another surrounding for the left and the right regions and vice versa. This means, using Eq. (4.4), we have

$$\overline{\dot{\mathcal{E}}}_L = \overline{\dot{\mathcal{Q}}}_{c \to L} + \overline{\dot{\mathcal{W}}}_{c \to L} + \overline{\dot{\mathcal{Q}}}_{M \to L} + \overline{\dot{\mathcal{W}}}_{M \to L}, \tag{4.5a}$$

$$\overline{\dot{\mathcal{E}}}_R = \overline{\dot{\mathcal{Q}}}_{h \to R} + \overline{\dot{\mathcal{W}}}_{h \to R} + \overline{\dot{\mathcal{Q}}}_{M \to R} + \overline{\dot{\mathcal{W}}}_{M \to R}, \tag{4.5b}$$

$$\overline{\dot{\mathcal{E}}}_M = \overline{\dot{\mathcal{Q}}}_{L \to M} + \overline{\dot{\mathcal{W}}}_{L \to M} + \overline{\dot{\mathcal{Q}}}_{R \to M} + \overline{\dot{\mathcal{W}}}_{R \to M}, \tag{4.5c}$$

where the subscript $a \to b$ has been used to denote that the heat is being supplied from the region a to the region b or the work is being done by a on b, where $a, b = L, R, M, c, h$. We are actually interested in calculating the heat flux in the middle region, therefore the

term of interest in the above system of equations is $\overline{\dot{\mathcal{Q}}}_{L \to M}$ or $\overline{\dot{\mathcal{Q}}}_{M \to R}$ divided by cross-sectional area A. The temperature gradient is along x-axis, therefore, all of this heat flux can be thought of existing only along x-axis, and then we will also have $\overline{\dot{\mathcal{Q}}}_{L \to M} = \overline{\dot{\mathcal{Q}}}_{M \to R}$. We use this relation and also the definition that $\overline{\dot{\mathcal{Q}}}_{M \to L} = -\overline{\dot{\mathcal{Q}}}_{L \to M}, \overline{\dot{\mathcal{Q}}}_{M \to R} = -\overline{\dot{\mathcal{Q}}}_{R \to M}$, and subtract Eq. (4.5b) from Eq. (4.5a) to obtain

$$2\overline{\dot{\mathcal{Q}}}_{M \to R} = \left(\overline{\dot{\mathcal{Q}}}_{c \to L} - \overline{\dot{\mathcal{Q}}}_{h \to R} \right) + \left(\overline{\dot{\mathcal{W}}}_{M \to L} - \overline{\dot{\mathcal{W}}}_{M \to R} \right)$$
$$+ \left(\overline{\dot{\mathcal{W}}}_{c \to L} - \overline{\dot{\mathcal{W}}}_{h \to R} \right) - \left(\overline{\dot{\mathcal{E}}}_L - \overline{\dot{\mathcal{E}}}_R \right). \tag{4.6}$$

It turns out that the last two terms appearing on the right hand side of Eq. (4.6) can be easily calculated in the following manner.

The equation of motion of atoms in a bin under a Langevin thermostat is described as

$$m_i \ddot{\boldsymbol{r}}_i = \boldsymbol{f}_i + \boldsymbol{F}_i^D + \boldsymbol{F}_i^R, \tag{4.7}$$

where m_i is the mass of ith atom in the bin, $\ddot{\boldsymbol{r}}_i$ is the acceleration of the atom whose position vector is $\boldsymbol{r}_i$, $\boldsymbol{f}_i$ is the interatomic force derived from the gradient of the total interatomic potential energy of the system acting on i^{th} atom due to all other atoms in the system, $\boldsymbol{F}_i^D = -\gamma m_i \dot{\boldsymbol{r}}_i$ is the Langevin drag force, γ is the damping coefficient, and $\boldsymbol{F}_i^R$ is the Langevin random force. The drag and random forces are external forces on the atoms of the bin. Therefore, the rate of external work done by the Langevin thermostat on the bin is

$$\dot{\mathcal{W}} = \sum_{i=1}^{N_n} (\boldsymbol{F}_i^D + \boldsymbol{F}_i^R) \cdot \boldsymbol{v}_i, \tag{4.8}$$

where summation is over all the atoms in the bin. The research works utilizing TWD method depends upon the LAMMPS option "*tally yes*" in the LAMMPS fix "*fix langevin*" to calculate accumulated energy added to the system due to the thermostat. This option cumulatively adds $\sum_{i=1}^{N_n} (\boldsymbol{F}_i^D + \boldsymbol{F}_i^R) \cdot \boldsymbol{v}_i \Delta t_{\text{MD}}$ in each MD time step and prints the accumulated sum as a fix output. Looking at this expression and comparing it with

Eq. (4.8), it is clear that it does not calculate accumulated energy $\int_0^t \dot{\mathcal{E}} dt$ but it actually calculates accumulated work done $\int_0^t \dot{\mathcal{W}} dt$, where t is the current time starting from the time when the LAMMPS fix is invoked with "*tally yes*". The method, further, incorrectly assumes that the average rate of the work done by the thermostat per unit area, which is mistaken as the average rate of accumulated energy added to the bin per unit area, is the heat flux in the system. In other words, LAMMPS fix "*fix langevin*" with the option "*tally yes*" is used to calculate the average rate of work done, $\overline{\dot{\mathcal{W}}}(t)$, as

$$\overline{\dot{\mathcal{W}}}(t) = \frac{1}{t} \int_0^t \dot{\mathcal{W}} dt = \frac{\overline{\Delta \mathcal{W}}}{t} = \frac{1}{t} \sum_{j=1}^{N_t} \dot{\mathcal{W}}^j \Delta t_{\mathrm{MD}}, \qquad (4.9)$$

where $\overline{\Delta \mathcal{W}}$ is the accumulated work done, $\dot{\mathcal{W}}^j$ is the rate of work done at j^{th} MD time step, $\dot{\mathcal{W}}^j = \dot{\mathcal{W}}(j\Delta t_{\mathrm{MD}})$, and N_t is the total number of MD steps after the "*tally yes*" option has been invoked such that $t = N_t \Delta t_{\mathrm{MD}}$. This means $\overline{\dot{\mathcal{W}}}_{c \to L}$ and $\overline{\dot{\mathcal{W}}}_{h \to R}$ appearing in Eq. (4.6) can be calculated. Also, the change of energy of nth bin as a function of time is given by $\Delta \mathcal{E}_n(t) = \mathcal{E}_n(t) - \mathcal{E}_0$, where $\mathcal{E}_0$ is the energy of the bin under equilibrium NVE ensemble before the application of the thermostat, which involves both potential and kinetic energies. For our MD simulations, the corresponding average rate of energy change is

$$\overline{\dot{\mathcal{E}}}(t) = \frac{\overline{\Delta \mathcal{E}}}{t} = \frac{1}{t} \sum_{j=1}^{N_t} \Delta \mathcal{E}^j, \qquad (4.10)$$

where $\overline{\Delta \mathcal{E}}$ is the accumulated energy change, $\Delta \mathcal{E}^j$ is the energy change from equilibrium NVE ensemble at j^{th} MD time step after the '*tally yes*" option has been invoked. Thus, $\overline{\dot{\mathcal{E}}}_L$ and $\overline{\dot{\mathcal{E}}}_R$ can also be calculated. Now, if we divide Eq. (4.6) by the cross-sectional area A, then the average heat flux in the system, $\langle q \rangle = \overline{\dot{\mathcal{Q}}}_{M \to R}/A$, can be calculated as

$$\langle q \rangle = \frac{1}{2A} \left[\left(\overline{\dot{\mathcal{Q}}}_{c \to L} - \overline{\dot{\mathcal{Q}}}_{h \to R} \right) + \left(\overline{\dot{\mathcal{W}}}_{M \to L} - \overline{\dot{\mathcal{W}}}_{M \to R} \right) \right.$$
$$\left. + \left(\overline{\dot{\mathcal{W}}}_{c \to L} - \overline{\dot{\mathcal{W}}}_{h \to R} \right) - \left(\overline{\dot{\mathcal{E}}}_L - \overline{\dot{\mathcal{E}}}_R \right) \right]. \qquad (4.11)$$

This could be another method to calculate the same average heat flux that appeared in Eq. (3.7). On the contrary, the TWD method defines the average heat flux as

$$\langle q \rangle_{\mathrm{TWD}} = \frac{1}{2A} \left[\overline{\dot{\mathcal{W}}}_{c \to L} - \overline{\dot{\mathcal{W}}}_{h \to R} \right] . \tag{4.12}$$

Comparing Eqs. (4.11) and (4.12), we get

$$\langle q \rangle = \langle q \rangle_{\mathrm{TWD}} + \langle q \rangle_c , \tag{4.13}$$

where

$$\langle q \rangle_c = \frac{1}{2A} \left[\left(\overline{\dot{\mathcal{Q}}}_{c \to L} - \overline{\dot{\mathcal{Q}}}_{h \to R} \right) + \left(\overline{\dot{\mathcal{W}}}_{M \to L} - \overline{\dot{\mathcal{W}}}_{M \to R} \right) - \left(\overline{\dot{\mathcal{E}}}_L - \overline{\dot{\mathcal{E}}}_R \right) \right] \tag{4.14}$$

is the correction term. With the help of the NEMD direct method simulation described in Section 4.2.1 over SLG nanoribbons of size 110×30 Å^2 (smaller sample) and 800×500 Å^2 (bigger sample), we now show that the average heat flux, $\langle q \rangle$, calculated using the I-K procedure as described in Section 3.2 is not equal to $\langle q \rangle_{\mathrm{TWD}}$ in Eq. (4.12). In other words, if $\langle q \rangle$ in Eq. (4.11) is the same as the I-K average heat flux in Eq. (3.7), then $\langle q \rangle_c$ in Eq. (4.13) is not equal to zero.

The accumulated energy change, $\overline{\Delta \mathcal{E}}$, and the accumulated work done by the thermostats, $\overline{\Delta \mathcal{W}}$, for both the left and the right regions in the SLG nanoribbon of size 800×500 Å^2 have been shown in Fig. 4.5 with time. We obtain similar curves for the size 110×30 Å^2. These curves help us generate $(\overline{\Delta \mathcal{E}}_L - \overline{\Delta \mathcal{E}}_R)$ and $(\overline{\Delta \mathcal{W}}_L - \overline{\Delta \mathcal{W}}_R)$ curves with respect to time. When fitted with straight lines, their slopes give us the values of $(\overline{\dot{\mathcal{W}}}_{c \to L} - \overline{\dot{\mathcal{W}}}_{h \to R})$ and $(\overline{\dot{\mathcal{E}}}_L - \overline{\dot{\mathcal{E}}}_R)$, as suggested by Eqs. (4.9) and (4.10). Divided by the cross-sectional area $A = 30 \times 3.34$ Å^2 for the smaller sample and 500×3.34 Å^2 for the bigger sample, and again divided by 2, we obtain $\langle q \rangle_{\mathrm{TWD}} = -3.736 \times 10^{-3}, -12.917 \times 10^{-3}$ eV/(Å^{2}ps), respectively, for smaller and bigger samples. The corresponding values for the heat flux obtained through the I-K procedure are $\langle q \rangle = -2.845 \times 10^{-3}, -9.501 \times 10^{-3}$ eV/(Å^{2}ps), respectively for two sizes, where the average heat flux is the average of the heat flux values for bin number 4 to 8, as shown in Fig. 4.2a. Since the
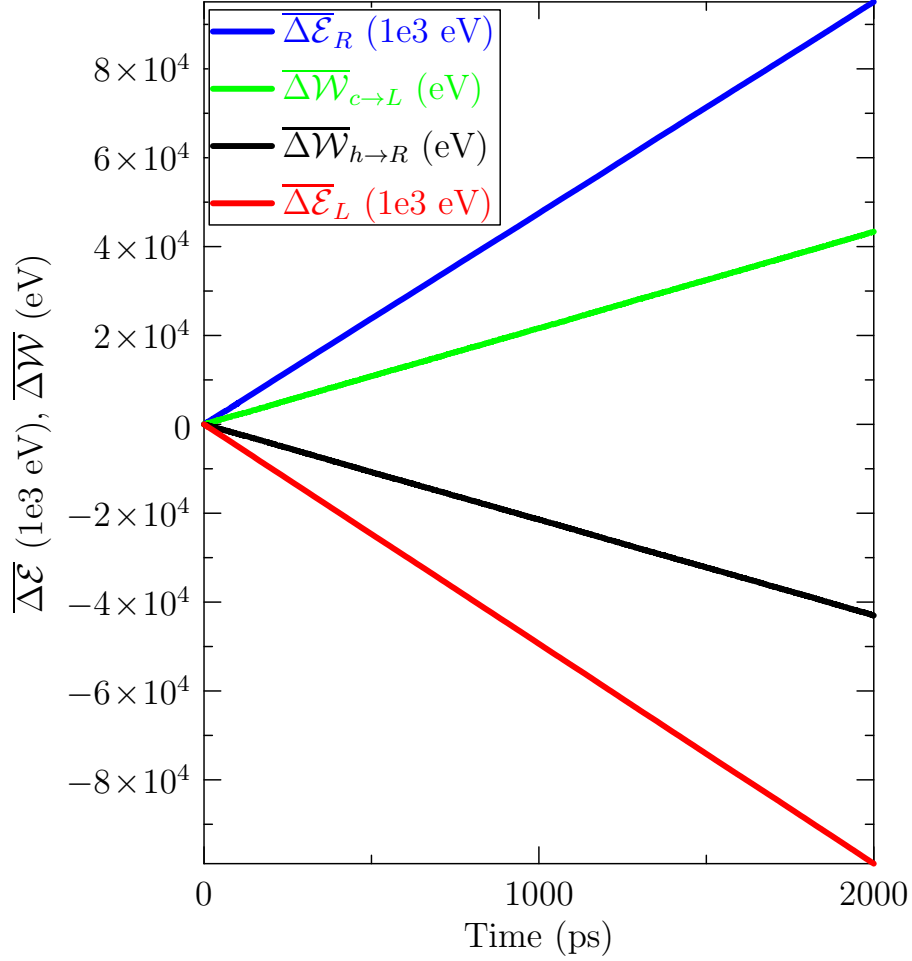
Figure 4.5: (a) For an SLG sample of size 800×500 Å^2, accumulated energy change, $\overline{\Delta \mathcal{E}}$, of the left (cold thermostatted at 280 K) and the right (hot thermostatted at 320 K) regions with respect to time have been shown by the red and the blue curves, respectively. The accumulated work done, $\overline{\Delta \mathcal{W}}$, on the left and the right regions by the thermostats have been shown by the green and the black curves, respectively.

temperature gradient in the linear regime away from the thermostats (e.g. see Fig. 4.2b) is the same for both the TWD and the I-K calculated heat flux methods, the corresponding TC values are approximately 139 and 106 W/mK for the smaller sample and 843 and 620 W/mK for the bigger sample. This means that the TWD method overestimates the TC values by around 31% and 36% for the smaller and the bigger samples, respectively, with respect to the I-K procedure based accurate method. It might be hypothesized that even bigger system would lead to even greater overestimation and that is why we believe that when Park et al. [47], calculate the TC of SLG close to 3200 W/mK using the TWD method, the correct TC value should be actually much smaller. We also obtained $\frac{1}{2A}\left(\bar{\bar{\mathcal{E}}}_L - \bar{\bar{\mathcal{E}}}_R\right) = 1.31$ and 29.03 eV/(Å²ps), for the smaller and the bigger samples, respectively. Using Eq. (4.13), we also calculate the correction term $\langle q \rangle_c = 0.891 \times 10^{-3}$ and 3.416×10^{-3} eV/(Å²ps) for the two sizes.

4.2.3 SED

The primitive superunit cells for all three systems, SLG, AB-BLG and $21.78°$ tBLG, are chosen as shown in Fig. 4.1. These unit cells are repeated N_1 and N_2 times along the vectors $\boldsymbol{p}_1$ and $\boldsymbol{p}_2$, respectively, as described in Section 4.1 to construct a sample. In order to obtain the position and velocity vectors of atoms in time for the SED analysis, first an energy minimization is done with periodic boundary conditions along all axes. This is followed by an equilibrium MD simulation with multiple MD runs where MD time step was taken as $\Delta t_{\mathrm{MD}} = 0.5$ fs. The first run involves a simulation under NPT condition with zero pressure and 300 K temperature for 2×10^5 MD steps. The second run is done under NVT condition with $\theta = 300$ K for 2×10^5 MD steps. These runs are performed with a Nose-Hoover chain thermostat. This is followed by another 2^{20} MD time steps under NVE condition to ensure that steady-state conditions are achieved without any corrupting influence of thermostats. The atomic positions and velocities are collected every 2^5 time steps. Ten different simulations are performed with different initial velocities to create replicas of ensemble so that an average of SEDs from these replicas are finally considered for the extraction of the phonon properties.

Only the allowed wavevectors are used in Eq. (4.15), which for crystalline struc-
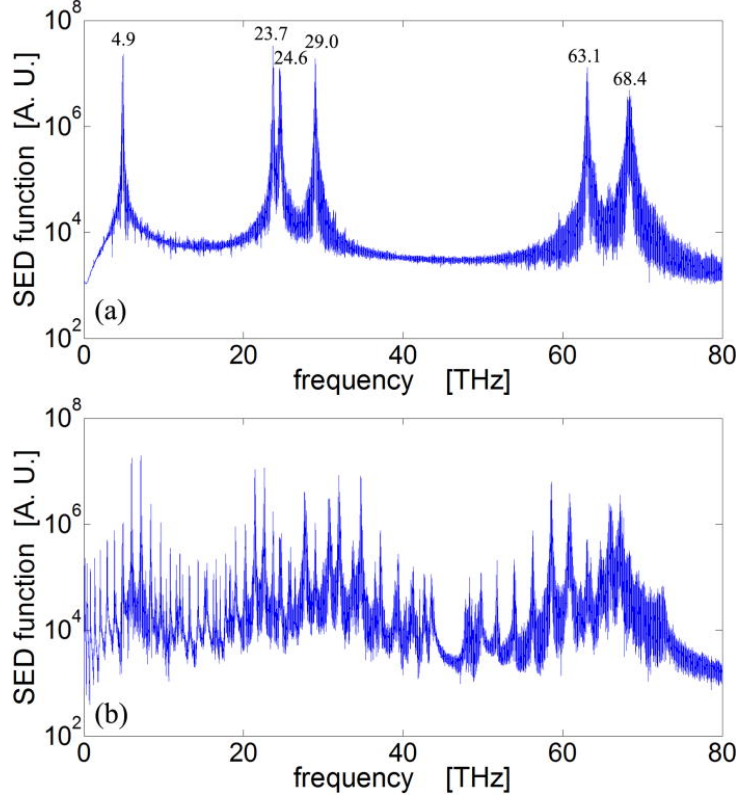
Figure 4.6: The calculated spectral energy density function with the appropriate wavevector $q = 2\pi/(3\sqrt{(3)}a)$ along the Γ-K direction (a), which is the integral multiple of the minimum wavevector and the inappropriate wavevector (b) where a is lattice constant [151].

tures are defined by

$$\boldsymbol{\kappa} = \sum_i \boldsymbol{b}_i \frac{n_i}{N_i}, \tag{4.15}$$

where the index i corresponds to i^{th} superunit cell vector ($i = 1, 2$ for $\boldsymbol{p}_1$ and $\boldsymbol{p}_2$, respectively, for our systems), N_i's are integers representing the number of unit cells along $\boldsymbol{p}_i$ vectors, and n_i's are also integers such that $-N_i/2 < n_i \leq N_i/2$ [83]. The vectors $\boldsymbol{b}_i$'s represent reciprocal lattice vectors, which are used to construct hexagonal BZs for all three systems studied as shown in Fig. 4.7a. The selection of wavevector is important as it is found that an inappropriate wavevector will result into wrong resonant peak and phonon properties [151] as shown in Fig. 4.6. We also follow Qiu and Ruan [51, 52] to exploit both the symmetry of the BZ and the simplicity in discretization of the BZ, and choose the allowed wavevectors in the first quadrant of hexagonal BZs, which have

50

their symmetric copies in other quadrants. We calculate the SEDs for all these symmetric copies for a chosen wavevector in the 1st quadrant, average them over and then also average over ten MD simulation runs with different initial velocities before fitting the SED curves in order to obtain the phonon properties.

We first study $N_1 \times N_2$ primitive unit cell samples, where $N_1 = N_2 = 20, 20, 8,$ respectively, of SLG, AB-BLG and $21.78°$ tBLG systems, for which the respective number of atoms per unit cell are 2, 4 and 28. With the help of the harmonic lattice dynamics based GULP package, we obtain the SLG, AB-BLG and $21.78°$ tBLG phonon dispersion curves along the symmetric Γ–M direction as shown in Figs. 4.7b–4.7d. They match with those obtained by Lindsay and Broido [40] for the SLG and Singh et al. [153] for both SLG and AB-BLG samples. They are also in close agreement with the curves obtained by Zou et al. [53] and Nika et al. [154] for the SLG system and Chenyang Li et al. [63] for the AB-BLG and tBLG samples, although both of these works follow the MD based Green's function method at 300 K temperature for the calculation of the dispersion curves. Following Cocemasov et al. [152], we also show the existence of ZA_2, TA_2 and LA_2 dispersion branches for the AB-BLG and $21.78°$ tBLG samples in Figs. 4.7c– 4.7d, whose respective frequencies are very close to ZA_1, TA_1 and LA_1 modes near the Γ-point. In order to have a sense of the contributions of basic phonon modes towards the TC, we classify the phonon modes into one of the basic modes (BMs) according to the *energy method* [2][1], which sorts the BMs according to the energies of the phonons around the Γ-point. There are total 6, 12 and 84 BMs in our SLG, AB-BLG and $21.78°$ tBLG systems. Further, SLG has 3 (ZA, TA and LA) whereas AB-BLG and tBLG systems have 6 (ZA_1, TA_1, LA_1, ZA_2, TA_2 and LA_2) acoustic BMs while the remaining BMs are optical modes. [2]

Having obtained satisfactory results for the dispersion curves, we calculate SEDs in Eq. (3.11) and fit the data over the Lorentzian function in Eq. (3.12). The curve fitting

---

[1]Although Cheng et al. [2] recommend using their new method, named as the projection method, in which the wavevectors are aligned and then projected onto the eigenvectors of the BMs to determine the weights of the BMs on the given phonon, we note in Fig. 3 of their work that both the energy method and the projection method almost give similar results for the contributions of the BMs to the scattering of electrons in 2D antimony.

[2]Actually, LA_2, TA_2 and ZA_2 are optical modes but following Cocemasov et al. [152], we term them as acoustic modes.

(a) Brilllouin zones

(b) SLG
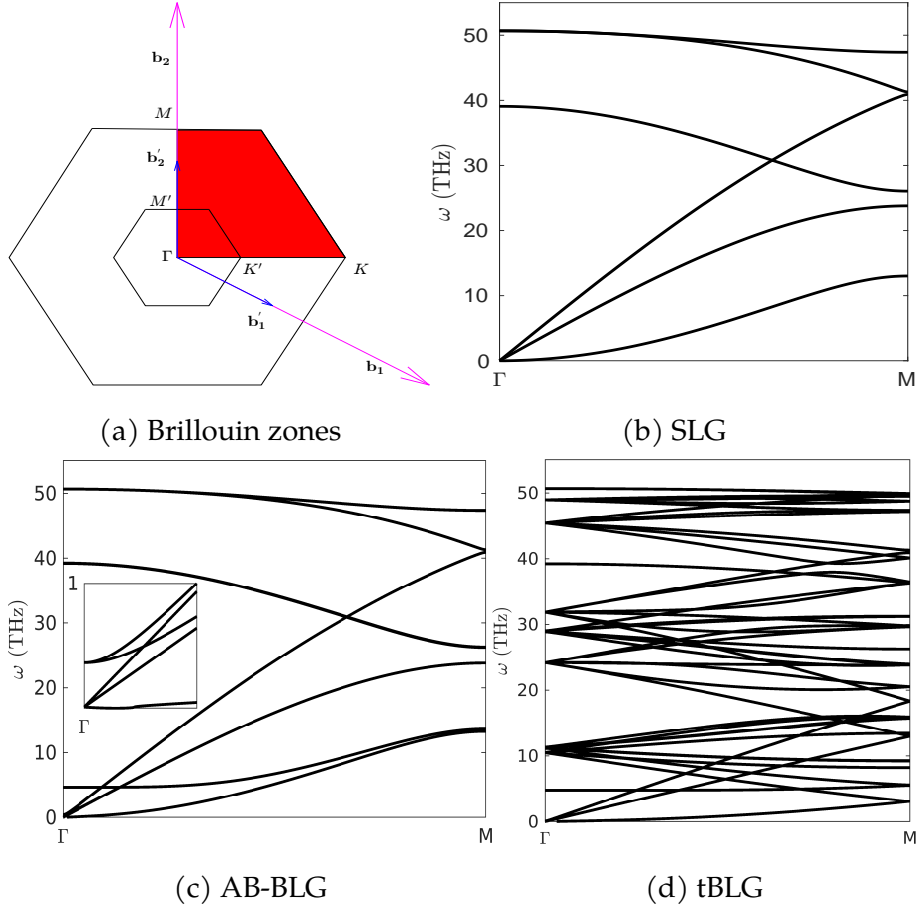
(c) AB-BLG

(d) tBLG

Figure 4.7: (a) Hexagonal Brillouin zones of SLG, AB-BLG and tBLG. The outer (bigger) BZ with reciprocal lattice vectors b_1 and b_2 corresponds to both SLG and AB-BLG primitive whereas the inner (smaller) BZ with reciprocal lattice vectors b'_1 and b'_2 corresponds to the tBLG samples. The red region is the 1st quadrant part of the BZ which is considered for the discrete allowed wave vectors. Phonon dispersion curves along Γ–M direction of (b) SLG, (c) AB-BLG, and (d) $21.78°$ tBLG samples. The inset figure in Fig. 4.7c shows the $ZA_1, TA_1, LA_1, ZA_2, TA_2$ and LA_2 dispersion branches in increasing order of the frequency for the modes near the Γ-point. These branches with modes having very close frequencies around the Γ-point are also observed in tBLG samples [152].
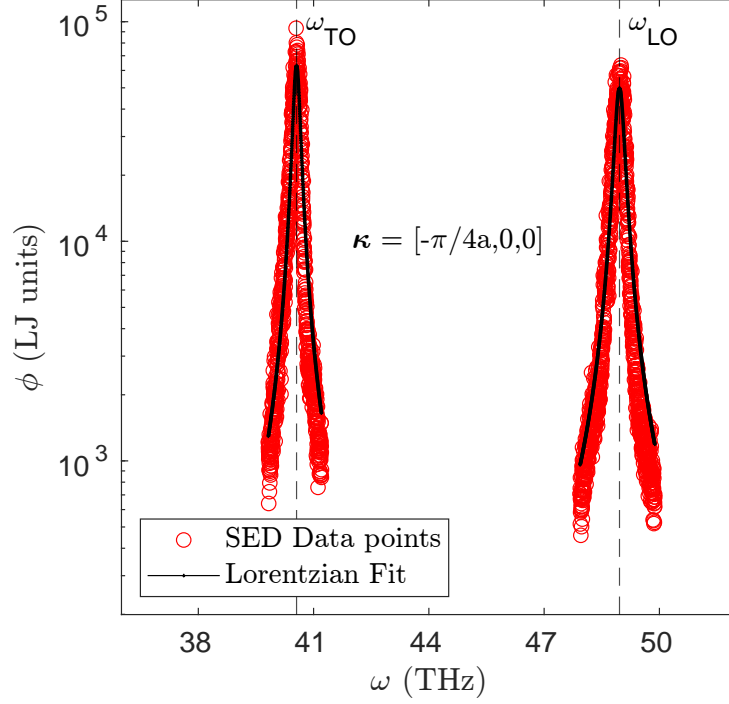
Figure 4.8: The Lorentzian function fits for the SED data for the SLG sample having 20×20 primitive unit cells. The two dispersion branches TO and LO for the wavevector $\boldsymbol{\kappa} = [-\pi/4a, 0, 0]$ are being shown for illustrative purposes.

is highly non-linear and done in a semi-automated way such that the fitting parameters are tuned by visualizing each fit for a given length and width of the system. Once these parameters are set, they can be used to fit the SED curves of the other samples with different lengths and widths. Figure 4.8 shows the Lorentzian fits for the phonon modes with wavevector $\boldsymbol{\kappa} = [-\pi/4a, 0, 0]$ and dispersion branches LO and TO as illustrative examples in the SLG sample with 20×20 primitive unit cells. The other phonon modes show similar fits. As suggested by Eq. (3.12) and following the discussion in Section 3.2, the fitting provides the anharmonic frequency $\omega_0\binom{\boldsymbol{\kappa}}{\nu}$ and the phonon lifetime $\tau\binom{\boldsymbol{\kappa}}{\nu}$ for the phonon mode $\binom{\boldsymbol{\kappa}}{\nu}$. The $\omega_0\binom{\boldsymbol{\kappa}}{\nu}$ thus obtained matches closely with the harmonic lattice dynamics based calculation of the frequency for a given wavevector $\boldsymbol{\kappa}$. This is confirmed by Fig. 4.9 which compares these two frequencies around the Γ-point in three graphene systems studied above. This shows that the harmonic normal modes are good approximations of the true vibrational modes of the system at 300 K.

The group velocities of these normal modes in the first quadrant of the BZs have been shown in Fig. 4.10. The average group velocities are 8.39, 8.27 and 6.43 km/s for

(a) SLG
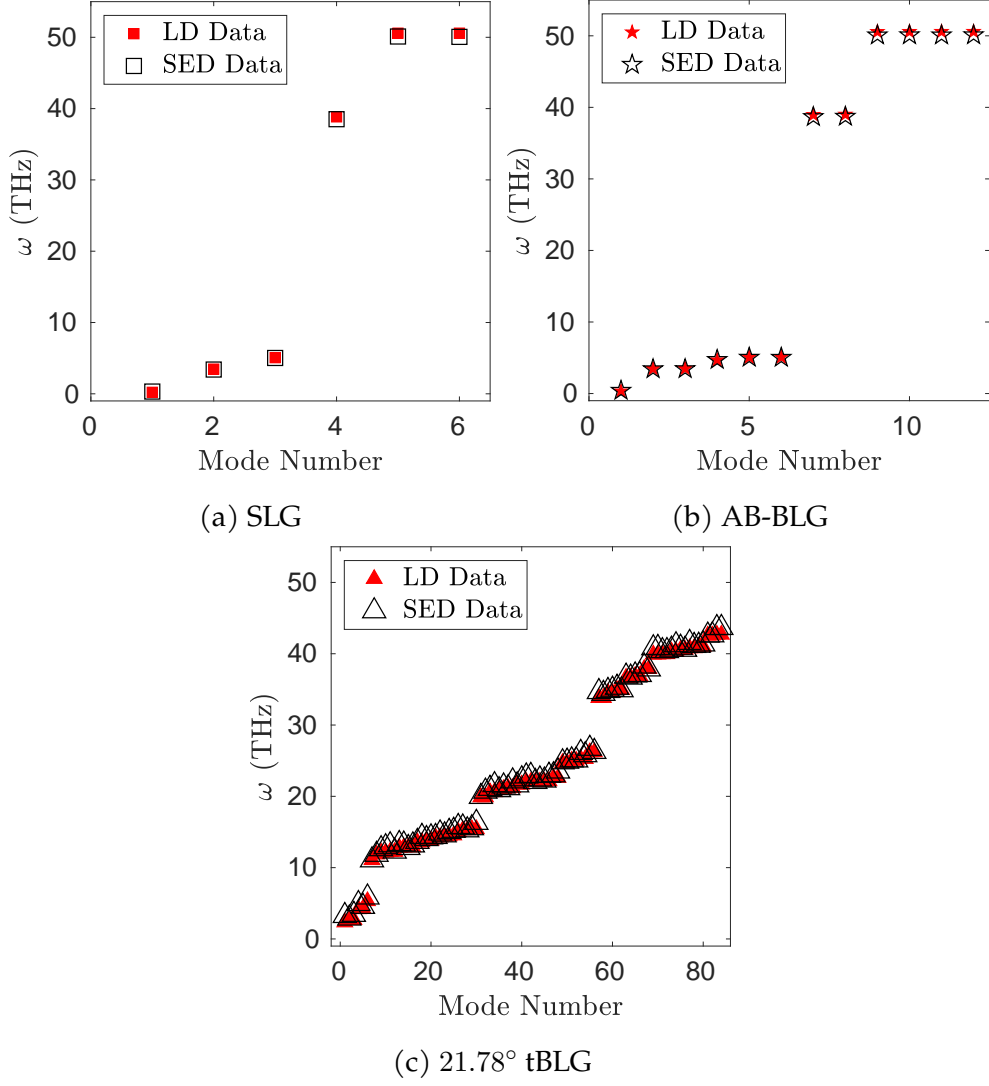
(b) AB-BLG

(c) 21.78° tBLG

Figure 4.9: Comparison between the harmonic lattice dynamics frequencies (LD Data) and the SED method fitted anharmonic frequencies (SED Data) around the Γ-point for all the available modes in the SLG, AB-BLG and $21.78°$ tBLG samples studied above with $N_1 \times N_2$ primitive unit cells, where $N_1 = N_2 = 20, 20, 8$, respectively, for three systems.

(a) SLG
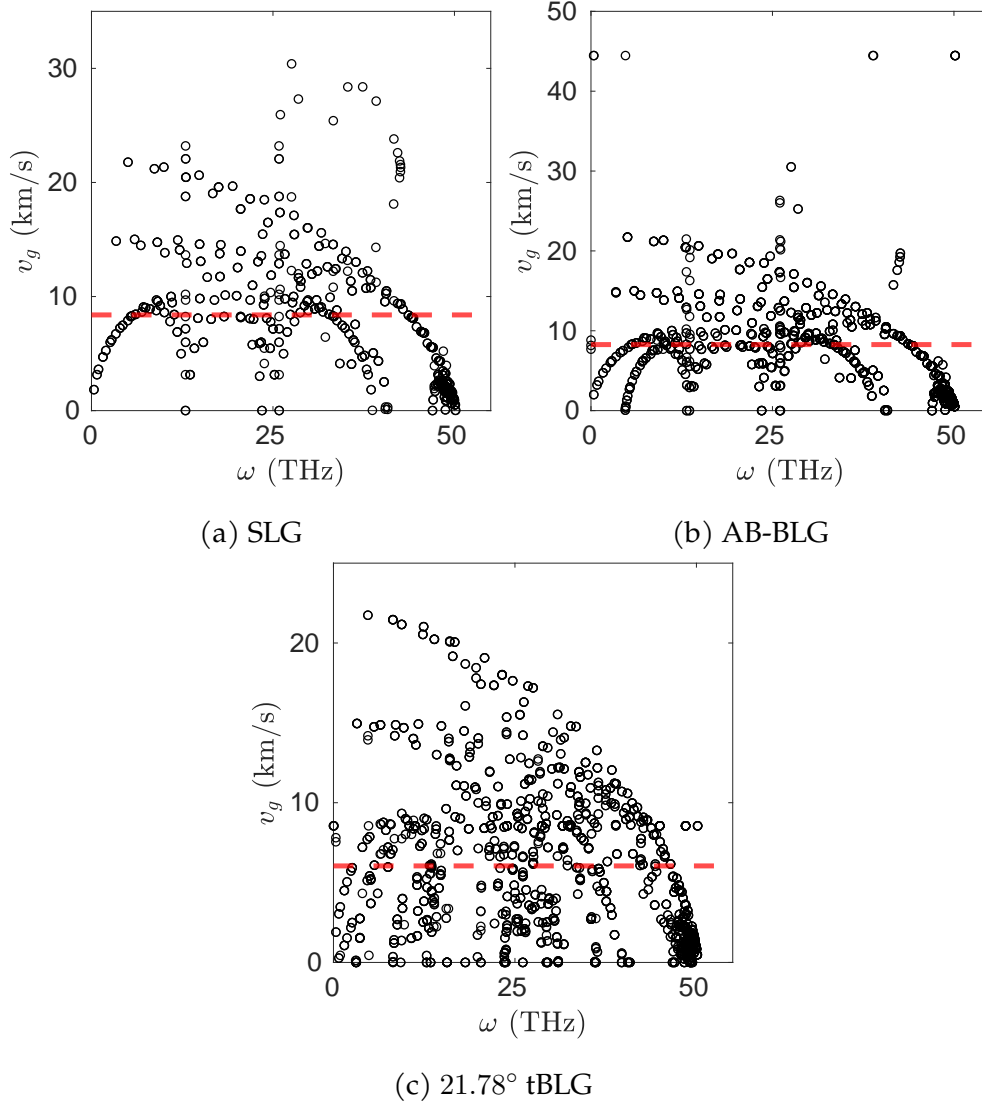
(b) AB-BLG

(c) 21.78° tBLG

Figure 4.10: Group velocities in km/s of the normal modes with the allowable wavevectors in the 1st quadrant of the BZs for (a) SLG, (b) AB-BLG and (c) 21.78° tBLG samples, which are prepared with $N_1 \times N_2$ primitive unit cells, where $N_1 = N_2 = 20, 20, 8$, respectively, for three systems. The dashed horizontal lines are showing the average values.

the SLG, AB-BLG and tBLG systems, respectively, also shown in Fig. 4.10 with dashed red horizontal lines. The first two have also same values but they are around 30% higher when compared with tBLG system. The significant difference in the values of the two bilayer systems is contrary to the result of Li et al. [63]. We also find an increase in the number of modes with null group velocity in the tBLG sample, which is another reason for its lower TC.

The phonon lifetimes obtained for the allowable wavevectors in the first quadrant of the BZs have been shown in Fig. 4.11. Each point in Figs. 4.11a–4.11c corresponds

(a) SLG
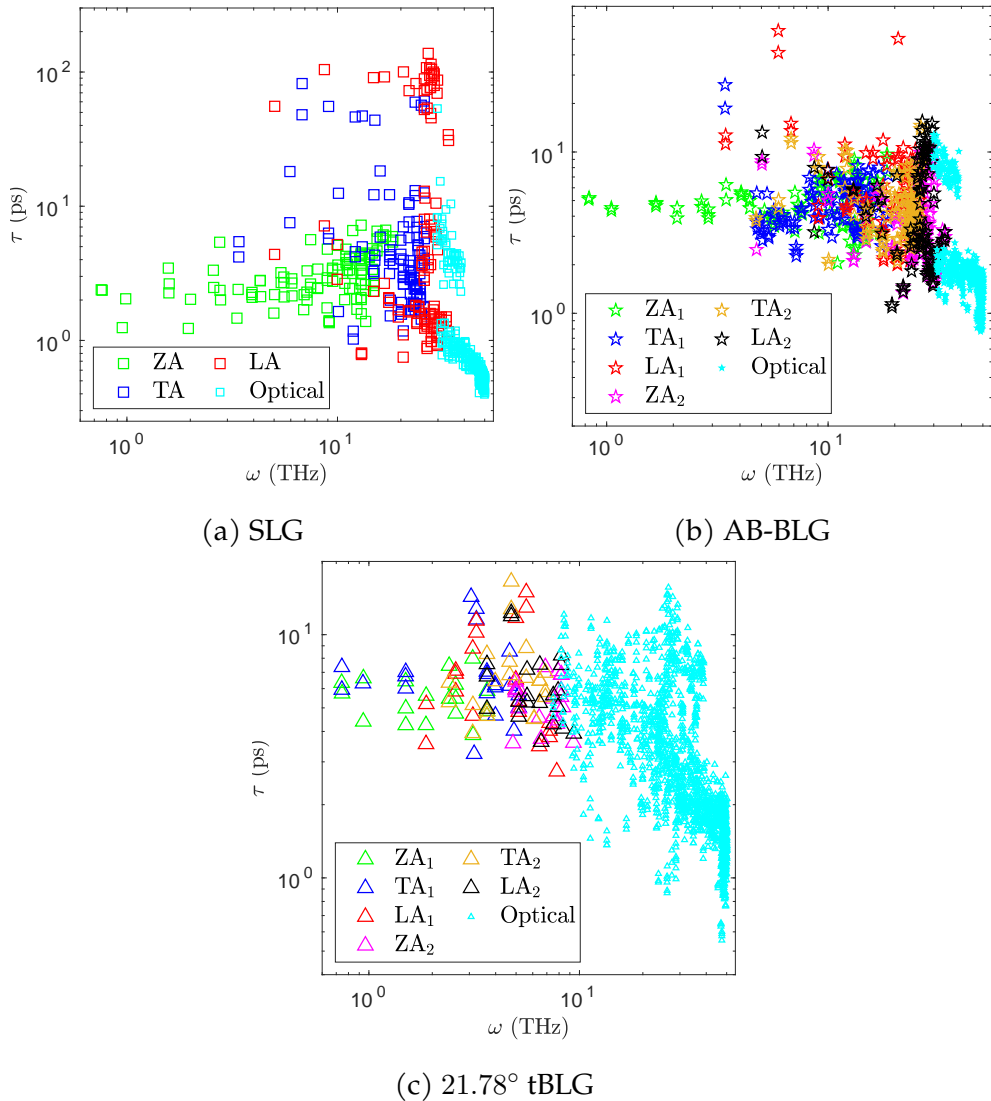
(b) AB-BLG

(c) 21.78° tBLG

Figure 4.11: Phonon lifetimes in ps obtained for the allowable wavevectors in the 1st quadrant of the BZ for (a) SLG, (b) AB-BLG and (c) 21.78° tBLG samples studied above.

to a $\binom{\kappa}{\nu}$ phonon mode. The maximum τ for the SLG, AB-BLG and tBLG samples are

close to 100, 65, 18 ps, respectively, and the average τ values are 6.9, 3.9 and 3.8 ps. The latter two have similar values and are almost 43% lower than the value for the SLG system. It can be observed that several optical modes have lowest values of τ for each system. For the SLG and AB-BLG samples, the highest τ's are available to TA and LA modes, whereas for the tBLG sample, the highest τ's are distributed among all modes. We further discuss the trends in these lifetimes across different BMs below.

With the help of the group velocity and the lifetime of each phonon mode, we calculate the TC, k, using Eq. (3.8), where k is equal to the average of the diagonal components of the TC tensor $\boldsymbol{k}$ in two-dimensional wavevector space. When the summation in Eq. (3.8) is done over all the allowable phonon modes only in the first quadrant of the BZs, we obtain $k = 325.97,\ 134.64$ and 101.45 W/mK for the SLG, AB-BLG and tBLG samples, respectively. This means the 1st quadrant TCs of the same size AB-BLG and tBLG samples are approximately 41% and 31% of the SLG sample, respectively. With the symmetry arguments, we then estimate the total TCs for the full BZs, which give total $k = 999.69, 458.63$ and 322.09 W/mK for three respective samples. This decrease in the TC across three samples can be explained with the help of Fig. 4.12a, where we show the BM specific contribution towards the TC of the sample in the first quadrant of BZs along high-symmetry Γ–K, Γ–M and M–K directions as well as non-symmetric (*nsym*) direction available to the remaining modes not lying on either of the aforementioned high-symmetry directions.

But, first we discuss the contributions of different BMs towards the TC within a given sample for the phonon modes in the first quadrant of BZs. In the SLG sample, the ZA, TA and LA modes have k in the increasing order along all symmetric and non-symmetric directions. For example, ZA, TA and LA modes have k close to $4, 16$ and 68 W/mK along the Γ–K, then 1, 36 and 58 W/mK along the Γ–M and 16, 38 and 77 W/mK along the *nsym* direction. The optical modes values are almost negligible for all directions. This trend, however, is not true for AB-BLG or tBLG sample. For the AB-BLG sample, ZA_1, TA_1 and LA_1 modes have close to 3, 2 and 13 W/mK TC along the Γ–K, then 1, 6 and 8 W/mK along the Γ–M and 11, 8 and 10 W/mK along the *nsym* direction. The ZA_2, TA_2 and LA_2 modes values are between 4 and 11 W/mK without any noticeable trend. Only the *nsym* optical modes in AB-BLG have comparable contribu-
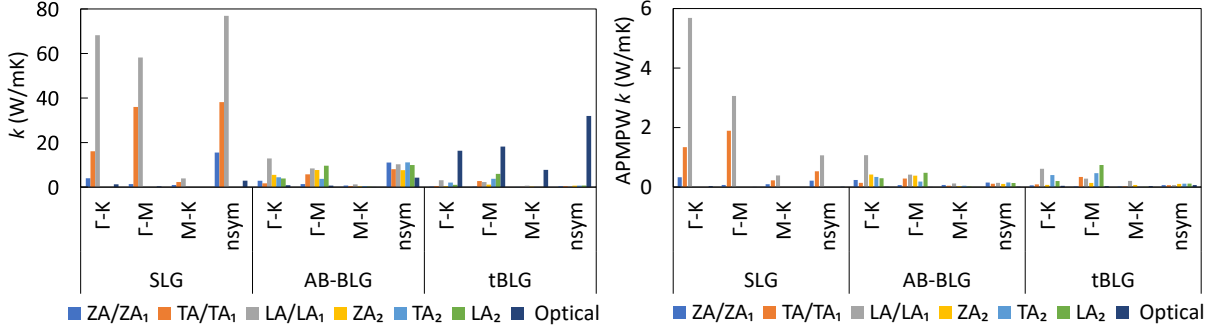
(a) k (W/mK) of 1st Quadrant

(b) Average per mode per wavevector k (W/mK)
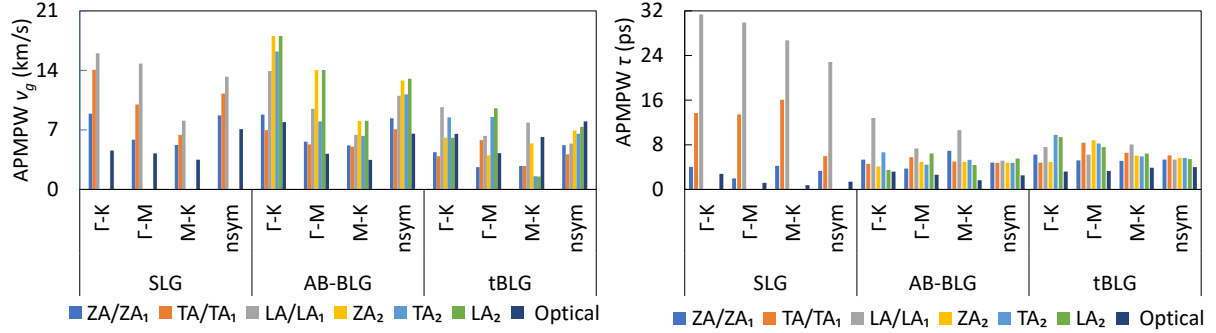
(c) Average per mode per wavevector v_g (km/s)

(d) Average per mode per wavevector τ (ps)

Figure 4.12: (a) Basic modes contribution to the overall TC, k (W/mK), along the high-symmetry Γ–K, Γ–M and M–K directions and the non-symmetric (*nsym*) direction, where the phonon modes in only the first quadrant of BZs are considered. The average per mode per wavevector (APMPW) contribution to (a) TC k (W/mK), (b) group velocity v_g (km/s), and (c) phonon lifetime τ (ps).

tion, close to 4 W/mK. For the tBLG sample, the values of the optical modes dominate with close to 16, 18, 8 and 32 W/mK along Γ–K, Γ–M, M–K and *nsym* directions. Only other significant contributions come from LA_1 and TA_2 modes along the Γ–K with close to 3 and 2 W/mK, and TA_1, LA_1, TA_2 and LA_2 along the Γ–M with close to 3, 2, 4 and 6 W/mK, respectively. Other modes have contributions below 1 W/mK. In sum, the LA and the TA modes contribute the most in SLG, all the acoustic modes and the *nsym* optical modes have almost similar contributions in AB-BLG and the optical modes dominate in tBLG samples. This domination of optical modes in tBLG samples is due to the fact that more number of optical modes are involved as the zone-folding of BZ occurs in tBLG which reduces the overall k contribution coming from the acoustic modes but simultaneously increases the contribution from the optical modes. Another effect of the zone-folding is an increase in the Umklapp scattering, which is also reflected in the lower mean free path of phonons [155]. With the help of Eq. (4.3), we have also been able to show in Section 4.2.1 that tBLG samples have the lowest mean free path of phonons in an average sense. Across the samples, it can be reasoned that the SLG has more TC than the other two samples because of the high contributions coming from the LA and the TA modes.Another interesting result which this study has been able to show is to quantitatively report the contributions coming from the high-symmetric directional modes as compared to the non-symmetric modes. For SLG, AB-BLG and tBLG samples, the high-symmetry modes contribute close to 60%, 55% and 65% towards the TCs.

However, this analysis alone does not provide the correct picture of the comparison of the contribution of different BMs across different systems because the number of allowable wavevectors varies for each BM across three systems. Hence, we define average per mode per wavevector (APMPW)[3] contribution to the TC k, the APMPW group velocity v_g (magnitude of the group velocity vector) and the APMPW phonon lifetime τ along the symmetric or the non-symmetric direction in the first quadrant of BZ as the total value of the property (k, v_g or τ) corresponding to the specific BM divided by the number of allowable wavevectors along the specified direction in the first quadrant. This helps us compare these properties for all the BMs across the symmetric and non-symmetric directions. For example, it can be observed in Fig. 4.12a for all three

---

[3]Note that this is average per basic mode per wavevector.

samples that the *nsym* acoustic and optical modes, together in the combined sense, seem to be contributing k on par with the high-symmetry direction modes, however, when compared in the APMPW sense, the high-symmetry direction modes are the highest contributors, as seen in Fig. 4.12b. In an approximate sense, the APMPW k is largely the result of the APMPW v_g and the APMPW τ (see Eq. (3.8)) and therefore we also discuss some trends in them.

As can be seen in Fig. 4.12c, the APMPW v_g's of LA and TA modes in SLG are more than ZA and optical modes in all directions. In AB-BLG, however, $ZA_{1,2}$ also have comparable values in comparison to $LA_{1,2}$ and $TA_{1,2}$ modes. The optical modes for AB-BLG still have the lowest APMPW v_g's in all directions, which is not the case for tBLG samples. In tBLG samples almost all modes have values between 2 km/s to 10 km/s without any noticeable trend. For the lifetimes, the APMPW τ's of LA and TA modes in SLG are more than those of corresponding $LA_{1,2}$ and $TA_{1,2}$ modes in AB-BLG or tBLG samples in all directions. The APMPW τ of LA modes (31.37 ps) in Γ–K direction of SLG is the highest across all the samples and across all high-symmetry and *nsym* directions. The ZA and optical modes in SLG have comparable APMPW τ's with respect to $ZA_{1,2}$ and optical modes of AB-BLG or tBLG samples.

An interesting result in our study is that the TCs obtained through the SED method for graphene systems are also size-dependent. We perform a size-dependent analysis by altering the number of primitive unit cells N_1 and N_2 ($N_1 = N_2 = N_0$) taken along the primitive lattice vectors $\boldsymbol{p}_1$ and $\boldsymbol{p}_2$ for our three systems. The results are shown in Fig. 4.13. Following [156], we perform a linear fit between k and $1/N_0$, and then extrapolate the linear curve to get the y-intercept so that the bulk TC (k_∞) can be obtained. In Table 4.1, we show a comparison between the bulk TCs obtained with both the NEMD direct method and the SED method for all three graphene systems.

This shows that the two methods give similar results for the bulk TCs for the SLG and $21.78°$ tBLG samples, only 15% higher TCs with the SED method when compared to the NEMD method. However, in case of AB-BLG sample, the SED method has almost 45% higher TC.

Although our TC values are on the lower side with respect to earlier studies, some of which are mentioned in Section 1.1, the bulk TCs at 300 K for the SLG are in some
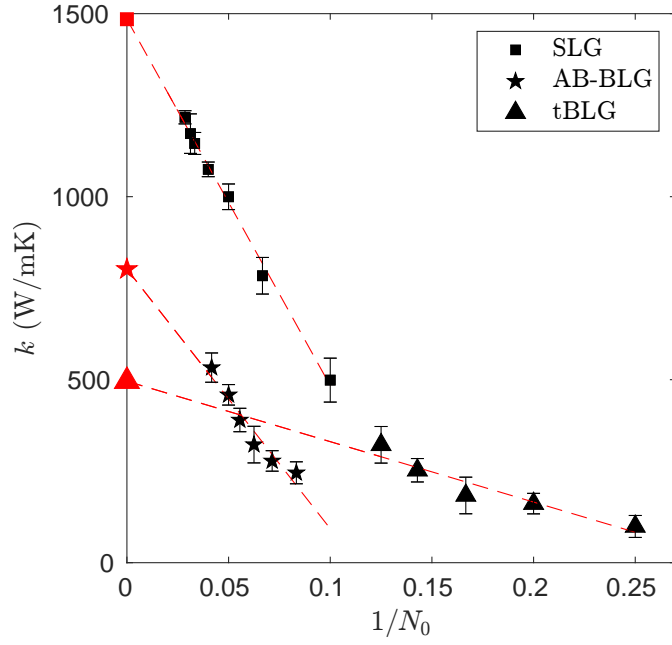
Figure 4.13: Size dependency of the TCs of the SLG, AB-BLG and $21.78°$ tBLG samples where the TCs are calculated with the SED method. The dashed red lines are showing the extrapolation to obtain the bulk TC.

Sample	k_∞^{NEMD} (W/mK)	k_∞^{SED} (W/mK)
SLG	1287.2	1484.5
AB-BLG	582.8	845.4
$21.78°$ tBLG	389.7	449.2

Table 4.1: Comparison of the estimated bulk thermal conductivity (k_∞) values using the NEMD direct method and the SED method.

agreement with experimental results of Cai et al. [39], SED results of Qiu and Ruan [52] and three and four-phonon scattering based results of Feng and Ruan [157]. Similarly, for the AB-BLG and tBLG samples, our results somewhat match with experimental results of Pettes et al. [56] for whom the misorientation angle was close to $11.7°$, and then with NEMD results of Wei et al. [61] who calculated the bulk TCs for AA-stacked SLG and BLG samples. The bulk TCs of bilayer samples provided by Liu et al. [67] are in close agreement with our results whereas the NEMD values of Li et al. [63] are comparable with our SED values for AB-BLG and $21.78°$ tBLG samples. Moreover, if we are interested in reproducing higher TCs obtained by some experiments, going as high as 5300 W/mK [38] for graphene, our calculation of lower TCs suggests that we need better interatomic potentials for intralayer C-C interactions than the currently widely used optimized tersoff potential [40], which has been shown to already provide maximum TCs for SLG but after inclusion of four-phonon scattering, the TC value significantly reduces to near 810 W/mK [157] at room temperature.

4.3 Summary

The size-dependent TC values of the SLG, AB-BLG and tBLG are first obtained using the NEMD direct method where the heat flux has been calculated consistently using Irving-Kirkwood's definition. A critique of the TWD method has also been presented which has been used as a measure of the heat flux in different studies. We show that this method greatly overestimates the TC and should not be used. The extrapolated bulk TCs obtained with the direct method are then compared with those obtained by the SED method, which has also been shown as a size-dependent method for all three graphene systems. The values obtained by the two methods have been found to be in close agreement with each other, at least for the SLG and the tBLG systems. We adopt the LD theory based SED Φ approach unlike other approaches which use the alternative phonon SED Φ' approach. The latter leads to more scattering in the relaxation time calculation and is not a reliable approach. For the AB-BLG and $21.78°$ tBLG systems, our calculation of the phonon lifetimes with the SED based approach is consistent unlike other approaches which use MD for the dispersion curves but DFT based packages for

the calculation of the lifetimes. We also study the contributions of basic phonon modes towards the TC of the samples in the first quadrant of BZs along high-symmetry as well as non-symmetric directions. We find that the ZA, TA and LA modes have TC contribution in the increasing order along all directions for the SLG, which is not true for bilayer samples. The optical modes dominate in tBLG sample and all the acoustic modes and the non-symmetric optical modes have almost similar contributions in AB-BLG sample towards TC contribution. We also find that the high-symmetry modes contribute the most for all three systems. We also conclude that SLG and AB-BLG have similar average group velocities (8.4 and 8.3 km/s) but 30% higher than tBLG's average group velocity (6.4 km/s), and AB-BLG and tBLG have similar average lifetimes (3.9 and 3.8 ps) but 43% lower than SLG's average lifetime (6.9 ps), which suggests that the bulk TC ($k \propto v_g^2 \tau$) of the AB-BLG and tBLG samples should be around 55% and 28% of the SLG sample. It is quite interesting that bulk TCs reported in Table 4.1 from the SED method show that indeed the values for the AB-BLG and tBLG samples are approximately 57% and 30% of the bulk TC of the SLG.

This page was intentionally left blank.

Chapter 5

Lattice Thermal Conductivity and Phonon Properties of Polycrystalline Graphene

In this chapter, we investigate the thermal transport in polycrystalline graphene samples with polycrystallinity only along x-axis (xPC-G samples) with the help of the robust and consistent normal mode decomposition (NMD) analysis based SED method [81, 156]. These samples cannot be categorized under BC-G samples or randomly oriented PC-G samples in the references cited above. First, almost similar size samples with seven different symmetric misorientation angles and stable dislocation cores are prepared and then the phonon properties and the TC tensor components, k_{xx} and k_{yy}, are calculated for each sample. A pristine graphene sample of the same size is also studied for comparison. This is followed by a size-dependent analysis of thermal transport for pristine graphene and xPC-G samples with two different misorientation angles, $21.78°$ and $32.2°$, so that bulk TCs of graphene with GBs of different misorientations can be compared. Contrary to other works on PC-G samples cited above, our work establishes strong dependence of the TCs of xPC-G samples on misorientation

angles.

The structure of the study is as follows. Section 5.1 describes the sample preparation method for xPC-G samples with different misorientation angles. In Section 5.2, we perform MD simulations necessary for the SED analysis. We discuss the results in Section 5.3 after calculating the phonon group velocities with the help of the harmonic lattice dynamics based GULP package and phonon lifetimes by fitting the SED curves to the Lorentzian function. In this section, we also obtain bulk TCs of three graphene systems with the SED method. Finally, we conclude in Section 5.4 with a summary and suggestions for any future work.

5.1   Sample Preparation

We follow the centroidal Voronoi tessellation based algorithm proposed by Ophus et al. [158] to generate symmetric GBs in graphene. We prepare xPC-G samples with seven different misorientation angles, where each misorientation angle $\theta = \theta_L + \theta_R$ can be defined through translation vectors (n_L, m_L) and (n_R, m_R) corresponding to the left and the right domains along the GB, respectively[159]. For symmetric GBs, we have $n_L = n_R = n$, $m_L = m_R = m$, $\theta_L = \theta_R = \frac{\pi}{3} - \arctan\frac{(2n+m)}{\sqrt{3}}$ and n and m are integers [159, 158]. The corresponding periodic length along the GB direction is $L_y = a\sqrt{3(n^2 + nm + m^2)}$, where the average C-C bond length $a = 1.397$ Å. Following Yazyev and Louie [160], the simulation supercell for the SED method, involving two parallel equally spaced GBs, is rectangular of length L_x and width L_y in order to satisfy periodic boundary conditions (PBCs). This means the unit cell vectors, $\boldsymbol{V}_1 = L_x\hat{\mathbf{i}}$ and $\boldsymbol{V}_2 = L_y\hat{\mathbf{j}}$, of the supercell are orthogonal to each other, where $\hat{\mathbf{i}}$ and $\hat{\mathbf{j}}$ are unit vectors in the Cartesian plane. Although close to $L_x = 4$ nm is sufficient to maintain stable GB structures, as this significantly reduces the influence of elastic interactions due to neighbouring GBs [82, 160], we have taken $L_x = 6$ nm for all our samples. Thus, two neighbouring GBs are separated by 3 nm, which also becomes the grain size along x-axis. The superunit cells for $(n.m)$ xPC-G samples with different misorientation angles θ have been shown in Figs. 5.1b–5.1h. The primitive unit cell of the pristine graphene $(1, 1)$ sample is created by two planar lattice vectors $\boldsymbol{V}_1 = \sqrt{3}a\hat{\mathbf{i}}$ and

(a) SLG   (b) (3,4) 9.43°   (c) (2,3) 13.17°

(d) (1,2) 21.78°   (e) (2,5) 27.80°

(f) (1,3) 32.20°   (g) (1,5) 42.10°   (h) (1,6) 44.82°
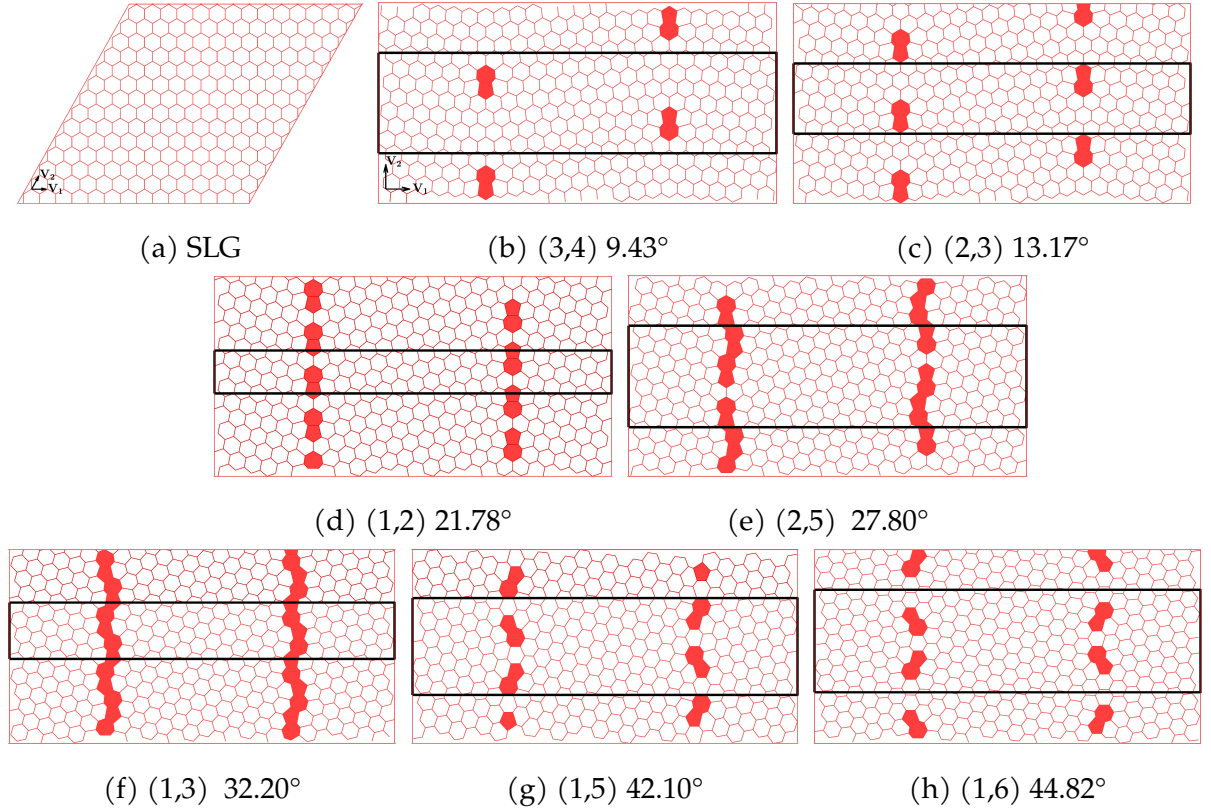
Figure 5.1: Close to $180 \times 32 \, \text{Å}^2$ size pristine graphene sample and xPC-G samples with seven different misorienation angles. The schematic diagram of the primitive unit cell vectors of the SLG sample is shown in (a) and rectangles created by black boundaries in (b)–(h) show the primitive superunit cells of commensurate unit cell for xPC-G samples.

$\boldsymbol{V}_2 = \sqrt{3}a(\cos 60°\hat{\mathbf{i}} + \sin 60°\hat{\mathbf{j}})$, as shown in Fig. 5.1a.

5.2 Computational Details

Now, we reiterate some basic principles of the SED method which has been explained in details in Abhikeern and Singh [81]. Based on the Fourier's law and the phonon Boltzmann transport equation (BTE) under relaxation time approximation, the TC tensor of a system is given by

$$\mathbf{k} = \sum_{\boldsymbol{\kappa}} \sum_{\nu} c_v(\substack{\boldsymbol{\kappa} \\ \nu}) \left(\mathbf{v}_g(\substack{\boldsymbol{\kappa} \\ \nu}) \otimes \mathbf{v}_g(\substack{\boldsymbol{\kappa} \\ \nu}) \right) \tau(\substack{\boldsymbol{\kappa} \\ \nu}) \tag{5.1}$$

Here, the summation is over all allowed normal modes in the first Brillouin zone (BZ), and each mode $(\substack{\boldsymbol{\kappa} \\ \nu})$ is denoted by wavevector $\boldsymbol{\kappa}$ and dispersion branch ν. Moreover, $c_v(\substack{\boldsymbol{\kappa} \\ \nu})$, $\mathbf{v}_g(\substack{\boldsymbol{\kappa} \\ \nu})$ and $\tau(\substack{\boldsymbol{\kappa} \\ \nu})$ are the mode specific volumetric specific heat, group velocity and phonon lifetime, respectively. We take $c_v(\substack{\boldsymbol{\kappa} \\ \nu}) = k_B/V$ [156] for all modes for classical MD simulations, where k_B is the Boltzmann's constant and V is the volume of the simulation box. The group velocity $\mathbf{v}_g(\substack{\boldsymbol{\kappa} \\ \nu}) = \frac{\partial \omega(\substack{\boldsymbol{\kappa} \\ \nu})}{\partial \boldsymbol{\kappa}}$ is obtained by using finite difference method over a fine grid of wavevectors around the given mode $(\substack{\boldsymbol{\kappa} \\ \nu})$. The GULP package [140] is used for calculating the normal mode frequencies $\omega(\substack{\boldsymbol{\kappa} \\ \nu})$ and eigenvectors. Based on the primitive unit cell of pristine $(1,1)$ graphene, and primitive superunit cells of $(1,2)$ and $(1,3)$ xPC-G with $21.78°$ and $32.20°$ misorientation angles, respectively, the phonon dispersion curves of these three configurations in the first BZ have been provided in Fig. 5.2. We provide the phonon dispersion curves in the first Brillouin zone (BZ) for the pristine graphene along $\Gamma - \mathrm{M}$ direction and xPC-G samples with $21.78°$ and $32.20°$ misorientation angles along $\Gamma - \mathrm{X}$ direction based on their respective primitive unit and superunit cells where similar to [161] we obtain some high frequency modes which are flat.

The phonon lifetime for a mode is calculated by fitting a Lorentzian function over the SED curve, which is determined by the normal mode decomposition method by projecting the equilibrium MD simulation based atomic positions and velocities onto the normal mode coordinates.

(a) SLG with 2 basis atoms
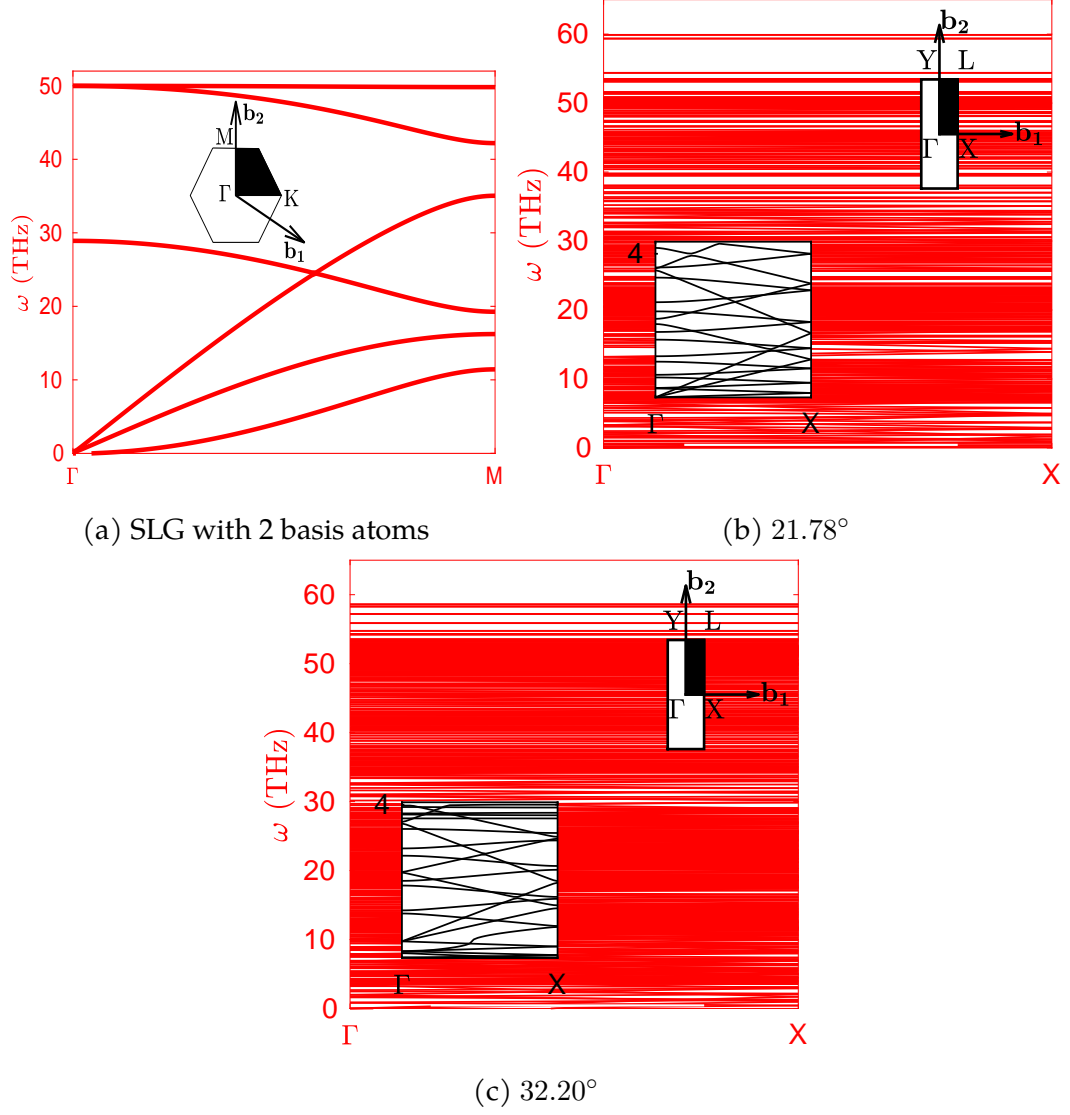
(b) 21.78°

(c) 32.20°

Figure 5.2: Dispersion curves in the first BZ for (a) SLG with 2 basis atoms along $\Gamma - M$ direction, (b) $21.78°$ xPC-G sample with 152 basis atoms and (c) $32.20°$ xPC-G sample with 204 basis atoms along $\Gamma - X$ direction. Insets in (b) and (c) show the zoomed area of the same dispersion curves with upper limit of frequency constrained to 4 THz. The insets show the respective BZ of SLG and xPC-G samples and the first quadrant chosen for the the discretization of BZ due to its symmetry.

We describe the simulation details below. The primitive superunit cell for (n, m) structure is repeated N_x and N_y times along x and y axes, respectively, to construct a sample of the required size. To ensure the lowest possible energy state for the GB, we first perform energy minimization over this structure with PBCs along all axes, where the C-C interactions are modeled by the original REBO potential [162]. The equilibrium MD simulation is then performed with multiple MD runs where MD time step was taken as $\Delta t_{MD} = 0.2$ fs. In the first run, atoms are simulated under NPT ensemble conditions with zero pressure and 300 K temperature for 2×10^5 MD steps. The next run is performed under NVT conditions with 300 K for 2×10^5 MD steps. The Nosé-Hoover chain thermostats are used for these NPT and NVT runs. The final run is performed for another 2^{16} MD time steps under NVE conditions to ensure steady-state conditions without any corrupting influence of thermostats. The package LAMMPS [149] is used for all MD simulations and energy minimization. We choose the wavevectors in the first quadrant (hexagonal BZ for SLG and rectangular BZ for xPC-G samples) to exploit both the symmetry of the BZ and the simplicity in discretization of the BZ [52, 81] as shown in the insets of Fig. 5.2. The SEDs are first calculated for a chosen wavevector κ and dispersion branch ν in the first quadrant and for all its symmetric copies in other quadrants of the first BZ, and then they are averaged over for a single MD simulation. Then, we perform five different MD simulations with different initial atomic velocities so that a final average of SEDs for all simulations can be considered for the extraction of the phonon lifetime for a given mode.

5.3 Results

Using the primitive superunit cells defined above, we prepare same-size pristine graphene and seven xPC-G samples with different θ corresponding to (n, m) translation vectors. In order to achieve an approximate size of 180×32 Å^2, the number of unit cells required along x and y axes, N_x and N_y, respectively, for different (n, m) samples has been listed in Table 5.1.

The table also mentions the unit cell length L_y along y-axis and the number of atoms per unit cell for each sample. For all our samples, we obtain excellent Lorentzian

Table 5.1: Number of unit cells required along x and y axes, N_x and N_y, respectively, to obtain 180×32 Å^2 size samples with different misorientation angles θ.

θ	(n, m)	L_y (Å)	Unit cell atoms	(N_x, N_y)
0	(1,1)	2.10	2	(73,14)
9.43	(3,4)	14.71	344	(3,2)
13.17	(2,3)	10.55	248	(3,3)
21.78	(1,2)	6.40	152	(3,5)
27.80	(2,5)	15.11	356	(3,2)
32.20	(1,3)	8.72	204	(3,4)
42.10	(1,5)	13.47	320	(3,2)
44.82	(1,6)	15.86	372	(3,2)

fits for the SED curves.

We particularly show the Lorentzian curve fitting over the SED data for $21.78°$ and $32.20°$ xPC-G samples for a chosen wavevector $\boldsymbol{\kappa} = [\pi/6a, 0, 0]$ and one of the optical dispersion branches in Fig. 5.3. The fitting provides not only the phonon lifetime τ but also the anharmonic frequency ω_0 as the center of the Lorentzian fit over the SED curve. These anharmonic frequencies match closely with the harmonic lattice dynamics based frequencies. For illustration, we provide excellent match for all available modes for a given wavevector $\boldsymbol{\kappa}$ around the "X" point as shown in Figs. 5.3c and Figs. 5.3d for $21.78°$ and $32.20°$ angles, respectively. Hence, it is established that the harmonic frequencies are a good approximation for the vibrational modes at the room temperature.

The fitting provides not only the phonon lifetime τ but also the anharmonic frequency ω_0, matching with the GULP based normal frequency ω, as the center of the Lorentzian fit over the SED curve. The phonon lifetimes (τ), group velocities $v_g = \left(\sqrt{v_{g_x}^2 + v_{g_y}^2} \right)$ and mean free paths along x and y axes, $l_x = v_{g_x}\tau$ and $l_y = v_{g_y}\tau$, obtained for the allowable modes in the first quadrant of the first BZs of pristine graphene and two xPC-G samples with $\theta = 21.78°$ and $32.20°$ have been shown in Fig. 5.4. With a total of 1533, 1710 and 1836 modes for these three systems, respectively, it makes more sense to talk about root mean square (rms) of group velocities $v_{g_{rms}}$, average of phonon lifetimes $\langle \tau \rangle$ and average of mean free paths, $\langle l_x \rangle$ and $\langle l_y \rangle$, rather than individual acous-
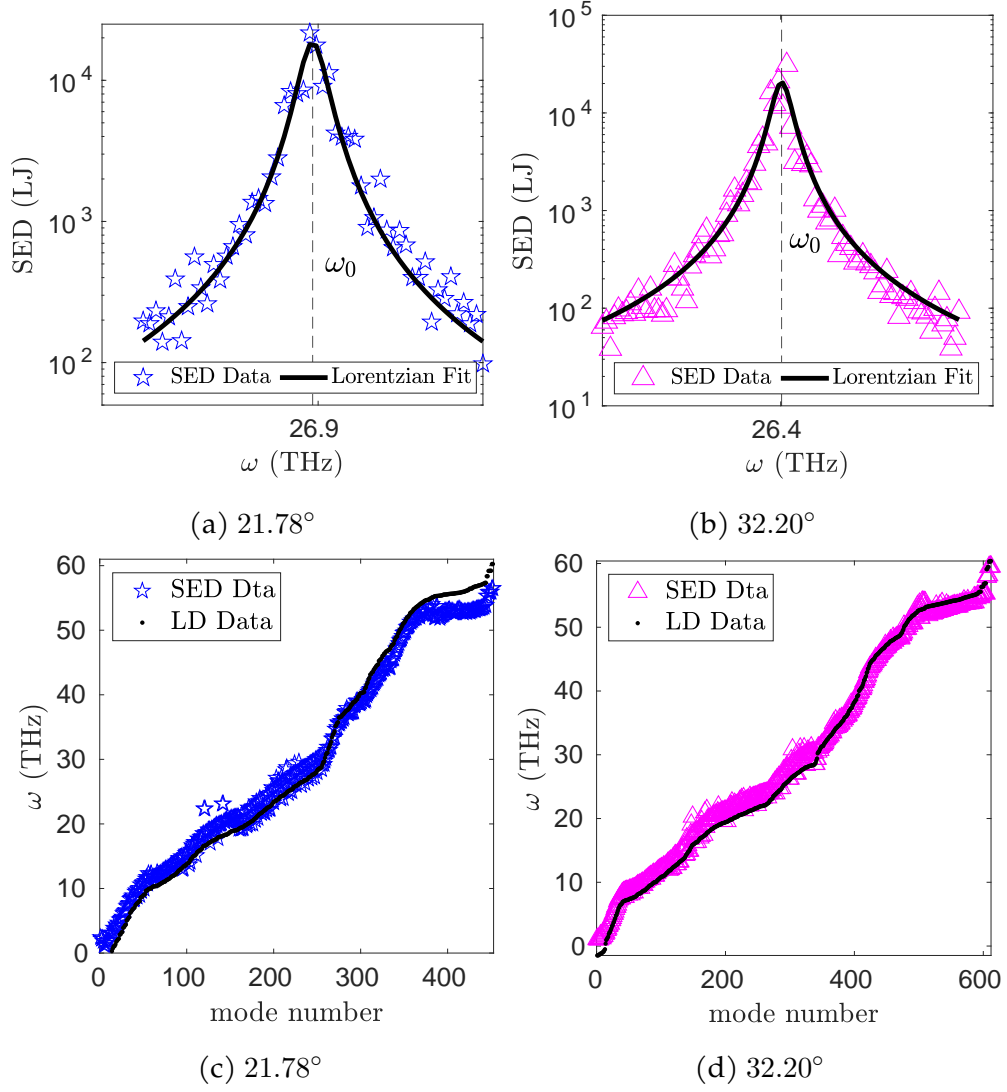
Figure 5.3: The Lorentzian fit for the SED data obtained at wavevector $\boldsymbol{\kappa} = [\pi/6a, 0, 0]$ and an optical dispersion branch for (a) 21.78° and (b) 32.20° xPC-G samples. Comparison between the GULP generated harmonic lattice dynamics frequencies (LD Data) ω and the Lorentzian curve fitted anharmonic frequencies ω_0 for all available modes at X symmetric point with wavevector $\boldsymbol{\kappa} = [\pi/a, 0, 0]$.
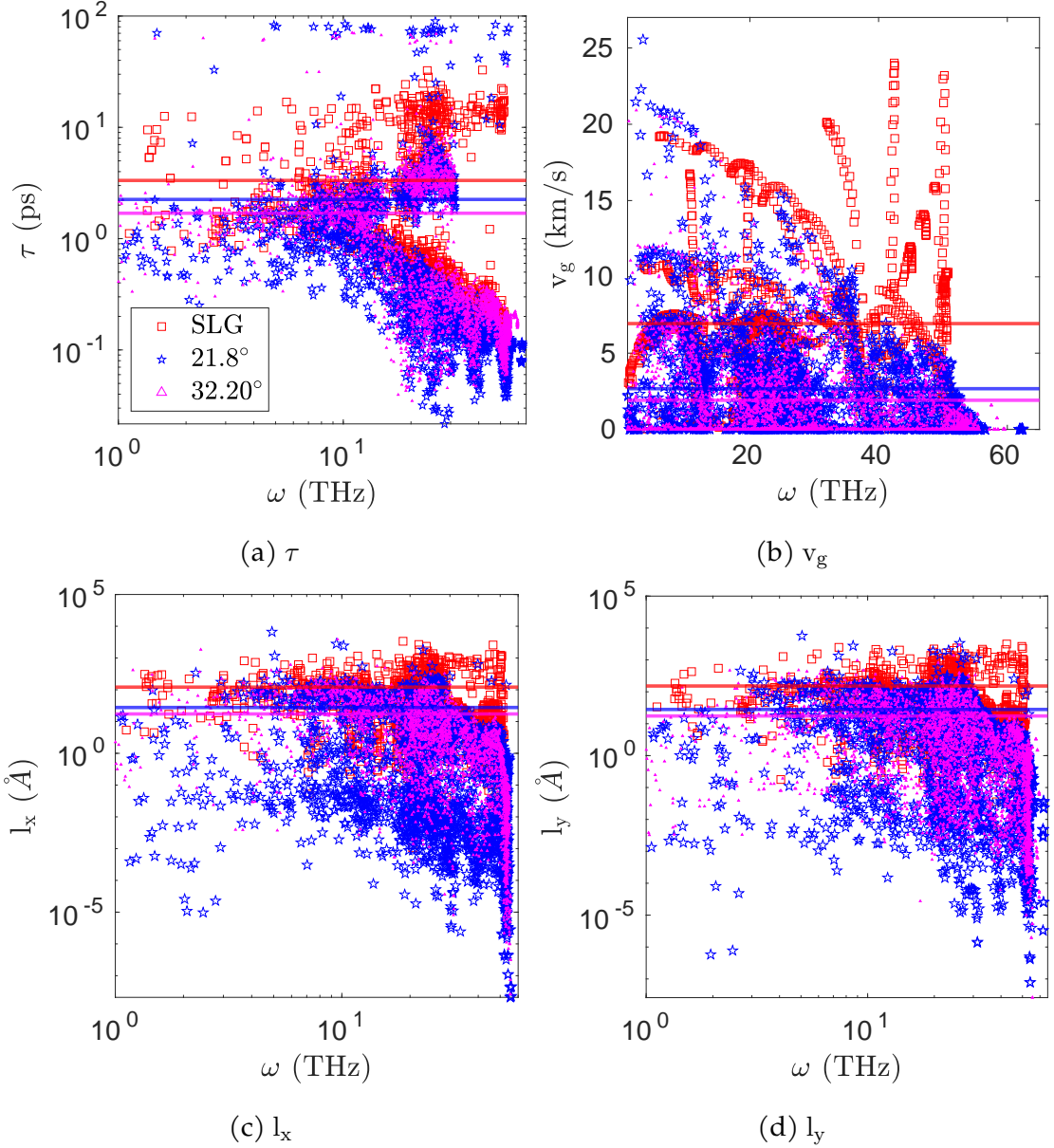
Figure 5.4: (a) Phonon lifetimes in ps, (b) group velocities in km/s, and mean free paths (c) l_x and (d) l_y of the allowable normal modes in the the first quadrant of the BZs for pristine SLG (red) and xPC-G with $\theta = 21.78°$ (blue) and $\theta = 32.20°$ (magenta) samples, which are prepared with $N_x \times N_y$ primitive unit cells, where $N_x = 73, 3, 3$ and $N_y = 14, 5, 4$, respectively, for three systems. The solid horizontal lines show the average values.

tic or optical modes, where the average is taken over all available modes in the first quadrant of the first BZ. We obtain $\langle\tau\rangle = 3.33, 2.25, 1.69$ ps, $v_{g_{rms}} = 6.93, 2.67, 1.91$ km/s, $\langle l_x \rangle = 121.1, 27.7, 17.3$ Å and $\langle l_y \rangle = 152.1, 28.0, 17.5$ Å, respectively, for three systems shown in Fig. 5.5 with solid horizontal lines. Later, we also show x and y components of $v_{g_{rms}}$ in Fig. 5.5b and $\langle\tau\rangle$ in Fig. 5.5c for all angles. We note that average mean free paths are less than the grain size along x-axis (30 Å) for xPC-G samples. We also observe that around 90% of the phonon modes have their mean free paths less than 30 Å along both x and y axes for all seven different misorientation angles. This was expected for l_x since phonons would scatter at the GBs, however, l_y also showing similar trend is an interesting result.

Having obtained all phonon properties, we use Eq. (5.1) to obtain the TC tensor components $k_{xx} \approx 87, 29, 28, 88, 35, 56, 25, 14$ W/mK and $k_{yy} \approx 80, 7, 27, 80, 5, 54, 9, 3$ W/mK for pristine graphene and seven different misorientation angles listed in Table 5.1 in increasing order. With respect to the pristine graphene, maximum reduction in the TCs is found in the last sample with $44.82°$ angle, almost 84% and 96% reduction for k_{xx} and k_{yy}, respectively. As reflected in the values and also shown in Fig. 5.5a, the TCs strongly depend upon the misorientation angles. We also note that except for samples with $13.17°$ and $32.2°$ tilt angles, there exists strong anisotropy along x and y axes in the TCs for other angles. Also, the TCs for $21.78°$ sample is the highest among all xPC-G samples. These trends in TCs can be explained in terms of the trends in the group velocities and the phonon lifetimes, which were found to be uncorrelated for all xPC-G samples. Since $k_{xx} = \sum_{\boldsymbol{\kappa},\nu} c_v\binom{\boldsymbol{\kappa}}{\nu} v_{g_x}^2\binom{\boldsymbol{\kappa}}{\nu} \tau\binom{\boldsymbol{\kappa}}{\nu}$, and we have taken $c_v\binom{\boldsymbol{\kappa}}{\nu} = k_B/V = c_v$ for all modes, hence, the average of k_{xx} over all n modes in the first BZ can be written as $\langle k_{xx} \rangle = n c_v \langle v_{g_x}^2 \rangle \langle\tau\rangle = n c_v v_{g_{x_{rms}}}^2 \langle\tau\rangle$, provided that correlation coefficient ρ of $v_{g_x}^2$ and τ for all modes is close to zero. The similar argument holds for $\langle k_{yy} \rangle$. The averages of TCs defined in this way are denoted as $\langle k_{xx} \rangle_I$ and $\langle k_{yy} \rangle_I$. We calculate $\rho(v_{g_x}^2, \tau)$ and $\rho(v_{g_y}^2, \tau)$ and plot them for all angles in Fig. 5.5d. All correlation coefficients were found to be in the range of $0.2\% - 1.9\%$, i.e. they are close to zero. This suggests that group velocities and phonon lifetimes are uncorrelated for all xPC-G samples. We obtain $\langle k_{xx} \rangle_I \approx 27, 24, 86, 28, 50, 21, 12$ W/mK and $\langle k_{yy} \rangle_I \approx 7, 25, 123, 5, 45, 6, 3$ W/mK for seven different angles in the increasing order. They are also plotted in Fig. 5.5e and we observe that values closely match with actual k_{xx} and k_{yy} reported earlier, except

(a) k_{xx} and k_{yy}

(b) $v_{g_{rms}}$ along x and y axes

(c) $\langle \tau \rangle$

(d) ρ

(e) k_I and k_{II} components
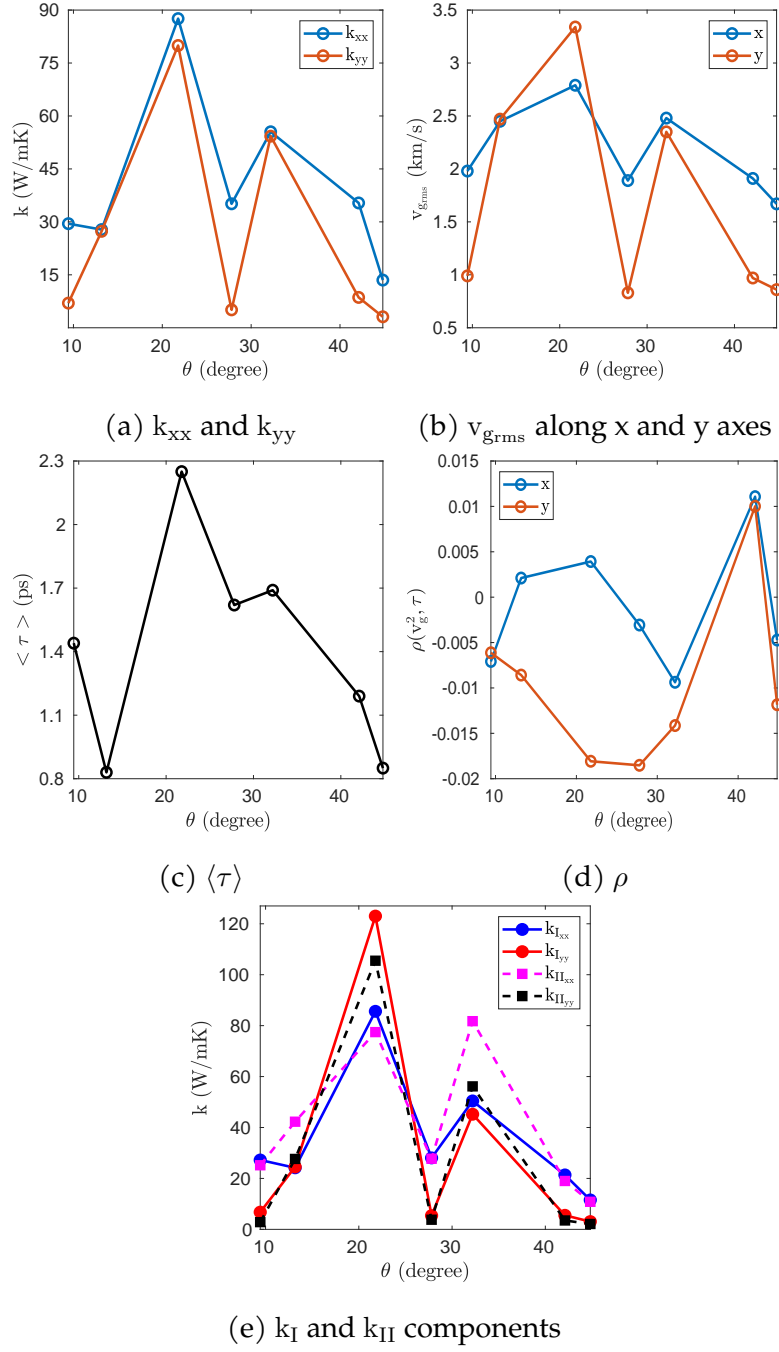
Figure 5.5: For all misorientation angles, (a) k_{xx} and k_{yy}, (b) x and y components of $v_{g_{rms}}$, (c) $\langle \tau \rangle$, (d) correlation coefficients $\rho(v_{g_x}^2, \tau)$ and $\rho(v_{g_y}^2, \tau)$, (e) $k_{I_{xx}}$ and $k_{I_{yy}}$ in solid lines and $k_{II_{xx}}$ and $k_{II_{yy}}$ in dashed lines.

for $21.78°$ sample for which $\langle k_{yy} \rangle_I = 123$ W/mK whereas $k_{yy} = 80$ W/mK, i.e. an increase of around 54% is found. This deviation can be attributed to $21.78°$ sample having a slightly higher $\rho(v_{g_y}^2, \tau)$ and the highest $v_{g_{yrms}}$. But in general, we can assert that $\langle k_{xx,yy} \rangle = \langle k_{xx,yy} \rangle_I \approx k_{xx,yy}$ and it can be emphasized that an average phonon mode can be defined whose group velocity components along x and y axes are the rms of group velocity components of all phonon modes and whose lifetime is the average of all phonon lifetimes. Therefore, anisotropy in the TC components is largely the outcome of anisotropy in the group velocities, since lifetimes remain the same for both xx and yy components of the TC. The maxima and minima of the TC components across all angles, however, have to explained both in terms of maxima and minima of x and y components of $\mathbf{v}_{g_{rms}}$ and also those of $\langle \tau \rangle$.

Next, we express group velocity and phonon lifetime as distribution functions of normal mode frequencies so that the TC components can also be written as distribution functions of frequencies. This can potentially help in the semi-analytical and numerical solutions of the BTE [163]. For that, we first show phonon density of states (DOS) in Fig. 5.6a, where $DOS(\omega)d\omega$ represents the number of modes lying between ω and $\omega + d\omega$. We observe that the DOS remains almost the same for all GB angles [75]. This is followed by calculating the sum of $\mathbf{v}_{g_{rms}}$ along x axis for all modes lying in the frequency range $[\omega, \omega+d\omega)$ and then dividing by the total number of modes in the same range, which we denote as $\overline{v_{g_{xrms}}}$. Similarly, we define $\overline{v_{g_{yrms}}}$ and $\overline{\tau}$ for $v_{g_{rms}}$ along y axis and τ, respectively. Basically, they are distribution functions of ω and can be treated as average properties of phonons in $[\omega, \omega + d\omega)$. For any given angle, we find that natural semi-log plots of $\overline{v_{g_{xrms}}}(\omega)$ and $\overline{v_{g_{yrms}}}(\omega)$ can be fitted with straight lines as shown in Figs. 5.6b and 5.6c, respectively, and the natural semi-log plot of $\overline{\tau}(\omega)$ can be fitted with a piecewise constant function in Fig. 5.6d. Therefore, we can write,

$$\overline{v_{g_{xrms}}}(\omega) = a_1 e^{-a_2\omega}, \quad \omega \in [0, \omega_{max}] \tag{5.2a}$$

$$\overline{v_{g_{yrms}}}(\omega) = b_1 e^{-b_2\omega}, \quad \omega \in [0, \omega_{max}] \tag{5.2b}$$

$$\overline{\tau}(\omega) = \begin{cases} c_1, & \omega \in [0, \omega_d] \\ c_2, & \omega \in (\omega_d, \omega_{max}] \end{cases} \tag{5.2c}$$
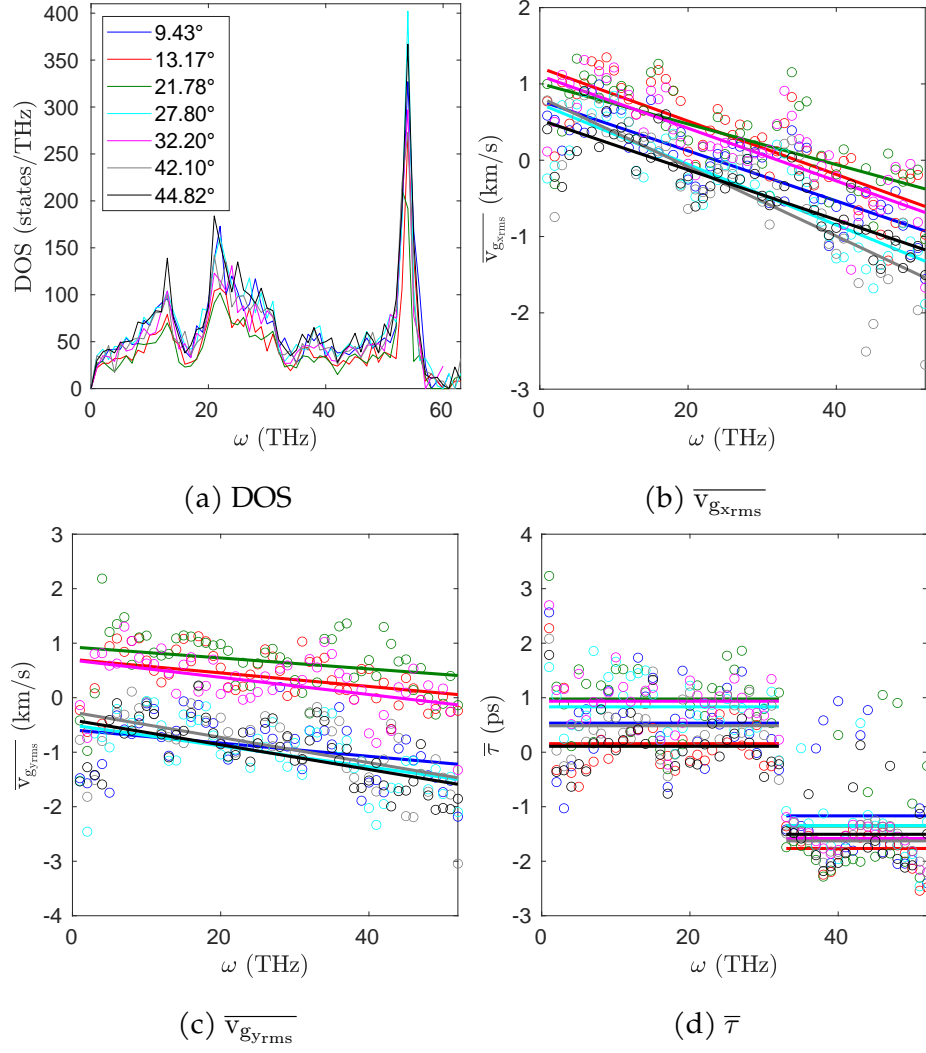
Figure 5.6: (a) DOS, (b) $\overline{v_{g_{x_{rms}}}}$, (c) $\overline{v_{g_{y_{rms}}}}$, (d) $\overline{\tau}$ for all xPC-G samples of size close to $180 \times 32 \, \text{Å}^2$.

where ω's are in THz, group velocity components are in km/s, lifetimes are in ps, $a_1, a_2, b_1, b_2, c_1, c_2$ are constants, $\omega_d < \omega_{\max}$ is the frequency at which discontinuity in $\overline{\tau}$ emerges and $\omega_{\max}$ is the maximum frequency beyond which the phonon properties can be assumed as zero. Interestingly, we find that $\omega_d = 32$ THz and $\omega_{\max} = 52$ THz are the same for all xPC-G samples. The values of the constants appearing in Eq. (5.2) for different misorientation angles are provided in Table 5.2.

Table 5.2: a_1, a_2, b_1, b_2, c_1, and c_2 for different GB angles.

θ	a_1	a_2	b_1	b_2	c_1	c_2
9.43	2.182	0.033	0.554	0.012	1.704	0.311
13.17	3.360	0.035	2.020	0.012	1.170	0.171
21.78	2.735	0.027	2.534	0.010	2.654	0.259
27.80	2.094	0.040	0.605	0.019	2.298	0.260
32.20	3.031	0.035	1.992	0.016	2.550	0.205
42.10	2.282	0.045	0.768	0.023	1.624	0.197
44.82	1.699	0.033	0.663	0.023	1.115	0.222

Based on this, we calculate another measure of the TC components as

$$\langle \mathrm{k_{xx,yy}} \rangle_{\mathrm{II}} = c_v \int_0^{\omega_{\max}} \mathrm{DOS}(\omega) \left(\overline{\mathrm{v_{g_{x,y_{\mathrm{rms}}}}}} \right)^2 \overline{\tau}(\omega) d\omega, \tag{5.3}$$

where $c_v = k_B/V$ as defined above. The values obtained for xPC-G samples with increasing angles are $\langle \mathrm{k_{xx}} \rangle_{\mathrm{II}} \approx 25, 42, 77, 28, 82, 19, 11$ W/mK and $\langle \mathrm{k_{yy}} \rangle_{\mathrm{II}} \approx 3, 28, 105, 4, 56, 4, 2$ W/mK. We find that $\langle \mathrm{k_{xx,yy}} \rangle_{\mathrm{II}}$ vary within $\pm 60\%$ range of the actual $k_{xx,yy}$ calculated by Eq. (5.1), and therefore, we can assert that $\langle \mathrm{k_{xx,yy}} \rangle_{\mathrm{II}} \approx \mathrm{k_{xx,yy}} \pm 0.6 \, \mathrm{k_{xx,yy}}$.

The TCs obtained through the SED method are size-dependent [81]. A size-dependent analysis is performed for xPC-G samples with $\theta = 21.78°$ and $32.20°$ by increasing the number of primitive superunit cells along y-axis, N_y, but keeping N_x same because we reason that the x-axis length, around 18 nm, is too large to significantly affect the TC components if we further increase N_x. In Ref. [81], we calculated the TC for SLG up to 50 Å length along x-axis, and the TC deviated from the bulk value by only 10%. We chose these two angles because they have the least number of basis atoms in comparison

to xPC-G samples with other misorientation angles, specifically, 152 for $21.78°$ and 204 for $32.20°$, which makes the computation more tractable. We take $N_y = 5, 6, 7, 8$ and 9 for $21.78°$ samples and $N_y = 4, 6, 7$ and 8 for $32.20°$ samples. The results for TC components k_{xx} and k_{yy} are shown in Fig. 5.7. Following Ref. [81], we perform a linear fit between
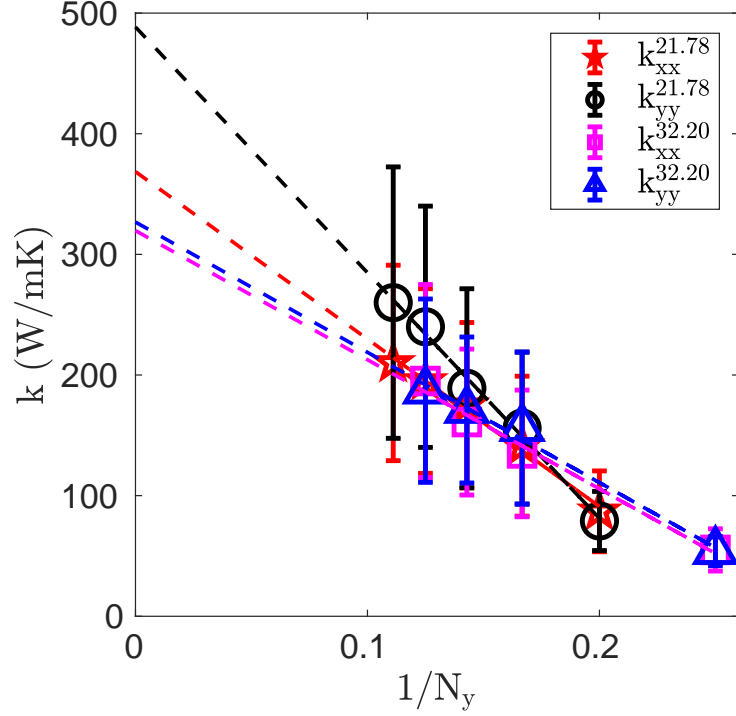
Figure 5.7: Size dependency of the TCs of the xPC-G samples with $\theta = 21.78°$ and $\theta = 32.20°$. The dashed lines are showing the extrapolation to y-axis to obtain the bulk TC.

$k_{xx,yy}$ and $1/N_y$ and then extrapolate the linear curve to obtain the bulk TC ($k_{xx,yy}^\infty$). We calculate $k_{xx}^\infty = 369$ and 320 W/mK, and $k_{yy}^\infty = 488$ and 327 W/mK for $\theta = 21.78°$ and $32.20°$, respectively. The bulk TC values for $32.20°$ match closely with Fox et al. [78] who calculated around 312 W/mK for $32.20°$ BC-G samples with the NEMD method. For the pristine graphene studied here, $k_{xx}^\infty = 563$ and $k_{yy}^\infty = 863$ W/mK. Therefore, k_{xx}^∞ decreased by 34% and 43% and k_{yy}^∞ decreased by 43% and 62%, respectively, for the two angles with respect to the pristine graphene. We also note that the $32.20°$ sample does not show much anisotropy in the bulk TC components whereas the $21.78°$ sample shows strong anisotropy.

5.4 Summary

In conclusion, we predict the phonon properties of xPC-G samples with seven different misorientation angles with the equilibrium MD simulations and the SED method. Our work concludes that the TCs of xPC-G samples strongly depend upon misorientation angles. We also find that the square of the group velocity components along x and y axes and the phonon lifetimes are uncorrelated for all samples, which allows for the calculation of TCs in terms of an average phonon mode whose group velocity components are the rms of group velocity components of all phonon modes and lifetime is the mean of all phonon lifetimes. We explain anisotropy in the TC components for some angles with the difference in the rms of group velocity components of all phonon modes along x and y axes. Further, the DOS for all xPC-G samples are found to be independent of the misorientation angles. Based on the DOS, distribution functions of phonon properties have been calculated and plotted as semi-log plots against the phonon normal frequencies. The distributions of group velocity components are found to be exponentially decaying whereas the distribution of phonon lifetime showed piecewise constant function behavior with respect to frequency. This is reflected in the distribution of TC components, which also show exponentially decaying behavior against frequency. We provide the parameters for the exponential and piecewise constant functions for the group velocity components and lifetimes, respectively. We provide another measure of the TC based on these functions and estimate that their values are within $\pm 60\%$ range of the actual TC values. Finally, we perform the size-dependent analysis for two angles, $21.78°$ and $32.20°$, and calculated their bulk TC components, which are found to have decreased by 34% to 62% in comparison to the bulk TC values of the pristine graphene. We end with a suggestion that the frequency dependent distribution functions suggested for the rms of group velocity components and the phonon lifetime can be used in multiscale semi-analytical and numerical solutions for the solutions of the BTE.

Chapter 6

Single Layer Graphene with Strain and Ripple

In the previous chapters, with structural changes such as stack of graphene layer with Moiré patters and grain boundaries in single layer graphene, we examined the thermal properties of these modifies structures. Building on that understanding, this chapter explores the influence of strain on SLG, specifically how mechanical deformation alters its thermal and mechanical properties. Investigating the strain effect is crucial as it focuses on graphene's properties for applications requiring high flexibility and durability, such as in flexible electronics and nano-mechanical systems.

The aim of this chapter is to investigate the thermal conductivity (TC) properties of single layer graphene, with a particular focus on understanding phonon behavior and energy transport in the presence of an externally applied strain. To achieve this, we utilize Spectral Energy Density (SED) analysis, which allows us to decompose the energy distribution of phonon modes across the frequency spectrum. By examining these modes in detail, SED analysis provides crucial insights into how phonons contribute to thermal transport by looking into the changes in their group velocities and

lifetimes in the presence of external strain also including the identification of dominant heat-carrying modes.

The structure of the study is as follows. Section 6.1 details the sample preparation process for single layer graphene with different strain. In Section 6.2, we conduct molecular dynamics (MD) simulations necessary for performing SED analysis. Section 6.3 discusses the results obtained, including phonon group velocities calculated via the harmonic lattice dynamics using the GULP package and phonon lifetimes derived by fitting the SED curves to Lorentzian functions. Additionally, in this section, we calculate the thermal conductivities (TCs) of the different strained single layer graphene systems using the SED method. Finally, Section 6.4 provides a summary of the findings and recommendations for future work.

6.1   Sample Preparation
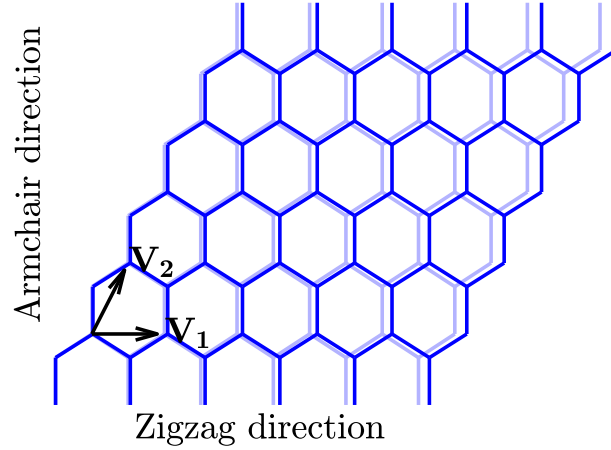
Figure 6.1: Comparison of unstrained (light blue) and 3% strained pristine graphene (dark blue). Strain is applied in the zigzag direction.

Fig. 6.1 shows the unstrained SLG in light blue color and strained SLG in dark blue color. First, we describe the construction of SLG samples. The two planar lattice vectors taken for the formation of the primitive unit cell of the SLG samples are $\boldsymbol{V}_1 = a(1+\epsilon_{\text{zig}})\hat{\mathbf{i}}$ and $\boldsymbol{V}_2 = a((1+\epsilon_{\text{zig}})\cos 60°\hat{\mathbf{i}} + \sin 60°\hat{\mathbf{j}})$ in Å, where $\hat{\mathbf{i}}$ and $\hat{\mathbf{j}}$ are unit vectors along x and y axes, respectively, as shown in Fig. 6.1. Also, lattice constant $a = 2.492$ Å and ϵ_{zig} is

the strain applied in the zigzag direction as per Eq. (6.1):

$$\epsilon_{\mathrm{x}} = \epsilon_{\mathrm{zig}} = \frac{V'_{1_x} - V_{1_x}}{V_{1_x}} \tag{6.1}$$
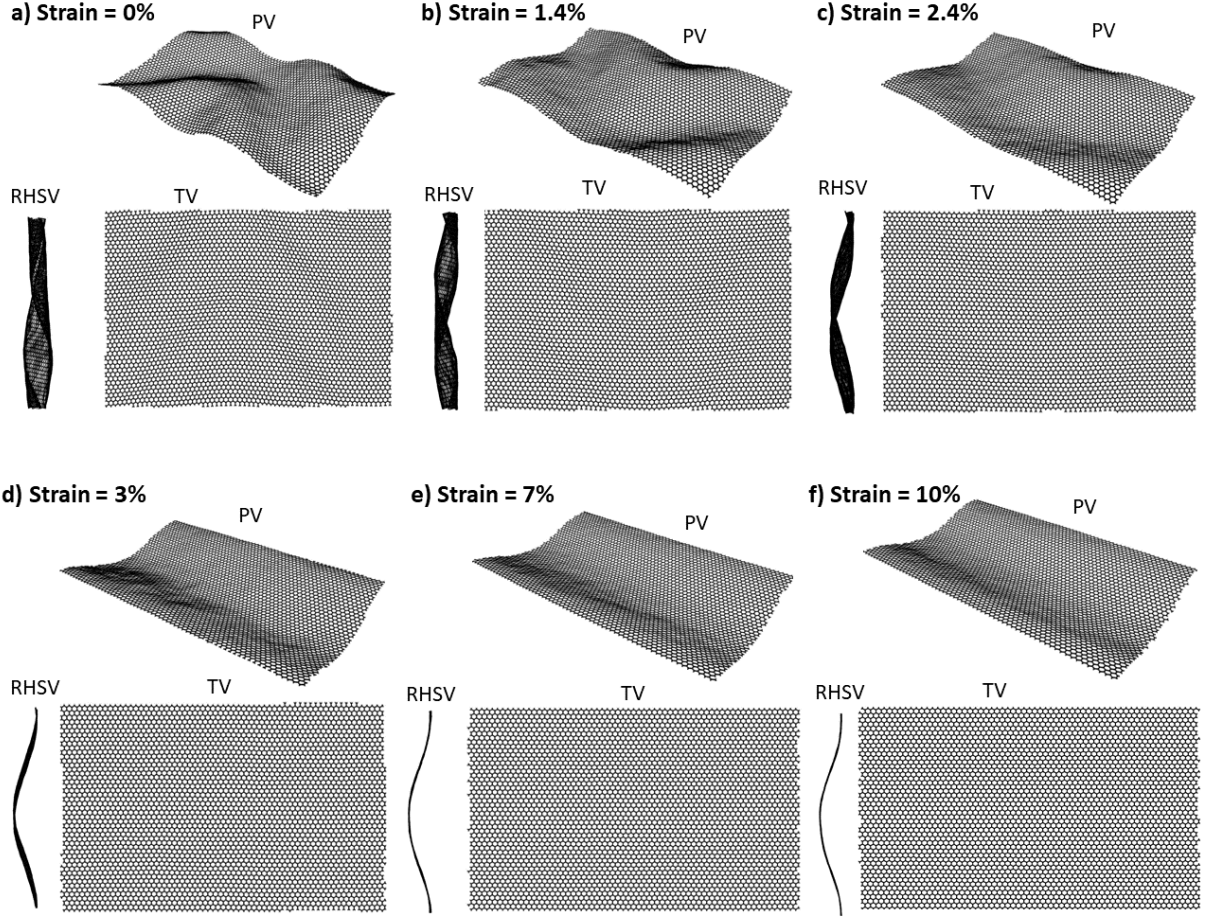
Figure 6.2: Structural changes in pristine graphene with the application of strain for a sample size of 150×100Å. It is observed that such a large sample length has a pronounced ripple effect at 0% strain, which keeps on decreasing as the strain increases [164].

For our NMD analysis, we chose $N_1 \times N_2$ primitive unit cell samples, where $N_1 = N_2 = 12$ which corresponds to a sample size of 31×26 Å. A small graphene sheet produces negligible ripples. We characterize the ripples in terms of their magnitude (ΔZ) which we quantify as the time average of the absolute difference between the maximum and the minimum out-of-plane (z) coordinates of the sample. For the SLG sample of size 31×26Å , we obtain $\Delta Z \sim 1$Å . But for a sample length of 150×100Å ,

the ripple effect is much stronger, which keeps on decreasing as we keep increasing the strain as shown in Fig. 6.2.

6.2 Computational Details

The computational details employed in this study are outlined below. As per Section 3.2, in order to obtain the position and velocity vectors of atoms over time for the SED analysis, we used Large-scale Atomic/Molecular Massively Parallel Simulator (LAMMPS) using optimized Tersoff potential. The initial energy minimization is performed under periodic boundary conditions along all axes. This is followed by an equilibrium MD simulation consisting of multiple MD runs with a time step of $\Delta t_{\mathrm{MD}} = 0.2$ fs. The first run is conducted under NVT conditions at a temperature of 300 K for 5×10^5 MD steps utilizing the Nose-Hoover chain thermostat. The second run is performed under NVE conditions for another 10^5 MD steps. Subsequently, an additional 2^{16} MD steps are carried out under NVE conditions to ensure that steady-state conditions are reached without the influence of thermostats. Atomic positions and velocities are recorded every 2^2 time steps. Five separate simulations with different initial velocities are conducted to create ensemble replicas, and the averaged SEDs from these replicas are used to extract the phonon properties.

Similar to Section 3.2, only the allowed wavevectors are used in Eq. (3.8), as applicable for crystalline structures [83]. The vectors $\boldsymbol{b}_i$ represent reciprocal lattice vectors, which are employed to construct irregular hexagonal Brillouin Zones (BZs) for all strained systems studied, as illustrated in Fig. 6.3. With the help of the harmonic lattice dynamics based GULP package, we obtain the phonon dispersion curves along the symmetric Γ–M direction as shown in Fig. 6.4. Using the GULP package we also obtain the phonon density of states (PDOS) and eigenvectors. Further, following the approach of Qiu and Ruan [51, 52], we leverage both the symmetry of the BZ and the ease of discretization to select allowed wavevectors within the first quadrant of the regular hexagonal BZ for unstrained system and irregular hexagonal BZs for all strained systems, which have symmetric counterparts in the other quadrants. SEDs are calculated for all allowed wavevectors corresponding to the first BZ. These are then averaged over

84

ten MD runs with different initial velocities and further averaged over for each of the chosen symmetric wavevector in the first quadrant before performing the Lorentzian fitting of these SED data to determine the phonon properties.

The second part of the study with regard to the ripple effect was performed by my PhD colleague Abhishek Kumar and data related to Green Kubo study have been taken from his permission ([164]). For the GK analysis in the pristine graphene simulation was performed using optimized Tersoff potential for a sheet size 150×100 Å with a total 6048 number of atoms. Periodic boundary condition was used in the x and y directions, whereas shrink-wrapped boundary conditions were used in the z-direction with a timestep of 0.001 ps. In order to equilibriate the system at 300 K, initially energy minimization is performed which is then followed by NPT run for 1 ns and then further with a 1 ns of NVT run. The last step under NVT environment which is also our production run is performed for a total of 6 ns from which we obtain the heat current data for each timestep. Thus using this data we conduct the GK analysis to determine TCs which is further explained in detail in the subsequent sections.

6.3   Results

6.3.1   Strain Effect on Thermal Conductivity

Fig. 6.3 shows the BZs of the sample graphene chosen. As we increase the strain in the zigzag direction, the BZ shape also changes as shown in 6.3 where the comparison of BZ's are shown for 0%, 3% and 10% strained pristine graphene samples.

Similar to the dispersion curve obtained for the longer wavelength (ZA mode) in [165], the dispersion curve here is obtained from GULP [140] for the 0.0%, 0.9%, 1.4%, 3.0%, 4.0%, 7.0% and 10.0% strains in the direction of $\Gamma - \mathrm{M}$, as shown in Fig. 6.4. In particular, the ZA modes particularly show the deviation from $\omega \propto k^2$ to $\omega \propto k$ as the strain increases. The frequencies for all other modes i.e TA, LA, ZO, TO and LO modes decreased as we keep on increasing the strain. This flattening occurs because the applied strain weakens the bond stiffness, making it harder for the phonons to propagate

85
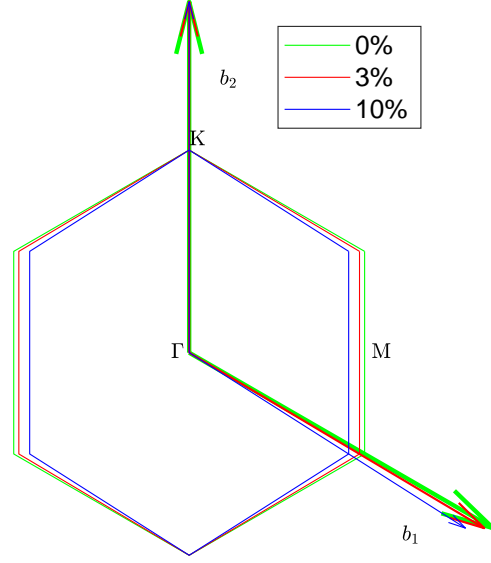
Figure 6.3: BZ comparison of unstrained (0%), 3% and 10% strained graphene. b_1 and b_2 are the reciprocal lattice vectors.
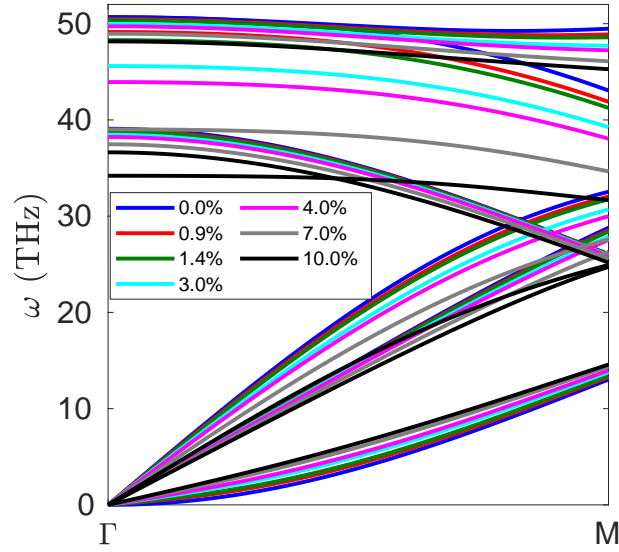
Figure 6.4: Dispersion curve comparison of unstrained and strained graphene along $\Gamma - M$ direction.

through the lattice as quickly as they would in unstrained graphene. The distributions of v_g and phonon lifetimes τ for all the allowed phonon modes in the 1st BZ are shown in Fig. 6.5a and Fig. 6.5b, respectively. As strain is applied, the force constants (which depend on the bond stiffness) between the carbon atoms change. This leads to a modification in the phonon dispersion curves. The effect of such a decrease in the above mode strengths is evident in the overall decrease of the $v_{g_{rms}}$ as strain increases, as shown in Fig. 6.6. The term $v_{g_{rms}}$ signifies a statistical measure of the group velocity, which has

(a) v_g

(b) τ
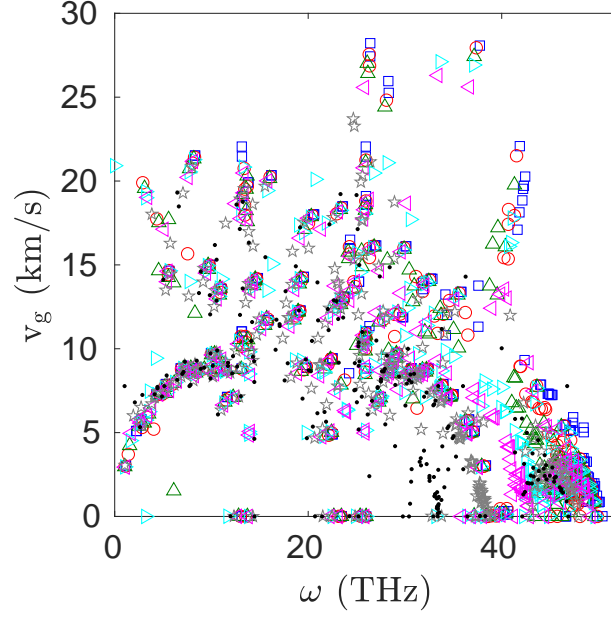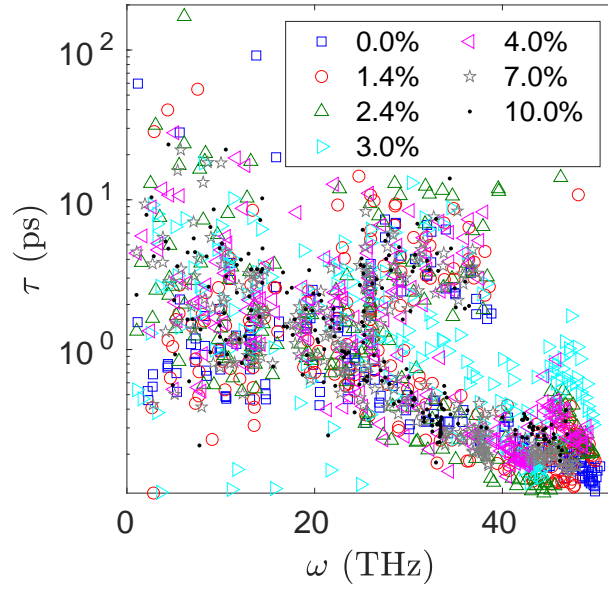
Figure 6.5: (a) v_g (km/s) and (b) τ (ps) comparison of unstrained and strained graphenes.

already been defined in Chapter 5. It can be observed in Fig. 6.5a that the maximum v_g for all the strain occurs in the range of 20-40 THz. As strain increases the distribution tends towards the lower values, which is evident from the decreasing trend of the average squared group velocity $v_{g_{rms}}^2$, as shown in Fig. 6.6a. A key observation is that few modes show null v_g values for the strained graphene samples, which is occurring because of the flattening of the dispersion curves.
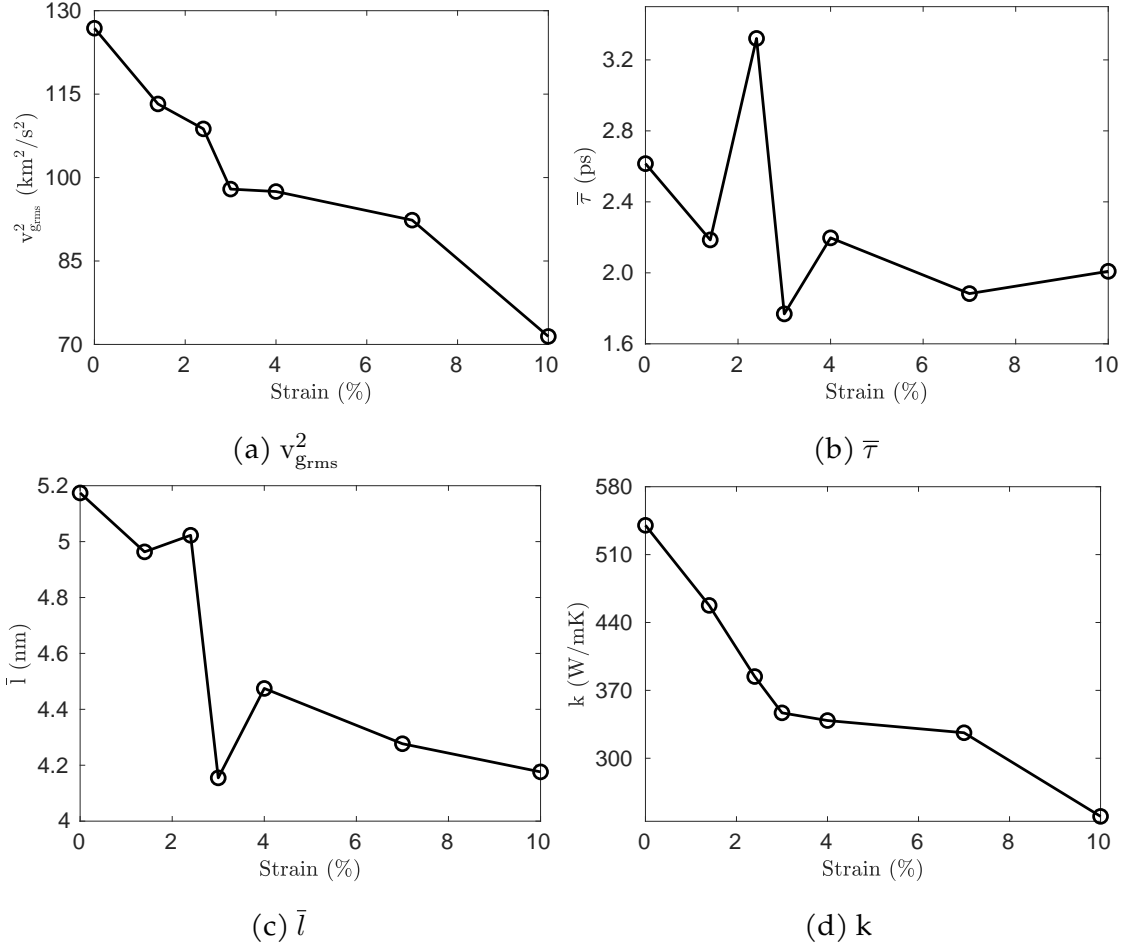
Figure 6.6: (a) $v_{g_{rms}}^2$ (km^2/s^2) (b) $\bar{\tau}$ (ps) (c) $\bar{l}$ (nm) and (d) k (W/mK) comparison of unstrained and strained pristine graphenes for 31×26 Å size.

While strain directly affects the group velocity by altering the lattice dynamics, the scattering processes which dictate lifetime τ are not as sensitive to strain, especially if the strain is not causing substantial defects or changing the material's anharmonicity. Thus there is no evident change in the phonon lifetimes while strain is increased, which can be observed in Fig. 6.5b. The lifetime τ distribution for the allowed phonon modes do not show a significant decrease in the average lifetime as the frequency keeps on

increasing (Fig. 6.6b) and follows a similar trend for all the strains. This is further verified by an almost constant average lifetime trend for all the strain values as shown in Fig. 6.6b. Moreover, we observe from Fig. 6.5b that the τ distribution shows a decreasing trend for all the strains as the frequency increases. Near the BZ centre, the phonon lifetimes of ZA modes are found to be as high as ~ 100 ps. This is because the phonon density of states (PDOS), as shown in Fig. 6.7, is very small near the zone centre. This
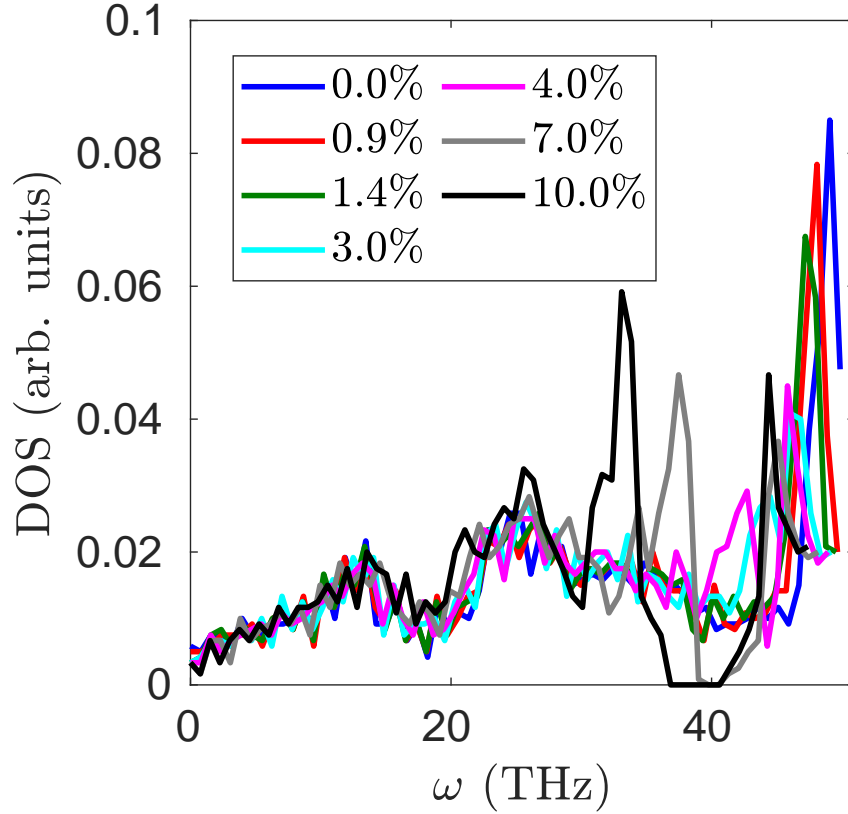
Figure 6.7: DOS comparison.

means that less number of modes are available for scattering to occur such that the momentum can be conserved. This results in lesser scattering and thus higher phonon lifetimes. Apart from the BZ centres, the maximum distribution of τ was found between 20 to 40 THz frequency ([24]) for all the strains because the PDOS is higher in this frequency range. It is also observed in the Fig. 6.7 that as the strain is increased, the PDOS distribution also shifts accordingly towards lower frequency. The mean free path (mfp) is given by $\bar{l} = v_{grms} \times \tau$ which shows an overall decreasing trend (Fig. 6.6c) as the strain is increased which is because of the the decreasing trend of v_g and an almost constant behaviour of τ.

Subsequently, once the mode properties τ and v_g are obtained, we can then calculate the TC of strained graphene structures according to Eq. (5.1). Similar to previous studies, we again choose the wavevectors in the first quadrant due to the symmetry of the BZ [52, 81]. As shown in Fig. 6.6d, the TC keeps on decreasing as the strain is increased [106, 166]. As mentioned earlier, the decrease in TC of $\sim 56\%$ from 0% to 3% is due to the decrease of $\sim 40\%$ alone in v_g^2, as shown in Fig. 6.6a, while the rest of the reduction is due to slight decrease in the τ (Fig. 6.6b) . Similarly, for the region from 3% to 10% strain, the TC decreases by $\sim 31\%$ whereas the v_g^2 decreases by $\sim 28\%$ and the rest of the decrease is attributed by τ decrease. This establishes that the main factor affecting the TC is the v_g when there is only a strain effect.
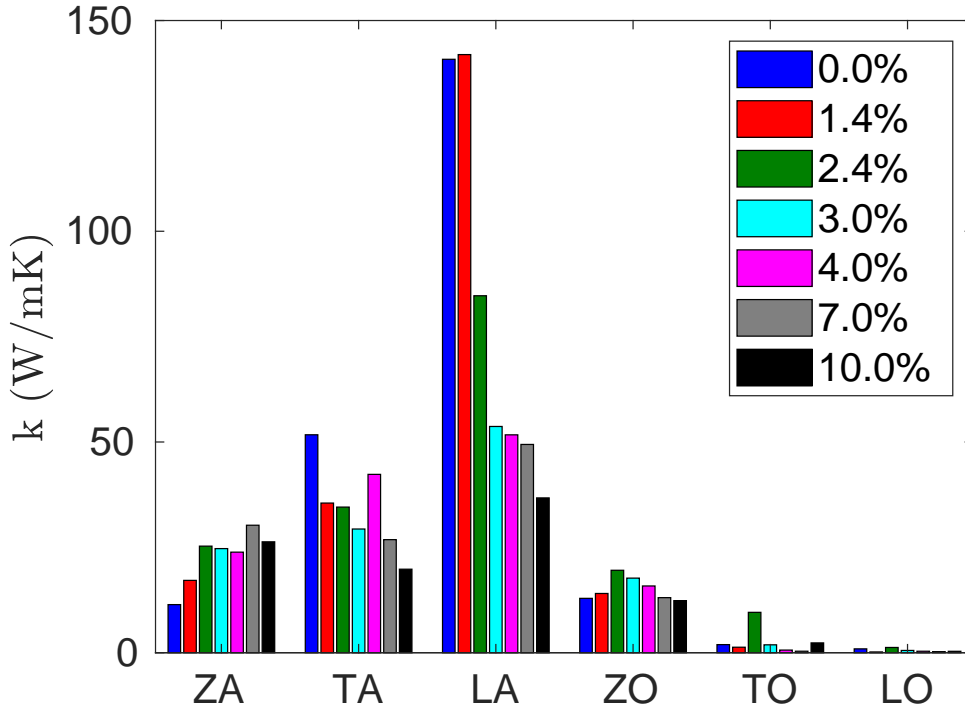
Figure 6.8: Variation of thermal conductivity with strain(%) for pristine graphene

Fig. 6.8 shows the contributions by different modes of graphene to the TC for the 1st quadrant. The total TC is then calculated by summing up the contributions coming from the corresponding symmetry wavevectors of the 1st quadrant wavevectors in the other 3 quadrants of the BZ. It is found that the highest contribution to the overall TC comes from the LA modes, accounting for almost $40 - 67\%$ for all the strain values. The next highest contribution comes from the TA modes, which contribute almost $17 - 24\%$ [53]. The contribution of the ZA modes increased from 5% to 28% as the strain increased from 0 to 10%. This is evident from the fact that the slope of the ZA modes ($v_{g_{ZA}}$) for

different strains keeps on increasing as the stain is increased (Fig. 6.4). The TO and LO modes in the combined sense give a maximum 3% contribution because their v_g is the lowest among all the branches while the ZO modes contribute with a maximum of $6\% - 14\%$. Overall the acoustic modes contribute $84\% - 93\%$ to the total TC of 540, 458, 384, 347, 339, 326 and 240 W/mK for 0.0%, 0.9%, 1.4%, 3.0%, 4.0%, 7.0% and 10.0% strain.

6.3.2   Ripple Effect on Thermal Conductivity

A graphene sheet has intrinsic ripples in it. It has been shown in previous studies that as we keep on increasing the size of a graphene sheet, the ripples start becoming more pronounced [93]. To distinguish between the effects of ripple and strain on TCs, we study strained graphene from 0% to 10% strain for two different sample sizes of 31×26Å with the help of the SED method described in Section 3.2 and 150×100Å with the help of Green-Kubo method described in Section 3.3.

We hypothesize that the total percentage change in TC with increase in strain by the same magnitude should be almost the same for both these samples. Additionally, the 31×26 Å sample being small shows a negligible ripple effect ΔZ of less than 1Å , whereas the $\sim 150 \times 100$ Å sample shows a maximum ΔZ of ~ 15Å as shown in Fig. 6.9a. As there is almost no ripple in the 31×26 Åsample, the NMD analysis on this sample found a total decrease of 31% in the TCs when the strain increased from 3% to 10%. The 150×100 Å samples also do not have ripples, $\Delta Z \approx 0$ Å, in the strain range $3 - 10\%$. The Green Kubo analysis for this range gave a decrease of $\sim 30\%$ in the TC(Fig. 6.9b). That means both samples do not have ripples in the strain range $3 - 10\%$, and therefore, the similar decrease (31% to 30%) in the TC can be attributed to only the strain effect in both these samples. This provides a reasonable ground to argue that the NMD analysis for the smaller sample reveals similar thermal transport behavior to the Green-Kubo analysis for the bigger sample.

Now, for the $0 - 3\%$ strain range in the 150×100 Å sample, there are both ripple and strain effects. We calculated the percentage change in the TC in the 31×26 Å sample by NMD analysis which resulted into $\sim 36\%$ decrease. This decrease is attributed solely to
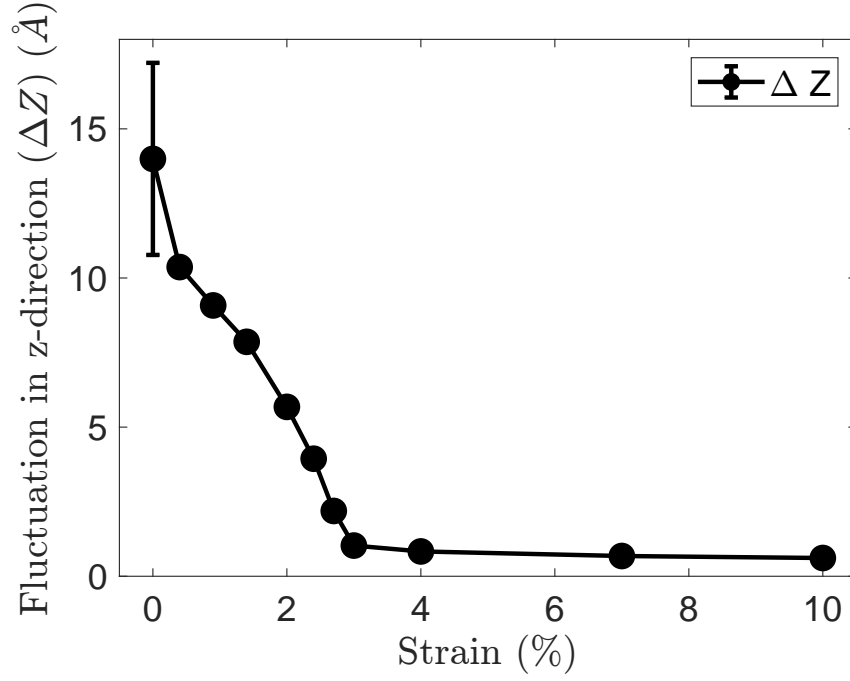
(a) ΔZ
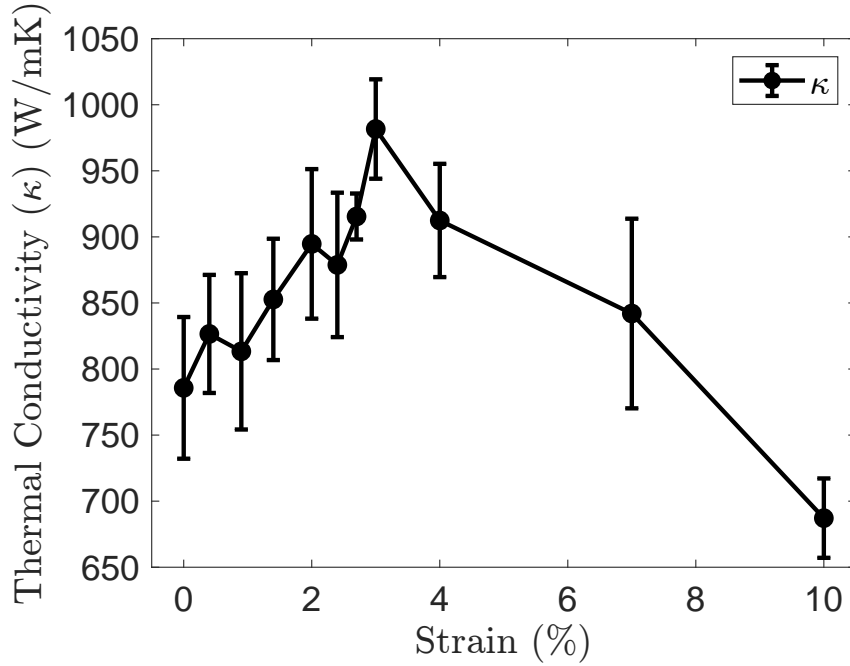
(b) TC data for $150 \times 100 \text{Å}$

Figure 6.9: Variation of thermal conductivity with strain(%) for pristine graphene [164].

the strain effect because there are no ripples in the smaller sample, i.e. $\frac{d\kappa}{\kappa}\big|_{strain}$. Since we already have established that the strain effect is the same on both samples, the same percentage should be in the 150×100 Å sample in the $0 - 3\%$ strain range. Whereas

the Green Kubo analysis on the $\sim 150 \times 100$ Å sample gave an overall increase of $\left(\frac{d\kappa}{\kappa}\big|_{overall}\right) \sim 25\%$ in the TC Fig. 6.9b. Thus, according to the Eq. (6.2), where we have hypothesized that the strain and the ripple effects can be linearly decoupled, an increase of $\sim 61\%$ should be attributed to the ripple effect $\left(\frac{d\kappa}{\kappa}\big|_{ripple}\right)$.

$$\frac{d\kappa}{\kappa}\bigg|_{overall} = \frac{d\kappa}{\kappa}\bigg|_{strain} + \frac{d\kappa}{\kappa}\bigg|_{ripple} \tag{6.2}$$

In other words, we have $\frac{d\kappa}{\kappa}\big|_{strain} = \frac{d\kappa}{\kappa}\big|_{overall} - \frac{d\kappa}{\kappa}\big|_{strain} = 25\% - (-36\%) = 61\%$. This means when we had calculate the bulk TC of the SLG [81] as 1484.5 W/mK, the reduction in the ripple could increase this bulk value to around 61% more TC, which will be around 2390 W/mK.

6.4   Summary

In this study, we have extensively investigated the impact of strain and ripple effect on the TC of single layer graphene (SLG). Our computational analysis on a small sample size has very less out-of-plane fluctuations ΔZ vibration. Using the lattice dynamics approach, it is revealed that the application of strain, particularly in the zigzag direction, leads to significant changes in the phonon dispersion characteristics, notably affecting the out-of-plane acoustic (ZA) modes. This strain induces a transition from a quadratic to a linear relationship between frequency and wavevector, which is directly linked to a marked reduction in group velocity v_g in the ZA modes. The reduction in v_g is primarily attributed to the weakening of bond stiffness under strain, which in turn reduces the phonon propagation. The PDOS shifts towards the lower frequencies as the strain is increased. The NMD analysis provides additional insights into the phonon mode contributions, demonstrating that the LA modes are the highest contributors to the TC, followed by the TA modes, with TO and LO modes being the lowest contributors across all the strain values. Additionally, our analysis indicates that phonon lifetimes τ are less sensitive to strain. Quantitatively, the strain leads to a significant decrease in TC, with our results showing up to a 30% reduction between $0 - 3\%$ strain. The ripple effect ΔZ, a measure of the degree of out-of-plane deformation, further amplifies the reduction in

TC. The Green Kubo study on a larger sample size having prominent ΔZ has intrinsic ripple effects, and when strain is applied, these two effects combine to reduce the TC of graphene. Using the NMD results of graphene without a ripple, we conclude that the ripple will alone decrease the TC by $\sim 61\%$ in the graphene samples. Thus these findings suggest that careful control of strain and ripple effects could be employed to tailor the thermal properties of graphene for specific applications for the design and optimization of graphene-based thermal management systems.

Chapter 7

Phonon Dynamics and Thermal Properties in 2D FPU-β Lattices

This chapter focuses on studying the thermal properties of a 2D system based on the FPU-β potential. Using SED method and NMD analysis, this work explores for the first time important characteristics of phonon behavior, such as their lifetimes, group velocities, and overall thermal conductivities in 2D. We fully investigate how heat is conducted through anharmonic 2D systems modeled by the FPU-β potential. We look closely at the unusual way the thermal conductivity (TC) behaves in these systems, especially as the system size grows. This study provides new insights into the challenges of understanding heat transport in these materials.

In this study, we first investigate the thermal transport properties of a two-dimensional square lattice system (Fig. 7.1) using the Green-Kubo method, incorporating the Fermi-Pasta-Ulam (FPU)-β potential (V_{FPU}) in Eq. (7.1):

$$V_{\text{FPU}}(\eta) = \frac{1}{2}\eta^2 + \frac{\beta}{4}\eta^4 \tag{7.1}$$

where $\eta = r - r_0$ is the relative displacement of inter-particle distance (r) with respect to the equilibrium distance r_0. The term β is used to quantify the strength of quartic anharmonic interaction which introduces the non-linearity into the system. The Green-
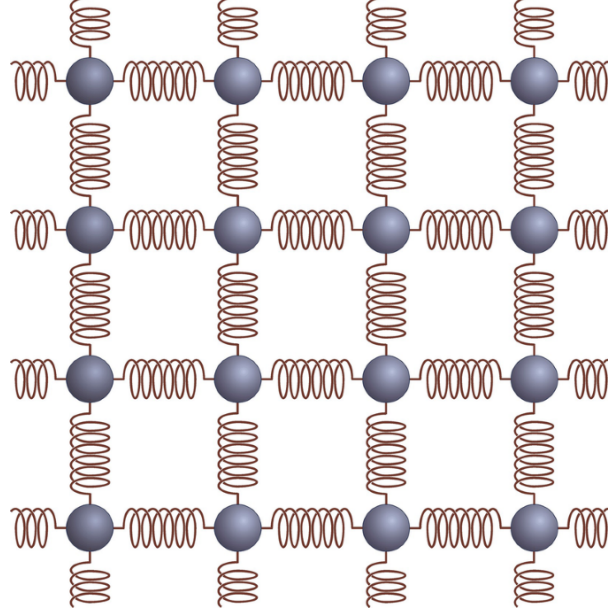
Figure 7.1: Schematic of FPU square lattice joined with non-linear springs.

Kubo linear response theory [167] provides an alternative definition of thermal heat conductivity **k** in the form of following expression for the TCs tensor:

$$k_{\alpha\beta} = \lim_{\tau_I \to \infty} \frac{1}{k_B V T^2} \int_0^{\tau_I} \langle J_\alpha(0) \otimes J_\beta(t) \rangle dt, \tag{7.2}$$

where $\tau_I (= I \Delta t_{MD})$ is the integration timestep, Δt_{MD} is the time step in the molecular dynamics simulation, I is the total number of integration steps and **J** is the heat current vector (for detailed explanation please refer Section 3.3), while the other terms have their usual meaning. As our GK model is homogeneous 2D non-linear square lattice, the TCs is represented equally by any of the diagonal components within the transport coefficient tensor as defined in Eq. (7.2) as $k = k_{xx} = k_{yy}$. We also utilize the SED method to calculate the phonon properties.

The organization of this study is structured as follows. In Section 7.1, we outline the methodology used for preparing FPU-β samples. Section 7.2.1 details the molecular dynamics (MD) simulations conducted to support the Green-Kubo (GK) along with the results obtained from the study. It is followed by the results for the SED based

NMD approach in Section 7.2.2, where we calculate the phonon group velocities using the harmonic lattice dynamics capabilities of the GULP package and determine phonon lifetimes by fitting the SED data to a Lorentzian function. Additionally, this reports the bulk thermal conductivities of FPU-β systems utilizing the SED method. Finally, we conclude in Section 7.3 by summarizing our findings and offering recommendations for future research directions.

7.1 Sample Preparation

We consider a two-dimensional square lattice model based on the Fermi-Pasta-Ulam (FPU)-β potential governed by Eq. (7.1) where all numerical simulations with this potential have been performed with $\beta = 0.025$. The atoms are arranged to form a uniform grid structure, where each atom interacts only with its nearest neighbors. Without loss of generality, the equilibrium distance between neighboring atoms is set to 1.0 LJ units, which defines the uniform lattice spacing, $a = 1.0$ LJ units. Each atom in the lattice is placed at a position defined by the integer indices (i, j), where $1 \leq i \leq N_x$ and $1 \leq j \leq N_y$, corresponding to the number of unit cells in the x and y directions, respectively. The origin of our Cartesian reference frame is chosen such that the two-dimensional equilibrium position vector, $\mathbf{r}_{ij}^0$, aligns with (i, j).

To simplify the model and reflect the short-range nature of interatomic interactions $V_{FPU}(\eta)$ (as given in Eq. (7.1)), which depends on the relative displacement η with respect to the equilibrium distance $r_0 = 1$ LJ units, we use a cutoff radius of 1.10 LJ units beyond which the interaction potential is considered negligible. The mass of each atom is, without loss of generality, set to 1.0 LJ units. Additionally, the energy parameter ϵ and the time unit are both defined as 1.0 LJ units, ensuring the system is normalized and dimensionless. This choice of units provides a consistent framework for our numerical simulations and simplifies the equations of motion. For the same physical unit cell system, we first study with Green-Kubo method which is later followed by SED based study.

7.2 Results

7.2.1 Green-Kubo

The TCs of our system was determined using the Green-Kubo formalism, which relies on analyzing the heat current autocorrelation function (HCACF) over an extended simulation period. The MD package LAMMPS [149] has been used for all our simulations. We used a $10 \times 10 \times 1$ supercell containing 100 atoms to balance computational efficiency with the need to capture essential thermal transport features. This supercell size was chosen as it provides a sufficiently large system to reduce finite-size effects while remaining computationally feasible.

To initialize our simulations, we equilibrated the system using the canonical ensemble (NVT) with a Nosé-Hoover thermostat. The Nosé-Hoover thermostat was selected because it provides an efficient way to control the temperature and ensure that the system samples the correct canonical distribution. The temperature was maintained at $T = 8.618 \times 10^{-6}$ LJ units (T is the reduced temperature in units of the Boltzmann constant) for 10^5 timesteps. This temperature value was specifically chosen based on the reduced units of the Lennard-Jones system, ensuring consistency and enabling meaningful comparison with theoretical models. After the equilibration phase, we removed the thermostat and transitioned to the microcanonical ensemble (NVE) for another 10^5 timesteps. The NVE ensemble was used to conserve the total energy of the system, which is crucial for the Green-Kubo analysis. By using the NVE ensemble, we allow the system to evolve naturally, without external influences, thereby providing an accurate representation of energy transport.

The production run, essential for calculating the HCACF, was carried out over 2×10^7 timesteps. This extensive duration was necessary to ensure that the HCACF decays fully and that enough data points are collected to perform a robust statistical analysis. The heat current vector, $\mathbf{J}(t)$, was sampled at every single timestep, providing high temporal resolution. In order to enhance the reliability of our TCs results and minimize statistical errors, we performed 30 separate simulations. Each of these simulations was initialized with distinct, randomly generated conditions to improve statistical av-

eraging. This method effectively reduces noise and allows us to better capture the true thermal characteristics of the system, given the inherent fluctuations associated with thermal transport properties.

The time-discretized TCs k, as given by Eq. (7.3), was computed from the HCACF, $\langle \mathbf{J}(t) \otimes \mathbf{J}(0) \rangle$, starting from the point where the autocorrelation function first decays to zero because it marks the region where meaningful integration can occur (Fig. 7.2). This occurs at $\sim 3 \times 10^4$ timesteps.
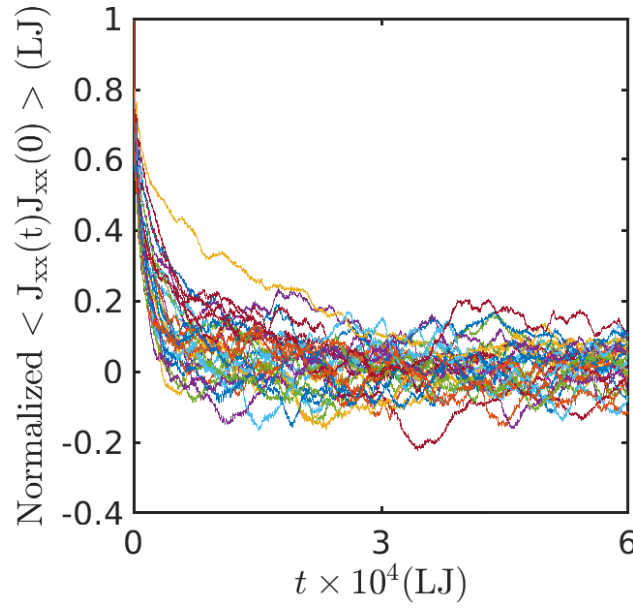
Figure 7.2: Normalized HCACF for 30 different ensemble replicas run under the NVE ensemble.

$$\mathbf{k} = \lim_{\substack{S,I \to \infty \\ S \gg I}} \frac{\Delta \mathrm{t}_{\mathrm{MD}}}{\mathrm{Vk_B T^2}} \sum_{a=1}^{I} \frac{1}{S-a} \sum_{b=1}^{S-a} \mathbf{J_{a+b}} \otimes \mathbf{J_b} \qquad (7.3)$$

Here Δt_{MD} is the time step in the molecular dynamics simulation taken as 0.01 LJ units, V is the volume of system which is 100 LJ units of distance, k_B is the Boltzmann constant, T is the same temperature as was chosen for the GK method equal to 8.618×10^{-6} LJ units. $\mathbf{J}_{a+b}$ and $\mathbf{J}_b$ are heat current vectors at time steps $a+b$ and b, respectively whose dyadic product gives the HCACF. The HCACF is summed over I intervals where I being the number of starting points for calculating autocorrelations which was taken at every 10^3 timesteps in order to improve the accuracy of the autocorrelation. A total

production run timestep of $S = 2 \times 10^7$ ensured that $S \gg I$ for improving the statistical reliability of the result Section 3.3.

The average TCs derived from these simulations exhibits a logarithmic dependence on time, as displayed in the semi-log plot in Figure 7.3. This logarithmic behavior is in accordance with the several previous studies which also showed the logarithmic growth on any finite system for 2D case [120, 123, 124] which validates our findings for the present set of studies.
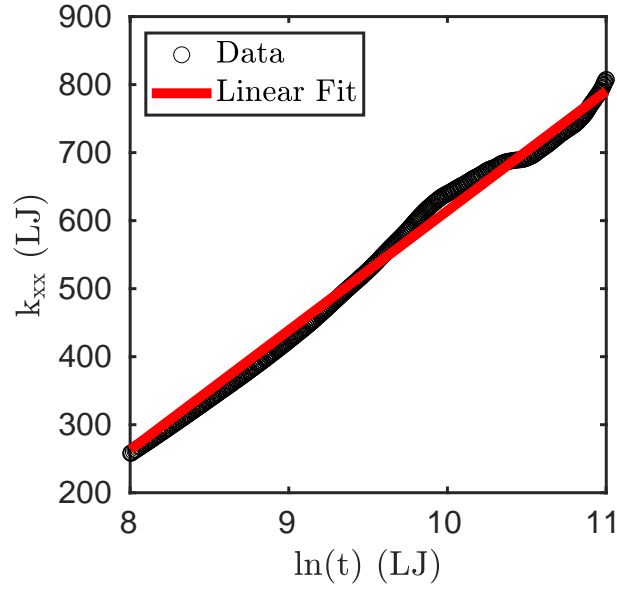
Figure 7.3: $\kappa_{xx} \propto \ln(t)$ dependence for a system size of 10×10 square unit cells. The data points have been obtained by averaging over 30 different initial conditons in order to get a better statistical averaging for the system.

The initial focus on the Green-Kubo (GK) method, which studies TC as a function of the logarithm of time, $\ln(t)$, provides a foundation for understanding the temporal evolution of heat transport properties in our system. The reason for starting with this approach is rooted in the observation that asymptotic behavior over long timescales is expected to be analogous to the asymptotic behavior in space, as observed by Lippi and Levi [120] and given by the relationship $N \sim \tilde{c}\tau$. Here, N represents the spatial system size, τ denotes the integration time, and $\tilde{c}$ is a proportionality constant [120]. However, this relation also highlights the presence of finite size effects when the integration time, τ, becomes significantly larger than N/c. These effects, which stem from the finite spatial extent of the system, have been effectively observed by analyzing the behavior

of $C(\omega)$, the Fourier transform of the time correlation function $C(\tau)$, particularly in the low-frequency range. The authors [120] also argue that for different values of N, the curves of $C(\omega)$ align well up to a certain frequency, $\omega_c(N) \approx c/N$, beyond which finite size effects cause them to diverge from the expected asymptotic trend. This finite size behaviour motivates our transition to the Normal Mode Decomposition (NMD) method, where we study TC as a function of the logarithm of system size, $\ln(N)$. This spatial approach helps us understand how thermal transport properties scale with the system size and complements the temporal insights gained from the GK method. Moreover, the GK method effectively calculates TCs by analyzing heat current fluctuations, however, it falls short in providing insights into specific phonon modes and their contributions to thermal transport. The SED approach complements this by resolving the vibrational characteristics of phonons, such as their lifetimes and group velocities.

7.2.2 SED

7.2.2.1 Simulation details

As explained in the Section 7.1, the unit cell information of the SED based system remains the same. We utilized the LAMMPS molecular dynamics software package [149] to perform our simulations in order to get the atomic positions and their respective velocities and at given timesteps. We prepare the simulation setup for our 2D square lattice model based on the FPU-β potential, employing periodic boundary conditions (PBC) in all directions. The molecular dynamics (MD) simulations were conducted using a timestep of 0.01 LJ units of time, ensuring numerical stability and accurate integration of the equations of motion. The simulation begins with equilibration in the canonical ensemble (NVT) for 10^5 timesteps, controlled using a Nosé-Hoover thermostat. This ensures that the system reaches the target temperature of 8.618×10^{-6} LJ units. Following equilibration, the thermostat is removed, and the system is evolved under the microcanonical ensemble (NVE) for another 10^5 timesteps to conserve total energy and achieve a steady state. To capture phonon properties with high resolution, we then record the atomic positions and velocities during a subsequent NVE simulation

run, lasting 2^{22} timesteps. This extensive duration guarantees that the system samples the phonon spectrum comprehensively, particularly capturing low-frequency modes. We set the step size for data output as 2^7 timesteps, chosen to ensure that the highest frequency lattice vibrations are captured accurately using the spectral analysis. To achieve statistical averaging, the entire procedure is repeated for 10 different ensembles for each of the system sizes chosen in the current study, each initialized with unique random velocities. This averaging process reduces noise and increases the reliability of the calculated phonon properties, providing a comprehensive understanding of thermal transport in the 2D FPU-β lattice model.

Similar to our previous studies, the choice of wavevector is crucial in the NMD analysis, as selecting an incorrect wavevector can lead to inaccurate resonant peaks and phonon properties [151]. We adopt the approach by Qiu and Ruan [51, 52], utilizing the symmetry of the Brillouin Zone (BZ) and the simplicity offered by BZ discretization. Specifically, we select the allowed wavevectors in the full BZ. For a chosen wavevector in the full BZ, we calculate the SEDs for all these symmetric copies, average them, and further average over ten MD simulation runs with different initial velocities. This process is carried out before fitting the SED curves to extract the phonon properties.

7.2.2.2 Single-size system analysis

Using the GULP package, which is based on harmonic lattice dynamics, we calculate the phonon dispersion curves along the symmetric Γ-X direction, as illustrated in Fig. 7.4. These results satisfy the analytical relations given below which can be derived easily for the harmonic part of the FPU-β potential modeling the 2D square lattices:

$$\omega_1 = 2\left|\sin\frac{\kappa_x}{2}\right|, \quad \omega_2 = 2\left|\sin\frac{\kappa_y}{2}\right|, \tag{7.4}$$

where $\omega_{1,2}$ are the dispersion frequencies corresponding to the wavevector $\boldsymbol{\kappa} = \kappa_x\hat{\mathbf{i}} + \kappa_y\hat{\mathbf{j}}$, 1 and 2 correspond to the LA and TA branches, and $\hat{\mathbf{i}}$ and $\hat{\mathbf{j}}$ are the unit vectors, respectively, along x and y axes. Following these relations, the magnitudes of the group velocities for two branches 1 (LA) and 2 (TA) are $v_{g1,2} = \left|\cos\frac{\kappa_{x,y}}{2}\right|$, and therefore, we
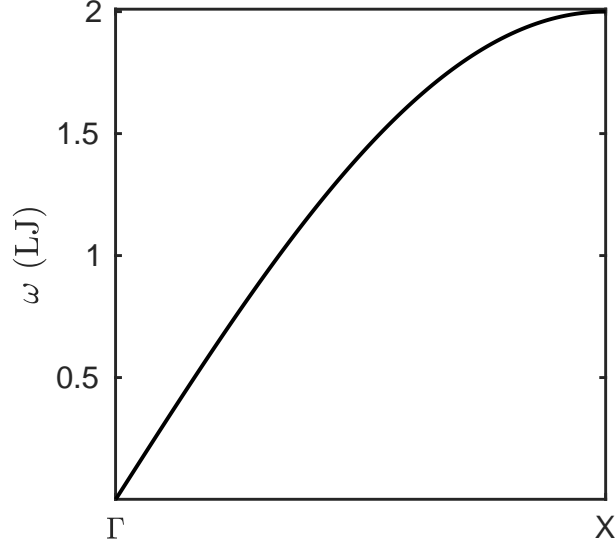
Figure 7.4: Dispersion of FPU-β in the hi-symmetry Γ–X direction. For the 2D system, only 2 acoustic branches, TA and LA branches, exist, which are highly degenerate.

can express these magnitudes of group velocities as

$$v_{g1,2} = \cos(\frac{\kappa_{x,y}}{2}).\mathrm{sgn}(\sin(\frac{\kappa_{x,y}}{2})) \tag{7.5a}$$

$$\begin{cases} \mathrm{sgn} = -1, & \sin(\frac{\kappa_{x,y}}{2}) < 0 \\ \mathrm{sgn} = 0, & \sin(\frac{\kappa_{x,y}}{2}) = 0 \\ \mathrm{sgn} = 1, & \sin(\frac{\kappa_{x,y}}{2}) > 0 \end{cases} \tag{7.5b}$$

These results are also consistent with the dispersion curves reported by Benettin [168].

As explained in the previous chapters, once satisfactory results for the dispersion curves have been obtained, we calculate the SEDs using Eq. (3.11) and fit the data with the Lorentzian function in Eq. (3.12). The Lorentzian curve fitting process is highly non-linear and performed in a semi-automated manner, where the fitting parameters are adjusted by visually inspecting each fit based on the system's length and width. Once these parameters are optimized, they can be applied to fit the SED curves of other samples with varying lengths and widths. Fig. 7.5 presents the Lorentzian fit for the TA phonon mode at the wavevector $\kappa = (-0.48, -0.46, 0.0)$ in the reduced coordinate

103
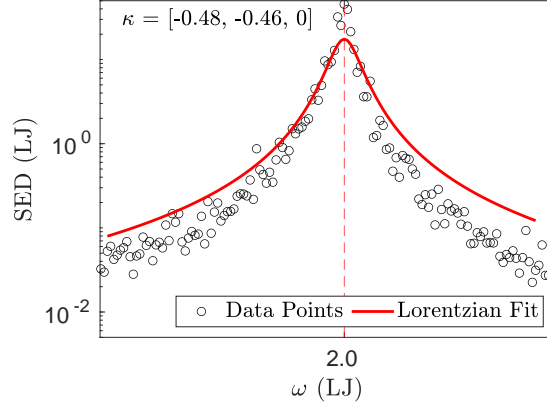
Figure 7.5: The Lorentzian function fits for the SED data for the SLG sample with $50 \times 50 \times 1$ primitive unit cells are presented. The LA dispersion branch for the wavevector $\boldsymbol{\kappa} = (-0.48, -0.46, 0.0)$ is shown for illustrative purposes. The red dashed line indicates the resonant frequency (ω_0) for this particular mode.

system of reciprocal space for the $28 \times 28 \times 1$ primitive unit cells. Similar fits are observed for other phonon modes.

To gain a deeper understanding into the behavior of individual phonon modes, we choose a system size of $N = 50 \times 50 \times 1$. This choice is deliberate, as it represents the largest system size analyzed in our size-dependent study. In a two-dimensional system, only two acoustic modes exist: the transverse acoustic (TA) and the longitudinal acoustic (LA) modes which are degenerate along not only the hi-symmetry directions but also across the entire BZ for square lattices. We differentiate these modes based on their respective eigenvectors with components $(0, 1)$ and $(1, 0)$ in the reciprocal space as TA and LA mode respectively. First, we examine the phonon lifetime distribution.

In order to get a quantitatively clearer picture of the dominant modes contributing to the phonon properties such as τ and v_g, we will try to calculate an average measure of these properties denoted as $\overline{\tau}$ and $\overline{v_g}$, respectively, whose calculation we explain now. As observed in the lifetime distribution, there are specific ω's where the phonon modes are concentrated, and therefore, we divide the whole ω domain into *bins*. Each bin has a width of $\Delta\omega = 0.22$ LJ units of frequency. We then get the total number of allowed TA or LA modes which lie in the frequency range $[\omega, \omega + \Delta\omega)$ and this term from now on will be termed as *modes per bin (MPB)*, as shown in Fig. 7.6d. We then sum all τ's ($\sum \tau$) which lie in the $[\omega, \omega + \Delta\omega)$ and then divide the sum by the MPB in the same

(a) τ

(b) τ

(c) $v_{g_{rms}}$

(d) Contribution to TC from TA and LA modes
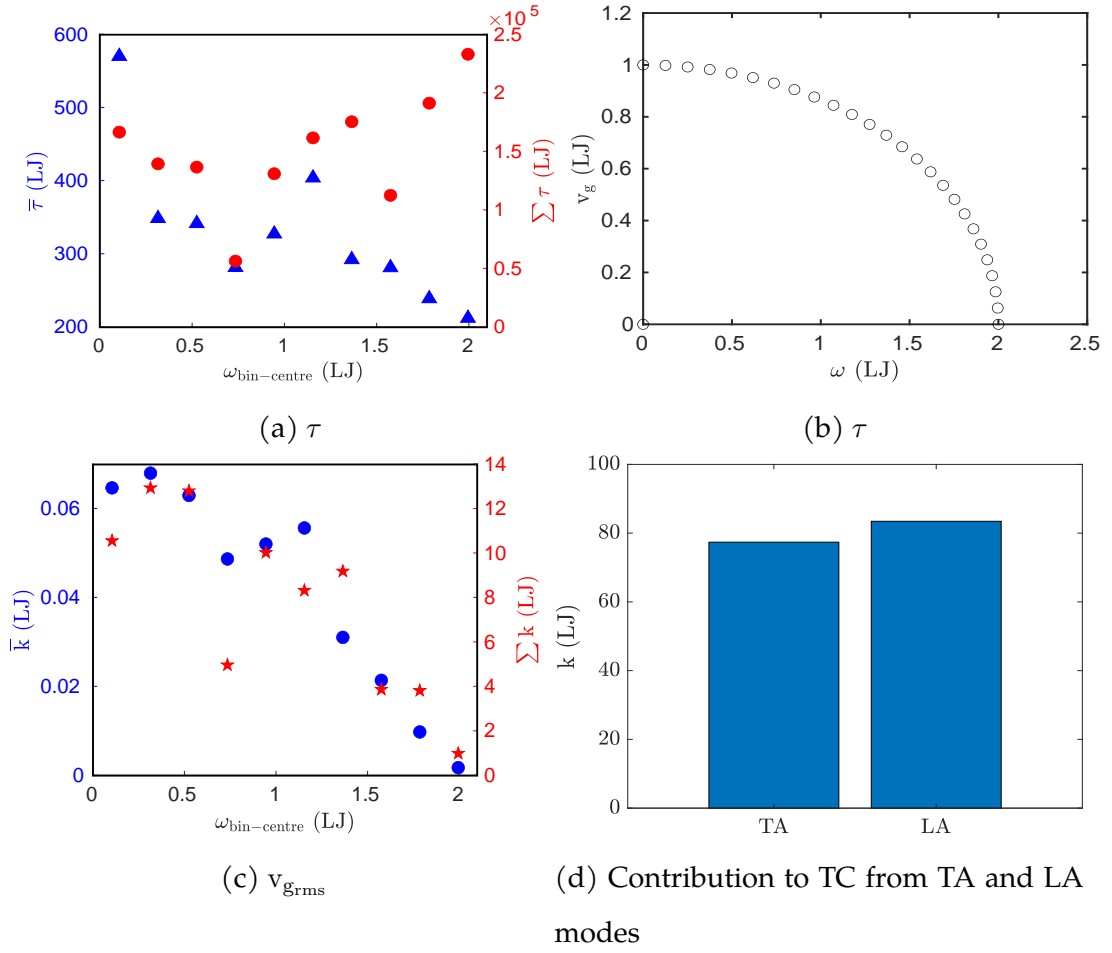
Figure 7.6: (a) Phonon lifetime distribution wrt bin for system size of $50 \times 50 \times 1$, (b) vg, (c) The $\overline{k}$ and $\sum k$ reveals these two decrease wrt frequency, (d) TA nad LA modes contribute almost equally

range to get $\bar{\tau}$ as shown in Fig. 7.6a. Further, the v_g distribution is shown in Fig. 7.6b which follows the Eq. (7.5). A similar procedure like $\bar{\tau}$ is followed to get $\bar{k}$ which shows that the lower frequency modes contribute more in terms of per mode than the higher frequency modes because of their higher lifetimes as shown in Fig. 7.6c. These modes are distinguished into LA and TA modes and their contributions is almost equal (as shown in Fig. 7.6d) to the overall TC because of the homogeneous nature of the system.

7.2.2.3 Size-dependent analysis

In our previous studies (Section 4.2.3), we established the size-dependent nature of the SED method based normal mode decomposition (NMD) analysis. Thus, we extend our investigation to analyse various system sizes. The study focuses on square lattices, and given the symmetric nature of the Brillouin Zone (BZ), which itself forms a square, we limit our TC calculations to the full BZ for all system sizes.

Similar to previous Section 7.2.2.2 and following the similar approach, we study $N = N_x \times N_y$ primitive unit cell samples, where $N = 16, 20, 24, 30, 40, 50$ respectively. Having obtained the full BZ contribution for each of the respective sizes, we try to fit the data points for the TC on a natural logarithmic scale of size N. The results, presented in Fig. 7.7d, reveal a logarithmic divergence of TC with increasing size N which follows the following linear fitting equation with $\ln N$:

Lippi and Livi [120] give an analytical justification for this logarithmic dependence with the help of normal mode coordinates and the linear response theory based self-consistent mode coupling theory (SMT)[120]. It can be shown that the ensemble average of the heat flux auto-correlation function is directly proportional to $1/t$. This means, the Green-Kubo expression for the TC in Eq. (7.2) becomes directly proportional to $\ln t$, and since the asymptotic behavior in space is equivalent to the asymptotic behavior in time for the model [120], i.e system size $N = \tilde{c}t$, where $\tilde{c}$ is speed of sound in the non-linear medium, then $k \propto \ln N$. This size-dependent behavior can be attributed to the increasing number of contributing phonon modes as the system size grows. As the system size N increases, more modes become available for thermal transport, leading to the observed logarithmic scaling.
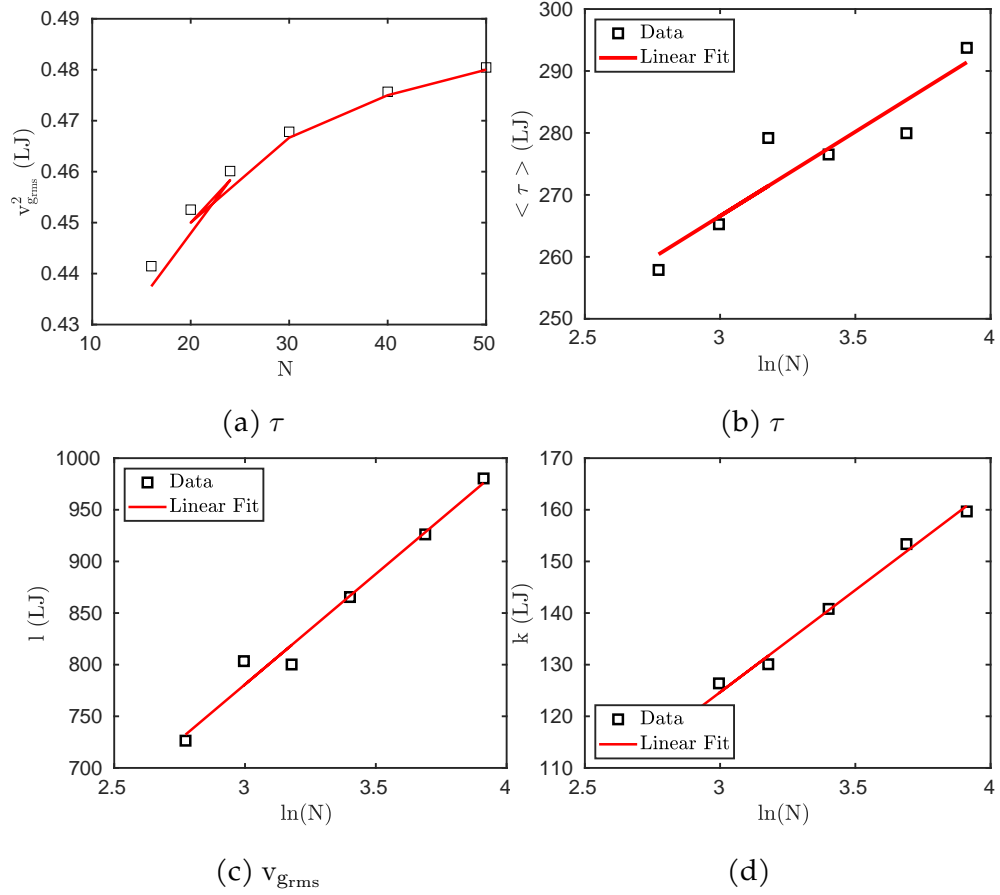
Figure 7.7: For system size of 16, 20, 24, 30, 40, 50 the (a) Squared $v_{g_{rms}}^2$ tends towards a constant value of 0.5 LJ units. Whereas the logarithmic trend is observed for these system sizes in (b) Mean phonon lifetime ($<\tau>$), (c) Average mean free path (l) and (d) Thermal conductivity (k).
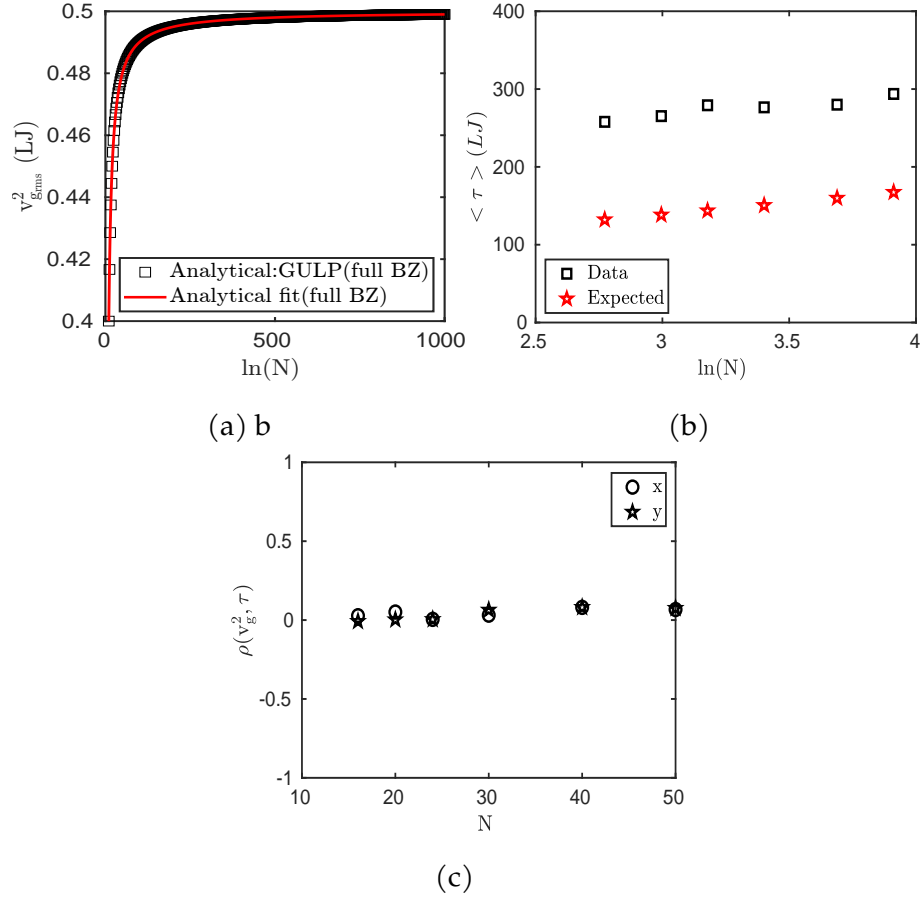
Figure 7.8: (a) Squared root mean square (rms) of group velocities ($v^2_{g_{rms}}$) comparison of raw data (obtained from GULP) and analytical data match exactly across the given sizes. It is found that the $v^2_{g_{rms}} \to 0.5$ as size increases. (b) Obtained $< \tau >$ data shows a similar trend with the expected

To further understand the origins of this trend, we examine the two critical components of TC: the phonon group velocity and phonon lifetimes. Specifically, we analyze the root mean square (rms) of group velocities, $v_{g_{rms}}$ and the average phonon lifetimes across different system sizes N. Rather than focusing on individual acoustic modes, we take averages over all available phonon modes within the full BZ. The calculated value of $v_{g_{rms}}^2$ shows a steep increase for the small system size and then it tends towards a constant value of 0.5 LJ units for the larger system size as shown in Fig. 7.8a where $v_g^2 = 0.5 - 1/N$ relationship is being followed.

On the other hand, $\langle \tau \rangle$ increases as the system size increases. Thus this trend in $\langle \tau \rangle$ is the main reason for the overall logarithmic increase in TC which was shown earlier in Fig. 7.7d. Now, similar to Section 5.3, we find that the correlation coefficients between $v_{g_{rms}}^2$ and $< \tau >$ along both x and y axes are close to 0 for different values of N, i.e., $\rho(v_{g_{rms}}^2, < \tau >) = 0$, as shown in Fig. 7.8c. Therefore, $k = \sum_{\nu=1,2} \sum_i^{2N^2} c_v v_g^2 \tau \approx 2N^2 c_v v_{g_{rms}}^2 < \tau >$, where $2N^2$ is the total number of allowed modes in both $\nu = 1$ (LA) and $\nu = 2$ (TA) branches of the full BZ. The approximation sign appears because there exists a small non-zero correlation between $v_{g_{rms}}^2$ and $< \tau >$. Also, for a given volume $V = N \times N \times 1$ of the system, the classical mode specific volumetric specific heat can be taken as $c_v = \frac{k_B}{V} = \frac{1}{V} = \frac{1}{N^2}$, since $k_B = 1$ in the LJ units. Therefore, by assuming that for a general larger size system $2N^2 c_v \approx 2$, the estimated TC, k_{estm}, for the full BZ becomes

$$k \approx k_{estm} = 2 v_{g_{rms}}^2 < \tau > \tag{7.6}$$

We calculated this k_{estm} for different values of N and found that $k_{estm} \approx 0.9k$. With the help of Eq. (7.6), therefore, it can be argued that the logarithmic divergence of the thermal conductivity calculated only from full BZ modes is primarily due to the logarithmic divergence of $< \tau >$ since $v_{g_{rms}}^2$ remains the same for all higher values of N. This is a significant result. In future, we intend to explore various β values, thereby we intend to extend our model to more realistic solids where anharmonic effects play a significant role.

7.3 Summary

The motivation behind this work comes from the need to understand the thermal transport properties in two-dimensional anharmonic solids, specifically within the context of the FPU-β model. Given the significance of TC in designing materials for advanced applications, especially where heat management is critical, our study aims to explain the underlying mechanisms driving TC behavior in such systems. By employing the equilibrium molecular dynamics-based Green-Kubo (GK) analysis and the SED method, we systematically investigate how size and phonon properties influence TCs.

We began our investigation with the GK method to explore the time dependence of TC. The analysis revealed that TC is proportional to $\ln(t)$. This logarithmic dependence emphasizes the importance of temporal evolution in thermal transport and validates findings from previous studies, thus ensuring the consistency and robustness of our approach. Following the GK study, we transitioned to the NMD method to investigate into phonon transport properties. Our first focus was on a detailed analysis of the $N = 28 \times 28 \times 1$ system size. This study highlighted the behavior of individual phonon modes. We observed that the average lifetimes of TA and LA modes are comparable. The TC contributions from the TA and the LA modes were found to be nearly equal.

Subsequently, we extended the NMD analysis to study the size-dependent behavior of TC. The results revealed a logarithmic divergence of the TC with the system size N. As the system size increased, more phonon modes participated in heat transport, leading to an enhanced TC. We also found that the rms of group velocities for all modes, v_{grms}^2, becomes constant for bigger system size N, however, the mean of all lifetimes, $< \tau >$, keeps on increasing for as the system size increased. Through our correlation based analysis, we then showed that the logarithmic divergence of the TC can be attributed primarily to the $\overline{\tau}$ with respect to N.

Thus the complementary use of the GK and NMD methods provided a comprehensive understanding of thermal transport. The GK method established the temporal aspects of TC behavior, while the NMD approach offered insight into spatial dependencies and phonon properties across the frequency domain. Looking forward, future research will focus on extending this analysis to varying anharmonicity parameters, β,

to develop a robust analytical model for the TCs. This model will enable better predictive capabilities for real anharmonic materials, linking microscopic phonon behavior with macroscopic thermal properties.

This page was intentionally left blank.

Chapter 8

Conclusion

This thesis addresses the critical issue of thermal conductivity (TC) in low dimensional materials, such as graphene and other two-dimensional structures, which are increasingly important in modern technologies requiring effective heat dissipation. It systematically investigates the factors influencing TC by employing advanced computational techniques, including both equilibrium and non-equilibrium molecular dynamics (MD) simulations. We begin with a comprehensive analysis of graphene-based systems, specifically single layer graphene (SLG), AB-stacked bilayer graphene (AB-BLG), and twisted bilayer graphene (tBLG), focusing on how interlayer interactions in bilayer graphene and their respective phonon modes contribute to the heat transport along with the study of size effects. The research then explores the impacts of structural modifications, including grain boundaries (GBs) with different misorientation angles and strain, on thermal properties. Furthermore, we examine the thermal transport characteristics of two-dimensional anharmonic solids using the FPU-β model, highlighting how anharmonicity and finite size effects influence TC behavior.

To explore these factors, we utilize MD simulations to model atomic behavior and

interactions, providing insights into heat transport mechanisms at a microscopic level. We apply techniques such as the Non-equilibrium molecular dynamics based Direct method to get the size dependent TC, equilibrium molecular dynamic based Green-Kubo (GK) and the spectral energy density (SED) based normal mode decomposition (NMD) to quantify the contributions of various phonon modes—vibrational patterns critical for heat conduction. By integrating these approaches, we capture the dynamic behavior of phonons over time and their spatial distributions, leading to a deeper understanding of thermal transport in these materials.

The following sections will briefly highlight the main results. We will first analyze how size affects TC in the single layer and bilayer graphene systems (chapter 4). Next, we will delve into the impact misorientation angles in SLG with GB (chapter 5), followed by an investigation of strain and ripple effects in SLG (chapter 6). Finally, we will present our findings on the FPU-β model, focusing on the fundamental aspects of anharmonic heat transport, including both temporal and spatial characteristics of phonon properties (chapter 7). Through this structured investigation, we aim to enhance our knowledge of thermal transport phenomena in low-dimensional materials and contribute to future advancements in thermal management technologies.

The key takeaways from these studies are as follows:

- **Phonon properties of SLG, AB-BLG, and tBLG**

    In this work, we have thoroughly investigated the size-dependent TC of SLG, AB-stacked bilayer graphene (AB-BLG), and twisted bilayer graphene (tBLG) using the Non-Equilibrium Molecular Dynamics (NEMD) direct method. The heat flux in our simulations was calculated by employing Irving-Kirkwood's definition, ensuring that our results are consistent and reliable. A critical assessment of the widely used TWD method for heat flux calculation has also been presented, where we demonstrate that this method significantly overestimates the TC values and should not be relied upon for accurate measurements. Our findings show that the extrapolated bulk TC values obtained from the NEMD direct method are in close agreement with those obtained using the NMD method for the SLG and tBLG systems. The NMD method, known for its sensitivity to system size, serves as an effective validation of our results. Importantly, we adopted the LD

theory-based SED Φ approach, as opposed to the alternative phonon SED Φ' approach. The latter introduces excessive scattering into the relaxation time calculations and has proven to be unreliable. For AB-BLG and the $21.78°$ tBLG systems, our phonon lifetime calculations using the NMD-based approach remained consistent. This consistency contrasts with previous approaches that employed Molecular Dynamics (MD) for obtaining dispersion curves but relied on Density Functional Theory (DFT)-based packages for phonon lifetime calculations. We have shown that this mixed approach can introduce discrepancies, whereas our method maintains coherence between the simulation data and theoretical predictions.

We further investigated the contributions of basic phonon modes to the TC of the graphene samples. Our analysis in the first quadrant of the Brillouin Zones (BZs) along both high-symmetry and non-symmetric directions revealed that, for SLG, the out-of-plane acoustic (ZA), transverse acoustic (TA), and longitudinal acoustic (LA) modes contribute to TC in increasing order along all directions. However, this trend does not hold for the bilayer systems. In the tBLG samples, optical phonon modes dominate TC contributions, while in AB-BLG, both acoustic modes and non-symmetric optical modes have comparable contributions. High-symmetry phonon modes were found to make the most significant contributions to TC across all three graphene systems. A detailed analysis of the phonon group velocities and lifetimes provided further insights: SLG and AB-BLG exhibit similar average group velocities (8.4 and 8.3 km/s, respectively), which are 30% higher than that of tBLG (6.4 km/s). Conversely, AB-BLG and tBLG have comparable average lifetimes (3.9 and 3.8 ps), which are 43% lower than the average phonon lifetime of SLG (6.9 ps). This indicates that the bulk TC, which depends on the product $k \propto v_g^2 \tau$, should be approximately 55% and 28% of the SLG bulk TC for AB-BLG and tBLG, respectively.

Our results using the NMD method gave bulk TC values for AB-BLG and tBLG that are approximately 57% and 30% of the bulk TC of SLG. This strong agreement between theoretical predictions and simulation results underscores the validity of our approach.

- **Phonon properties of xPC-G**

Building on our investigation into graphene systems, we extended our analysis to predict the phonon properties of xPC-G samples with seven different misorientation angles using equilibrium Molecular Dynamics (MD) simulations coupled with the NMD method. This comprehensive study revealed a strong dependence of the TC of xPC-G samples on their misorientation angles, underscoring the critical role of structural orientation in thermal transport.

A key finding from this work is the lack of correlation between the square of the group velocity components along the x and y axes and the phonon lifetimes for all misorientation angles studied. This observation simplifies the calculation of TC, allowing us to represent it in terms of an average phonon mode. Specifically, the group velocity components of this average mode are taken as the root mean square (rms) of the group velocity components of all phonon modes, while the phonon lifetime is the mean of all individual lifetimes. This approach provides a practical framework for estimating TC without the need to consider each phonon mode individually.

To explain the anisotropy observed in TC components for certain misorientation angles, we examined the differences in the rms values of group velocity components along the x and y directions. This anisotropy arises from the structural differences induced by misorientation, highlighting the complex relationship between the atomic arrangement and phonon transport. Interestingly, the density of states (DOS) for all xPC-G samples remained independent of the misorientation angles, suggesting that the overall vibrational spectrum is unaffected, even as the TC components vary significantly. We further analyzed the distribution functions of phonon properties based on the DOS, plotting them as semi-log plots against the phonon normal frequencies. The distributions of the group velocity components followed an exponential decay, while the distribution of phonon lifetimes exhibited a piecewise constant behavior with respect to frequency. This behavior was reflected in the distribution of TC components, which also displayed an exponentially decaying trend with frequency. To quantify these distributions, we provided parameters for the exponential and piecewise constant functions de-

scribing the group velocity components and lifetimes, respectively. Using these parameters, we developed an alternative measure of TC, which we found to be within a $\pm 60\%$ range of the actual TC values, demonstrating the robustness and applicability of our approach.

Finally, we conducted a size-dependent analysis for two specific misorientation angles, $21.78°$ and $32.20°$, calculating their bulk TC components. Our results showed a significant reduction in TC, with decreases ranging from 34% to 62% compared to the bulk TC values of pristine graphene. These findings emphasize the substantial impact of misorientation on thermal transport.

- **Strain and ripple effect on thermal properties of SLG**

Extending our exploration of thermal transport in graphene-based systems, we have conducted an in-depth study on how strain and ripple effects influence the TC of SLG. Our computational investigation started with a small sample size, characterized by minimal out-of-plane fluctuations, ΔZ, which served as a baseline to isolate the effects of strain. Using Normal Mode Decomposition (NMD) analysis, we observed that applying strain, particularly along the zigzag direction, leads to significant alterations in the phonon dispersion relations, most notably impacting the out-of-plane acoustic (ZA) modes. Our analysis revealed that strain causes a shift in the ZA mode dispersion from a quadratic to a linear dependence between frequency and wavevector. This transition is directly linked to a pronounced reduction in the group velocity, v_g, of the ZA modes. The primary reason for this reduction is the weakening of bond stiffness under strain, which inhibits phonon propagation. Additionally, we found that the phonon density of states (PDOS) shifts to lower frequencies as the strain increases, reflecting the altered vibrational landscape of the strained graphene lattice. The NMD analysis provided further insights into the contributions of individual phonon modes to TC. The longitudinal acoustic (LA) modes emerged as the highest contributors, followed by the transverse acoustic (TA) modes, while the transverse optical (TO) and longitudinal optical (LO) modes consistently contributed the least across all levels of strain. Interestingly, our results showed that phonon lifetimes, τ, were relatively insensitive to strain, suggesting that the primary mechanism for TC reduction under

117

strain is the decrease in group velocity rather than changes in phonon lifetimes.

Quantitatively, our findings indicate that TC decreases significantly with strain, with up to a 30% reduction observed between 0-3% strain. Beyond the effects of strain, we also examined the impact of ripples, characterized by ΔZ, which represent out-of-plane deformations. The presence of ripples further amplifies the reduction in TC. Using a GK analysis on a larger sample size with pronounced ΔZ fluctuations, we found that the intrinsic ripple effects, combined with applied strain, resulted in an even greater TC reduction. Specifically, using NMD results for graphene without ripples, we estimated that ripples alone could reduce TC by approximately 61% in larger samples.

- **Thermal transport in 2D FPU-β systems**

  Lastly, motivated by the need to understand the thermal transport properties of two-dimensional anharmonic solids, we studied the FPU-β model. This model is particularly relevant for designing materials for advanced applications where effective heat management is crucial. Our goal was to analyse the underlying mechanisms governing TC behavior in these systems. To achieve this, we employed equilibrium molecular dynamics-based GK method and the NMD method, each providing unique insights into phonon transport.

  Firstly with GK method, we explored the time dependence of TC. The analysis revealed a logarithmic relationship, with TC scaling as $\ln(t)$. This finding underscores the significance of temporal evolution in thermal transport and aligns with prior research, reinforcing the robustness and consistency of our results. The logarithmic dependence highlights how phonon contributions evolve over time, providing a crucial understanding of heat conduction dynamics in anharmonic systems. We then transitioned to the NMD method to delve deeper into the phonon transport properties. We began with a focused analysis of a system size of $N = 28 \times 28 \times 1$. This detailed examination shed light on the behavior of individual phonon modes. Our findings revealed that the average lifetimes of the TA and LA modes were comparable. This behavior can be attributed to the intrinsic symmetry of the FPU-β potential, with our analytical fits capturing these unique phononic characteristics. Expanding our analysis, we also explored the

size-dependent behavior of the TC using the NMD method. The results demonstrated a logarithmic divergence of the TC with increasing system size N. As the system size grew, an increasing number of phonon modes participated in heat transport, resulting in enhanced TC. Remarkably, critical parameters, $v_{g_{rms}}^2$ sharply increases and then becomes constant at 0.5 LJ units with N. Whereas, $< \tau >$ displayed a consistent increase with $ln(N)$, emphasizing the pronounced size effects characteristic of the FPU-β lattice. With the help of a correlation analysis between $v_{g_{rms}}^2$ and $< \tau >$, we were able to argue that the logarithmic dependence of the TC on N can be attributed to the $\bar{\tau}$ with respect to N. Thus, the combined use of the GK and the NMD methods provided a comprehensive understanding of the thermal transport in the FPU-β system. The GK method measured the temporal aspects of TC behavior, while the NMD approach revealed spatial dependencies and detailed phonon properties for different system sizes.

Future scope

In light of the findings from this research, several avenues for future work can be identified:

- Future research should extend the analysis to twisted bilayer graphene (tBLG) systems with various twist angles. This study will help us enhance our understanding of thermal transport mechanisms in tBLGs, which may exhibit unique thermal properties based on their geometric configurations.

- The frequency-dependent distribution functions established for the root mean square (rms) group velocity components and phonon lifetimes for the xPC-G samples can be integrated into multiscale semi-analytical and numerical solutions of the Boltzmann Transport Equation (BTE). This approach will provide a robust framework for the multiscale modeling of TC in polycrystalline graphene materials, facilitating more precise predictions of their thermal behavior.

- The study of the strain and ripple effects plays a critical role in optimizing the thermal properties of graphene. Modulation of these factors could be instrumental in modifying TC for specific applications, thereby methods being developed in future to study the TC of graphene based materials will be more robust if one takes into account the strain and ripple effects.

- We propose to vary the anharmonicity parameter, β, of the FPU-β based lattices of different 2D shapes in order to develop a more general analytical model for TC for such systems. This model will help improve the predictive capabilities for real anharmonic materials, establishing a crucial link between microscopic phonon behavior and macroscopic thermal properties. Such research will significantly contribute to the development of materials with customized thermal properties suitable for diverse technological applications.

References

[1] Alexander A Balandin. Thermal properties of graphene and nanostructured carbon materials. *Nature materials*, 10(8):569–581, 2011.

[2] Denis L Nika and Alexander A Balandin. Phonons and thermal transport in graphene and graphene-based materials. *Reports on Progress in Physics*, 80(3):036502, 2017.

[3] Tabitha A Amollo, Genene T Mola, MSK Kirui, and Vincent O Nyamori. Graphene for thermoelectric applications: prospects and challenges. *Critical Reviews in Solid State and Materials Sciences*, 43(2):133–157, 2018.

[4] Xingyi Huang, Chunyi Zhi, Ying Lin, Hua Bao, Guangning Wu, Pingkai Jiang, and Yiu-Wing Mai. Thermal conductivity of graphene-based polymer nanocomposites. *Materials Science and Engineering: R: Reports*, 142:100577, 2020.

[5] Housseinou Ba, Lai Truong-Phuoc, Thierry Romero, Christophe Sutter, Jean-Mario Nhut, Guy Schlatter, Giuliano Giambastiani, and Cuong Pham-Huu. Lightweight, few-layer graphene composites with improved electro-thermal properties as efficient heating devices for de-icing applications. *Carbon*, 182:655–668, 2021.

[6] Yifeng Fu, Josef Hansson, Ya Liu, Shujing Chen, Abdelhafid Zehri, Majid Kabiri Samani, Nan Wang, Yuxiang Ni, Yan Zhang, Zhi-Bin Zhang, et al. Graphene related materials for thermal management. *2D Materials*, 7(1):012001, 2020.

[7] Farooq Ahmad, Muhammad Zahid, Huma Jamil, Muhammad Ahmed Khan, Shahid Atiq, Mubashira Bibi, Kanwal Shahbaz, Muhammad Adnan, Muhammad Danish, Fazal Rasheed, et al. Advances in graphene-based electrode materials for high-performance supercapacitors: a review. *Journal of Energy Storage*, 72:108731, 2023.

[8] Qingqing Ke and John Wang. Graphene-based materials for supercapacitor electrodes–a review. *Journal of Materiomics*, 2(1):37–54, 2016.

[9] Richard Van Noorden. Production: Beyond sticky tape. *Nature*, 483(7389):S32–S33, 2012.

[10] Peter Debye. Zur theorie der spezifischen wärmen. *Annalen der Physik*, 344(14):789–839, 1912.

[11] Rudolf Peierls. Zur kinetischen theorie der wärmeleitung in kristallen. *Annalen der Physik*, 395(8):1055–1101, 1929.

[12] John M Ziman. *Electrons and phonons: the theory of transport phenomena in solids*. Oxford university press, 2001.

[13] Stefano Lepri, R Livi, and A Politi. Thermal transport in low dimensions. *Lecture notes in physics*, 921:1–37, 2016.

[14] Joseph Ford. The fermi-pasta-ulam problem: paradox turns discovery. *Physics Reports*, 213(5):271–310, 1992.

[15] Anant Raj and Jacob Eapen. Deducing phonon scattering from normal mode excitations. *Scientific reports*, 9(1):7982, 2019.

[16] Leandro M Malard, Marcos Assunção Pimenta, Gene Dresselhaus, and Mildred Spiewak Dresselhaus. Raman spectroscopy in graphene. *Physics reports*, 473(5-6):51–87, 2009.

[17] Vincent E Dorgan, Ashkan Behnam, Hiram J Conley, Kirill I Bolotin, and Eric Pop. High-field electrical and thermal transport in suspended graphene. *Nano letters*, 13(10):4581–4586, 2013.

[18] Alexander A Balandin, Suchismita Ghosh, Wenzhong Bao, Irene Calizo, Desalegne Teweldebrhan, Feng Miao, and Chun Ning Lau. Superior thermal conductivity of single-layer graphene. *Nano letters*, 8(3):902–907, 2008.

[19] Suchismita Ghosh, Irene Calizo, Desalegne Teweldebrhan, Evghenii P Pokatilov, Denis L Nika, Alexander A Balandin, Wenzhong Bao, Feng Miao, and C Ning

Lau. Extremely high thermal conductivity of graphene: Prospects for thermal management applications in nanoelectronic circuits. *Applied Physics Letters*, 92(15), 2008.

[20] Weiwei Cai, Arden L Moore, Yanwu Zhu, Xuesong Li, Shanshan Chen, Li Shi, and Rodney S Ruoff. Thermal transport in suspended and supported monolayer graphene grown by chemical vapor deposition. *Nano letters*, 10(5):1645–1651, 2010.

[21] Luis A Jauregui, Yanan Yue, Anton N Sidorov, Jiuning Hu, Qingkai Yu, Gabriel Lopez, Romaneh Jalilian, Daniel K Benjamin, Derek A Delkd, Wei Wu, et al. Thermal transport in graphene nanostructures: Experiments and simulations. *Ecs Transactions*, 28(5):73, 2010.

[22] Clement Faugeras, Blaise Faugeras, Milan Orlita, Marek Potemski, Rahul R Nair, and AK Geim. Thermal conductivity of graphene in corbino membrane geometry. *ACS nano*, 4(4):1889–1892, 2010.

[23] Jae Hun Seol, Insun Jo, Arden L Moore, Lucas Lindsay, Zachary H Aitken, Michael T Pettes, Xuesong Li, Zhen Yao, Rui Huang, David Broido, et al. Two-dimensional phonon transport in supported graphene. *Science*, 328(5975):213–216, 2010.

[24] Bo Qiu and Xiulin Ruan. Reduction of spectral phonon relaxation times from suspended to supported graphene. *Applied Physics Letters*, 100(19), 2012.

[25] Rui Wu, Rui-Zhi Zhu, Shi-Hui Zhao, Gang Zhang, He Tian, and Tian-Ling Ren. Filling the gap: thermal properties and device applications of graphene. *Science China Information Sciences*, 64:1–17, 2021.

[26] Andrew Z Zhao, Matthew C Wingert, Renkun Chen, and Javier E Garay. Phonon gas model for thermal conductivity of dense, strongly interacting liquids. *Journal of Applied Physics*, 129(23), 2021.

[27] Jacob M Schliesser and Brian F Woodfield. Development of a debye heat capacity model for vibrational modes with a gap in the density of states. *Journal of Physics: Condensed Matter*, 27(28):285402, 2015.

[28] Tae Yun Kim, Cheol-Hwan Park, and Nicola Marzari. The electronic thermal conductivity of graphene. *Nano letters*, 16(4):2439–2443, 2016.

[29] DL Nika, EP Pokatilov, AS Askerov, and Alexander A Balandin. Phonon thermal conduction in graphene: Role of umklapp and edge roughness scattering. *Physical Review B—Condensed Matter and Materials Physics*, 79(15):155413, 2009.

[30] L Lindsay, DA Broido, and Natalio Mingo. Flexural phonons and thermal transport in graphene. *Physical Review B—Condensed Matter and Materials Physics*, 82(11):115427, 2010.

[31] L Lindsay, Wu Li, Jesús Carrete, Natalio Mingo, DA Broido, and TL Reinecke. Phonon thermal transport in strained and unstrained graphene from first principles. *Physical Review B*, 89(15):155426, 2014.

[32] Liang Chen and Satish Kumar. Thermal transport in graphene supported on copper. *Journal of applied physics*, 112(4), 2012.

[33] Andrey Y Serov, Zhun-Yong Ong, and Eric Pop. Effect of grain boundaries on thermal transport in graphene. *Applied Physics Letters*, 102(3), 2013.

[34] Jackie D. Renteria, Denis L. Nika, and Alexander A. Balandin. Graphene thermal properties: Applications in thermal management and energy storage. *Applied Sciences*, 4(4):525–547, 2014.

[35] Dhinakaran Veeman, M. Swapna Sai, V. Rajkumar, M. Ravichandran, and S. Manivannan. Graphene for thermal storage applications: Characterization, simulation and modelling. *Journal of Electronic Materials*, 50:5090–5105, 2021.

[36] M Sang, J Shin, K Kim, and KJ Yu. Electronic and thermal properties of graphene and recent advances in graphene based electronics applications. *Nanomaterials (Basel)*, 9(3):374, 2019.

[37] A.A. Balandin, S. Ghosh, W. Bao, I. Calizo, D. Teweldebrhan, F. Miao, and C.N. Lau. Superior thermal conductivity of single layer graphene. *Nano Letters*, 8:902–907, 2008.

[38] S. Ghosh, I. Calizo, D. Teweldebrhan, E.P. Pokatilov, D.L. Nika, A.A. Balandin, W. Bao, F. Miao, and C.N Lau. Extremely high thermal conductivity in graphene: Prospects for thermal management application in nanoelectronic circuits. *Appl. Phys. Lett.*, 92:151911, 2008.

[39] Weiwei Cai, Arden L. Moore, Yanwu Zhu, Xuesong Li, Shanshan Chen, Li Shi, and Rodney S. Ruoff. Thermal transport in suspended and supported monolayer graphene grown by chemical vapor deposition. *Nano Lett.*, 10(5):1645–1651, 2010.

[40] L Lindsay and DA Broido. Optimized tersoff and brenner empirical potential parameters for lattice dynamics and phonon thermal transport in carbon nanotubes and graphene. *Physical Review B*, 81(20):205441, 2010.

[41] J. H. Irving and J. G. Kirkwood. The statistical mechanical theory of transport processes. iv. the equations of hydrodynamics. *J. Chem. Phys.*, 18(6):817–829, 1950.

[42] R. J. Hardy. Energy-flux operator for a lattice. *Physical Review*, 132(1):168–177, 1963.

[43] Hengji Zhang, Geunsik Lee, and Kyeongjae Cho. Thermal transport in graphene and effects of vacancy defects. *Physical Review B*, 84:115460, 2011.

[44] Y. Y. Zhang, Y. Cheng, Q. X. Pei, C.M. Wang, and Y. Xiang. Thermal conductivity of defective graphene. *Physics Letters A*, 476(47–48):3668–3672, 2012.

[45] Steven J. Stuart, Alan B. Tutein, and Judith A. Harrison. A reactive potential for hydrocarbons with intermolecular interactions. *The Journal of Chemical Physics*, 112(14):6472–6486, 2000.

[46] Ajing Cao. Molecular dynamics simulation study on heat transport in monolayer graphene sheet with various geometries. *Journal of Applied Physics*, 111(8):083528, 2012.

[47] Minkyu Park, Sun-Chul Lee, and Yong-Sung Kim. Length-dependent lattice thermal conductivity of graphene and its macroscopic limit. *Journal of Applied Physics*, 114:053506, 2013.

[48] Amit Singh and Ellad B. Tadmor. Thermal parameter identification for non-fourier heat transfer from molecular dynamics. *Journal of Computational Physics*, 299(18):667–686, 2015.

[49] Amit Singh and Ellad B. Tadmor. Removing artificial kapitza effects from bulk thermal conductivity calculations in direct molecular dynamics. *Journal of Applied Physics*, 117(18):185101, 2015.

[50] Liang Chen and Satish Kumar. Thermal transport in graphene supported on copper. *Journal of Applied Physics*, 112:043502, 2012.

[51] Bo Qiu and Xiulin Ruan. Reduction of spectral phonon relaxation times from suspended to supported graphene. *Applied Physics Letters*, 100(19), 2012.

[52] Bo Qiu, Hua Bao, Xiulin Ruan, Genqiang Zhang, and Yue Wu. Molecular dynamics simulations of lattice thermal conductivity and spectral phonon mean free path of pbte: Bulk and nanostructures. In *Heat Transfer Summer Conference*, volume 44779, pages 659–670. American Society of Mechanical Engineers, 2012.

[53] Ji-Hang Zou, Zhen-Qiang Ye, and Bing-Yang Cao. Phonon thermal properties of graphene from molecular dynamics using different potentials. *The Journal of chemical physics*, 145(13), 2016.

[54] Zherui Han and Xiulin Ruan. Thermal conductivity of monolayer graphene: Convergent and lower than diamond. *Physical Review B*, 108(12):L121412, 2023.

[55] Allan H MacDonald. Bilayer graphene's wicked, twisted road. *Physics*, 12:12, 2019.

[56] Michael Thompson Pettes, Insun Jo, Zhen Yao, and Li Shi. Influence of polymeric residue on the thermal conductivity of suspended bilayer graphene. *Nano Letters*, 11:1195–1200, 2011.

[57] Hongyang Li, Hao Ying, Xiangping Chen, Denis L. Nika, Alexandr I. Cocemasov, Weiwei Cai, Alexander A. Balandin, and Shanshan Chen. Thermal conductivity of twisted bilayer graphene. *Nanoscale*, 6:13402–13408, 2014.

[58] Shuo Han, Xianhua Nie, Shangzhi Gu, Wenyu Liu, Luchen Chen, Hao Ying, Le Wang, Zhihai Cheng, Li Zhao, and Shanshan Chen. Twist-angle-dependent thermal conduction in single-crystalline bilayer graphene. *Applied Physics Letters*, 118(19), 2021.

[59] L. Lindsay, D. A. Broido, and Natalio Mingo. Flexural phonons and thermal transport in multilayer graphene and graphite. *Phys. Rev. B*, 83:235428, 2011.

[60] Dhruv Singh, Jayathi Y. Murthy, and Timothy S. Fisher. Mechanism of thermal conductivity reduction in few-layer graphene. *Journal of Applied Physics*, 110(4), 2011.

[61] Zhiyong Wei, Zhonghua Ni, Kedong Bi, Minhua Chen, and Yunfei Chen. In-plane lattice thermal conductivities of multilayer graphene films. *Carbon*, 49(8):2653–2658, 2011.

[62] J. Tersoff. Empirical interatomic potential for carbon, with applications to amorphous carbon. *Phys Rev Lett*, 61(25):2879–2882, 1988.

[63] Chenyang Li, Bishwajit Debnath, Xiaojian Tan, Shanshan Su, Kui Xu, Supeng Ge, Mahesh R Neupane, and Roger K Lake. Commensurate lattice constant dependent thermal conductivity of misoriented bilayer graphene. *Carbon*, 138:451–457, 2018.

[64] D.W. Brenner, O. A. Shenderova, J. A. Harrison, S. J. Stuart, B. Ni, and S. B. Sinnott. A second-generation reactive empirical bond order (rebo) potential energy expression for hydrocarbons. *J. Phys. Condens. Matter*, 14(4):783, 2002.

[65] LAMMPS website. http://lammps.sandia.gov/.

[66] Xianhua Nie, Li Zhao, Shuai Deng, Yue Zhang, and Zhenyu Du. How interlayer twist angles affect in-plane and cross-plane thermal conduction of multilayer graphene: A non-equilibrium molecular dynamics study. *International Journal of Heat and Mass Transfer*, 137:161–173, 2019.

[67] Wenxiang Liu, Yang Hong, Jingchao Zhang, and Yanan Yue. Anisotropic thermal transport in twisted bilayer graphene. *Phys. Chem. Chem. Phys.*, 24:21722–21728, 2022.

[68] Teng Ma, Zhibo Liu, Jinxiu Wen, Yang Gao, Xibiao Ren, Huanjun Chen, Chuanhong Jin, Xiu-Liang Ma, Ningsheng Xu, and Hui-Ming Cheng. Tailoring the thermal and electrical transport properties of graphene films by grain size engineering. *Nature Communications*, 8:14486, 2017.

[69] Woomin Lee, Kenneth David Kihm, Hong Goo Kim, Seungha Shin, Changhyuk Lee, Jae Sung Park, Sosan Cheon, Oh Myoung Kwon, Gyumin Lim, and Woorim Lee. In-plane thermal conductivity of polycrystalline chemical vapor deposition graphene with controlled grain sizes. *Nano Letters*, 17(4):2361–2366, 2017.

[70] Dongmok Lee, Sanghoon Lee, Byeong-Seon An, Tae-Hoon Kim, Cheol-Woong Yang, Ji Won Suk, and Seunghyun Baik. Dependence of the in-plane thermal conductivity of graphene on grain misorientation. *Chemistry of Materials*, 29(24):10409–10417, 2017.

[71] Akbar Bagri, Sang-Pil Kim, Rodney S Ruoff, and Vivek B Shenoy. Thermal transport across twin grain boundaries in polycrystalline graphene from nonequilibrium molecular dynamics simulations. *Nano letters*, 11(9):3917–3921, 2011.

[72] Bohayra Mortazavi, Markus Potschke, and Gianaurelio Cuniberti. Multiscale modeling of thermal conductivity of polycrystalline graphene sheets. *Nanoscale*, 6:3344–3352, 2014.

[73] Konstanze R Hahn, Claudio Melis, and Luciano Colombo. Thermal transport in nanocrystalline graphene investigated by approach-to-equilibrium molecular dynamics simulations. *Carbon*, 96:429–438, 2016.

[74] HK Liu, Y Lin, and SN Luo. Grain boundary energy and grain size dependences of thermal conductivity of polycrystalline graphene. *The Journal of Physical Chemistry C*, 118(42):24797–24802, 2014.

[75] Ajing Cao and Jianmin Qu. Kapitza conductance of symmetric tilt grain boundaries in graphene. *Journal of Applied Physics*, 111(5), 2012.

[76] YY Zhang, Yuan Cheng, QX Pei, CM Wang, and Yang Xiang. Thermal conductivity of defective graphene. *Physics Letters A*, 376(47-48):3668–3672, 2012.

[77] Khatereh Azizi, Petri Hirvonen, Zheyong Fan, Ari Harju, Ken R Elder, Tapio Ala-Nissila, and S Mehdi Vaez Allaei. Kapitza thermal resistance across individual grain boundaries in graphene. *Carbon*, 125:384–390, 2017.

[78] Andy Fox, Upamanyu Ray, and Teng Li. Thermal conductivity of graphene grain boundaries along arbitrary in-plane directions: A comprehensive molecular dynamics study. *Journal of Applied Physics*, 125(1), 2019.

[79] Te-Huan Liu, Shang-Chin Lee, Chun-Wei Pao, and Chien-Cheng Chang. Anomalous thermal transport along the grain boundaries of bicrystalline graphene nanoribbons from atomistic simulations. *Carbon*, 73:432–442, 2014.

[80] Zhen Tong, Alessandro Pecchia, ChiYung Yam, Traian Dumitrică, and Thomas Frauenheim. Phononic thermal transport along graphene grain boundaries: a hidden vulnerability. *Advanced Science*, 8(18):2101624, 2021.

[81] Kunwar Abhikeern and Amit Singh. A consistent comparison of lattice thermal conductivities and phonon properties of single layer and bilayer graphene systems. *Journal of Applied Physics*, 134(22), 2023.

[82] X Blase, Karin Lin, A Canning, SG Louie, and DC Chrzan. Structure and energy of the 90 partial dislocation in diamond: A combined ab initio and elasticity theory analysis. *Physical Review Letters*, 84(25):5780, 2000.

[83] JM Larkin, JE Turney, AD Massicotte, CH Amon, and AJH McGaughey. Comparison and evaluation of spectral energy methods for predicting phonon properties. *Journal of Computational and Theoretical Nanoscience*, 11(1):249–256, 2014.

[84] Russell George Ross and Olov Sandberg. The thermal conductivity of four solid phases of nh4f, and a comparison with h2o. *Journal of Physics C: Solid State Physics*, 11(4):667, 1978.

[85] Per Andersson, Russel G Ross, and G Backstrom. Thermal resistivity of ice ih near the melting point. *Journal of Physics C: Solid State Physics*, 13(4):L73, 1980.

[86] Somnath Bhowmick and Vijay B Shenoy. Effect of strain on the thermal conductivity of solids. *The Journal of chemical physics*, 125(16), 2006.

[87] RC Picu, T Borca-Tasciuc, and MC Pavel. Strain and size effects on heat transport in nanostructures. *Journal of applied physics*, 93(6):3535–3539, 2003.

[88] Zheyong Fan, Luiz Felipe C Pereira, Petri Hirvonen, Mikko M Ervasti, Ken R Elder, Davide Donadio, Tapio Ala-Nissila, and Ari Harju. Thermal conductivity decomposition in two-dimensional materials: Application to graphene. *Physical Review B*, 95(14):144309, 2017.

[89] SB Cronin, AK Swan, MS Ünlü, BB Goldberg, MS Dresselhaus, and M Tinkham. Measuring the uniaxial strain of individual single-wall carbon nanotubes: resonance raman spectra of atomic-force-microscope modified single-wall nanotubes. *Physical review letters*, 93(16):167401, 2004.

[90] Zhiping Xu and Markus J Buehler. Strain controlled thermomutability of single-walled carbon nanotubes. *Nanotechnology*, 20(18):185701, 2009.

[91] Xiaobo Li, Kurt Maute, Martin L Dunn, and Ronggui Yang. Strain effects on the thermal conductivity of nanostructures. *Physical Review B—Condensed Matter and Materials Physics*, 81(24):245318, 2010.

[92] Jannik C Meyer, Andre K Geim, Mikhail I Katsnelson, Konstantin S Novoselov, Tim J Booth, and Siegmar Roth. The structure of suspended graphene sheets. *Nature*, 446(7131):60–63, 2007.

[93] Shikai Deng and Vikas Berry. Wrinkled, rippled and crumpled graphene: an overview of formation mechanism, electronic properties, and applications. *Materials Today*, 19(4):197–212, 2016.

[94] Ke Xu, Peigen Cao, and James R Heath. Scanning tunneling microscopy characterization of the electrical properties of wrinkles in exfoliated graphene monolayers. *Nano letters*, 9(12):4446–4451, 2009.

[95] Steven W Cranford and Markus J Buehler. Packing efficiency and accessible surface area of crumpled graphene. *Physical Review B—Condensed Matter and Materials Physics*, 84(20):205451, 2011.

[96] Large-Area Graphene. Multifunctionality and control of the crumpling and unfolding of large-area graphene. *nature*, 2013.

[97] Chun-Chung Chen, Wenzhong Bao, Jesse Theiss, Chris Dames, Chun Ning Lau, and Stephen B Cronin. Raman spectroscopy of ripple formation in suspended graphene. *Nano letters*, 9(12):4172–4176, 2009.

[98] U Bangert, MH Gass, AL Bleloch, RR Nair, and AK Geim. Manifestation of ripples in free-standing graphene in lattice images obtained in an aberration-corrected scanning transmission electron microscope, 2009.

[99] Recep Zan, Chris Muryn, Ursel Bangert, Philip Mattocks, Paul Wincott, David Vaughan, Xuesong Li, Luigi Colombo, Rodney S Ruoff, Bruce Hamilton, et al. Scanning tunnelling microscopy of suspended graphene. *Nanoscale*, 4(10):3065–3068, 2012.

[100] Annalisa Fasolino, JH Los, and Mikhail I Katsnelson. Intrinsic ripples in graphene. *Nature materials*, 6(11):858–861, 2007.

[101] Kaito Nakagawa, Kazuo Satoh, Shuichi Murakami, Kuniharu Takei, Seiji Akita, and Takayuki Arie. Controlling the thermal conductivity of multilayer graphene by strain. *Scientific Reports*, 11(1):19533, 2021.

[102] Youdi Kuang, Lucas Lindsay, Sanqiang Shi, Xinjiang Wang, and Baoling Huang. Thermal conductivity of graphene mediated by strain and size. *International Journal of Heat and Mass Transfer*, 101:772–778, 2016.

[103] Ming Guo, Yicheng Qian, Han Qi, Kedong Bi, and Yunfei Chen. Experimental measurements on the thermal conductivity of strained monolayer graphene. *Carbon*, 157:185–190, 2020.

[104] Yingtao Wang and Xian Zhang. Thermal transport in graphene under large mechanical strains. *Journal of Applied Physics*, 136(7), 2024.

[105] Wenzhong Bao, Feng Miao, Zhen Chen, Hang Zhang, Wanyoung Jang, Chris Dames, and Chun Ning Lau. Controlled ripple texturing of suspended graphene and ultrathin graphite membranes. *Nature nanotechnology*, 4(9):562–566, 2009.

[106] Ning Wei, Lanqing Xu, Hui-Qiong Wang, and Jin-Cheng Zheng. Strain engineering of thermal conductivity in graphene sheets and nanoribbons: a demonstration of magic flexibility. *Nanotechnology*, 22(10):105705, 2011.

[107] Jianhui Wang, HA Fertig, Ganpathy Murthy, and L Brey. Excitonic effects in two-dimensional massless dirac fermions. *Physical Review B—Condensed Matter and Materials Physics*, 83(3):035404, 2011.

[108] Julia A. Baimova, Sergey V. Dmitriev, Kun Zhou, and Alexander V. Savin. Unidirectional ripples in strained graphene nanoribbons with clamped edges at zero and finite temperatures. *Phys. Rev. B*, 86:035427, Jul 2012.

[109] Sergey V. Dmitriev, Julia A. Baimova, Alexander V. Savin, and Yuri S. Kivshar. Ultimate strength, ripples, sound velocities, and density of phonon states of strained graphene. *Computational Materials Science*, 53(1):194–203, 2012.

[110] Jianwei Zhang, Xiaodong He, Lin Yang, Guoqiang Wu, Jianjun Sha, Chengyu Hou, Cunlu Yin, Acheng Pan, Zhongzhou Li, and Yubai Liu. Effect of tensile strain on thermal conductivity in monolayer graphene nanoribbons: A molecular dynamics study. *Sensors*, 13(7):9388–9395, 2013.

[111] Byoung Seo Lee and Joon Sik Lee. Thermal conductivity reduction in graphene with silicon impurity. *Applied Physics A*, 121:1193–1202, 2015.

[112] Konstanze R Hahn, Claudio Melis, and Luciano Colombo. Structural, vibrational, and thermal properties of nanocrystalline graphene in atomistic simulations. *The Journal of Physical Chemistry C*, 120(5):3026–3035, 2016.

[113] Kyeong Hyun Park and Umberto Ravaioli. Limited thermal transport in rippled graphene induced by bi-axial strain for thermoelectric applications. *Journal of Applied Physics*, 122(2), 2017.

[114] Daniel N Payton III, Marvin Rich, and William M Visscher. Lattice thermal conductivity in disordered harmonic and anharmonic crystal models. *Physical Review*, 160(3):706, 1967.

[115] M Rich, WM Visscher, and DN Payton III. Thermal conductivity of a two-dimensional two-branch lattice. *Physical Review A*, 4(4):1682, 1971.

[116] Raymond D Mountain and Rosemary A MacDonald. Thermal conductivity of crystals: A molecular-dynamics study of heat flow in a two-dimensional crystal. *Physical Review B*, 28(6):3022, 1983.

[117] Reinhard HH Poetzsch and Harald Böttger. Interplay of disorder and anharmonicity in heat conduction: molecular-dynamics study. *Physical Review B*, 50(21):15757, 1994.

[118] RHH Poetzsch and H Böttger. Non-diffusive heat transport and chaos in nonlinear dielectric lattices. *Journal of Physics: Condensed Matter*, 10(5):943, 1998.

[119] J Michalski. Thermal conductivity of amorphous solids above the plateau: Molecular-dynamics study. *Physical Review B*, 45(13):7054, 1992.

[120] Andrea Lippi and Roberto Livi. Heat conduction in two-dimensional nonlinear lattices. *Journal of Statistical Physics*, 100(5):1147–1172, 2000.

[121] L Yang, P Grassberger, and B Hu. Dimensional crossover of heat conduction in low dimensions. *Physical Review E—Statistical, Nonlinear, and Soft Matter Physics*, 74(6):062101, 2006.

[122] Lei Yang. Finite heat conduction in a 2d disorder lattice. *Physical review letters*, 88(9):094301, 2002.

[123] Stefano Lepri, Roberto Livi, and Antonio Politi. Studies of thermal conductivity in fermi–pasta–ulam-like lattices. *Chaos: An Interdisciplinary Journal of Nonlinear Science*, 15(1), 2005.

[124] Peter Grassberger and Lei Yang. Heat conduction in low dimensions: from fermi-pasta-ulam chains to single-walled nanotubes. *arXiv preprint cond-mat/0204247*, 2002.

[125] E Atlee Jackson and Antonis D Mistriotis. Thermal conductivity of one-and two-dimensional lattices. *Journal of Physics: Condensed Matter*, 1(7):1223, 1989.

[126] Lik Wee Lee and Abhishek Dhar. Heat conduction in a two-dimensional harmonic crystal with disorder. *Physical review letters*, 95(9):094302, 2005.

[127] Yue Liu and Dahai He. Approach to phonon relaxation time and mean free path in nonlinear lattices. *Chinese Physics Letters*, 38(4):044401, 2021.

[128] Abhishek Dhar. Heat transport in low-dimensional systems. *Advances in Physics*, 57(5):457–537, 2008.

[129] Andrey Pereverzev. Fermi-pasta-ulam β lattice: Peierls equation and anomalous heat conductivity. *Physical review E*, 68(5):056124, 2003.

[130] Lubo Xu and Lei Wang. Dispersion and absorption in one-dimensional nonlinear lattices: A resonance phonon approach. *Physical Review E*, 94(3):030101, 2016.

[131] Lubo Xu and Lei Wang. Resonance phonon approach to phonon relaxation time and mean free path in one-dimensional nonlinear lattices. *Physical Review E*, 95(4):042138, 2017.

[132] Shiqian Hu, Jie Chen, Nuo Yang, and Baowen Li. Thermal transport in graphene with defect and doping: phonon modes analysis. *Carbon*, 116:139–144, 2017.

[133] Yue Liu and Dahai He. Anomalous interfacial temperature profile induced by phonon localization. *Physical Review E*, 96(6):062119, 2017.

[134] Jun Fang, Xin Qian, CY Zhao, Baowen Li, and Xiaokun Gu. Monitoring anharmonic phonon transport across interfaces in one-dimensional lattice chains. *Physical review E*, 101(2):022133, 2020.

[135] Dan Frenkel and Berend Smit. *Understanding Molecular Simulation*. Academic Press, San Diego, CA, US, 2nd edition, 2002.

[136] J. Jellinek and D. H. Li. Separation of the energy of overall rotation in any N-body system. *Phys. Rev. Lett.*, 62(3):241–244, 1989.

[137] Patrick K. Schelling, Simon R. Phillpot, and Pawel Keblinski. Comparison of atomic-level simulation methods for computing thermal conductivity. *Phys. Rev. B*, 65:144306, Apr 2002.

[138] J.M. Ziman. *Electrons and Phonons: The Theory of Transport Phenomena in Solids*. International series of monographs on physics. Clarendon Press, 1960.

[139] Martin T. Dove. *Introduction to Lattice Dynamics*. Cambridge Topics in Mineral Physics and Chemistry. Cambridge University Press, 1993.

[140] Julian D. Gale and Andrew L. Rohl. The general utility lattice program (gulp). *Molecular Simulation*, 29(5):291–341, 2003.

[141] Alan J. H. McGaughey and Jason Larkin. Predicting phonon properties from equilibrium molecular dynamics simulations. *Annual Review of Heat Transfer*, 17:49–87, 2014.

[142] Amit Singh and Ellad B. Tadmor. Thermal parameter identification for non-fourier heat transfer from molecular dynamics. *Journal of Computational Physics*, 299:667–686, 2015.

[143] Jun Kang and Lin-Wang Wang. First-principles green-kubo method for thermal conductivity calculations. *Physical Review B*, 96(2):020302, 2017.

[144] Anthony JC Ladd, Bill Moran, and William G Hoover. Lattice thermal conductivity: A comparison of molecular dynamics and anharmonic lattice dynamics. *Physical Review B*, 34(8):5058, 1986.

[145] JE Turney, ES Landry, AJH McGaughey, and CH Amon. Predicting phonon properties and thermal conductivity from anharmonic lattice dynamics calculations and molecular dynamics simulations. *Physical Review B*, 79(6):064301, 2009.

[146] Alan JH McGaughey and M Kaviany. Quantitative validation of the boltzmann transport equation phonon thermal conductivity model under the single-mode relaxation time approximation. *Physical Review B*, 69(9):094303, 2004.

[147] Jason M Larkin, Alexandre D Massicotte, Joseph E Turney, Alan JH McGaughey, and Cristina H Amon. Comparison of spectral energy density methods for predicting phonon properties. In *International Conference on Micro/Nanoscale Heat Transfer*, volume 54778, pages 753–759. American Society of Mechanical Engineers, 2012.

[148] Kazuyuki Uchida, Shinnosuke Furuya, Jun-Ichi Iwata, and Atsushi Oshiyama. Atomic corrugation and electron localization due to moiré patterns in twisted bilayer graphenes. *Physical Review B*, 90(15):155451, 2014.

[149] Steve Plimpton. Fast parallel algorithms for short-range molecular dynamics. *Journal of computational physics*, 117(1):1–19, 1995.

[150] F. X. Alvarez and D. Jou. Memory and nonlocal effects in heat transport: From diffusive to ballistic regimes. *Applied Physics Letters*, 90(8):083109, 02 2007.

[151] Zhiyong Wei, Juekuan Yang, Kedong Bi, and Yunfei Chen. Mode dependent lattice thermal conductivity of single layer graphene. *Journal of Applied Physics*, 116(15):153503, 2014.

[152] Alexandr I Cocemasov, Denis L Nika, and Alexander A Balandin. Phonons in twisted bilayer graphene. *Physical Review B*, 88(3):035428, 2013.

[153] Dhruv Singh, Jayathi Y Murthy, and Timothy S Fisher. Mechanism of thermal conductivity reduction in few-layer graphene. *Journal of Applied Physics*, 110(4):044317, 2011.

[154] Denis L Nika, Alexandr I Cocemasov, and Alexander A Balandin. Specific heat of twisted bilayer graphene: Engineering phonons by atomic plane rotations. *Applied Physics Letters*, 105(3), 2014.

[155] Hongyang Li, Hao Ying, Xiangping Chen, Denis L Nika, Alexandr I Cocemasov, Weiwei Cai, Alexander A Balandin, and Shanshan Chen. Thermal conductivity of twisted bilayer graphene. *Nanoscale*, 6(22):13402–13408, 2014.

[156] Alan JH McGaughey and Jason M Larkin. Predicting phonon properties from equilibrium molecular dynamics simulations. *Annual review of heat transfer*, 17, 2014.

[157] Tianli Feng and Xiulin Ruan. Four-phonon scattering reduces intrinsic thermal conductivity of graphene and the contributions from flexural phonons. *Phys. Rev. B*, 97:045202, 2018.

[158] Colin Ophus, Ashivni Shekhawat, Haider Rasool, and Alex Zettl. Large-scale experimental and theoretical study of graphene grain boundary structures. *Physical Review B*, 92(20):205402, 2015.

[159] Junfeng Zhang and Jijun Zhao. Structures and electronic properties of symmetric and nonsymmetric graphene grain boundaries. *Carbon*, 55:151–159, 2013.

[160] Oleg V Yazyev and Steven G Louie. Topological defects in graphene: Dislocations and grain boundaries. *Physical Review B*, 81(19):195420, 2010.

[161] WA Diery, Elie A Moujaes, and RW Nunes. Nature of localized phonon modes of tilt grain boundaries in graphene. *Carbon*, 140:250–258, 2018.

[162] Donald W Brenner, Olga A Shenderova, Judith A Harrison, Steven J Stuart, Boris Ni, and Susan B Sinnott. A second-generation reactive empirical bond order (rebo) potential energy expression for hydrocarbons. *Journal of Physics: Condensed Matter*, 14(4):783, 2002.

[163] Chengyun Hua and Austin J. Minnich. Semi-analytical solution to the frequency-dependent boltzmann transport equation for cross-plane heat conduction in thin films. *Journal of Applied Physics*, 117(22), 2015.

[164] Amit Singh Abhishek Kumar, Kunwar Abhikeern. Effect of ripples and curvatures on thermal conductivity of graphene with grain boundaries. *Sent to Journal of Applied Physics*, 2024. Draft available upon request.

[165] Kento Tada, Takashi Funatani, Satoru Konabe, Kenji Sasaoka, Matsuto Ogawa, Satofumi Souma, and Takahiro Yamamoto. Modulations of thermal properties of graphene by strain-induced phonon engineering. *Japanese Journal of Applied Physics*, 56(2):025102, 2017.

[166] Kyeong Hyun Park and Umberto Ravaioli. Limited thermal transport in rippled graphene induced by bi-axial strain for thermoelectric applications. *Journal of Applied Physics*, 122(2), 2017.

[167] Ryogo Kubo, Morikazu Toda, and Natsuki Hashitsume. *Statistical physics II: nonequilibrium statistical mechanics*, volume 31. Springer Science & Business Media, 2012.

[168] Giancarlo Benettin. Time scale for energy equipartition in a two-dimensional fpu model. *Chaos: An Interdisciplinary Journal of Nonlinear Science*, 15(1), 2005.

This page was intentionally left blank.

List of Publications and Conferences

International Journals

1. **Abhikeern Kunwar,** Singh Amit, 2023, "A consistent comparison of lattice thermal conductivities and phonon properties of single layer and bilayer graphene systems", *J. Appl. Phys. 134, 224305*

2. **Abhikeern Kunwar,** Singh Amit, 2024, "Lattice thermal conductivity and phonon properties of polycrystalline graphene", (*under review*)

3. **Abhikeern Kunwar,** Singh Amit, 2024, "FPU models: Study of its anomalous behaviour and thermal properties of 2D polygonal structures", (*in process*)

4. Meiksin, J., **Abhikeern, K.,** Antimirova, E. et al., Materials Research Society celebrates 50th anniversary at 2023 MRS Spring Meeting & Exhibit. *MRS Bulletin*, 48 (9), 947-954.

5. Kumar Abhishek, **Abhikeern Kunwar,** Singh Amit, "Study of thermal properties due to strain and wrinkling effects on single layer graphene with grain boundaries", (*under review*)

6. Jangid Komal, **Abhikeern Kunwar,** Singh Amit, "Advanced Models for Heat Transfer Across 2D Material Interfaces: ML and Numerical Approaches", (*in process*)

International Conferences

1. *Oral* and *Poster Presentation* organized by 17th U. S. National Congress on Computational Mechanics held in Albuquerque, New Mexico, USA in July 2023 titled

"Multiscale modeling of unsteady non-equilibrium Boltzmann transport equation with FEM", **Kunwar Abhikeern**, Amit Singh and chaired by Veruska Malave

2. *Poster Presentation* at Materials Research Society, Spring Conference, held in San Francisco in April 2023 titled "Multiscale modeling of unsteady non-equilibrium Boltzmann transport equation with FEM", **Kunwar Abhikeern**, Amit Singh

3. *Oral Presentation* titled "Study of Unsteady Thermal Transport in Single Layer Graphene with NMD approach" organized by Virtual Conference on Thermo-electrics (VCT),Japan 2020 chaired by Prof. Titas Dasgupta held virtually, **Kunwar Abhikeern**, Amit Singh

Acknowledgments

I am very grateful to my advisor, Prof. Amit Singh. His unwavering guidance and invaluable insights throughout my research journey have been monumental. With his in-depth knowledge, clear and sharp analytical prowess, he stands as an epitome of research excellence. His dedication to the advancement and well-being of his students is exceptional. It has been a privilege to be mentored by someone who invested his time wholeheartedly in my research with clarity and promptly refined my write-ups.

I wish to extend my heartfelt appreciation to my Annual Progress Committee members - Prof. Titas Dasgupta, Prof. Ankit Jain and Prof. Aftab Alam. Their invaluable feedback and expert perspectives undeniably enriched my research.

My gratitude extends to my peers, Abhishek and Komal, for their company and constructive feedbacks. My journey at the IIT campus was made memorable thanks to friends Dr. Rashmi, Aarti, Priya, Chetana, Upendra, Shivam, Manoj, Anil, Swapnil, Anshul, Ajay, Pankaj, Deepak, Rishabh, and Aditya - I cherish every moment spent with them. I express my heartfelt gratitude to Dr. Rashmi in particular, who has been a constant companion and source of support throughout my journey until the completion of my Ph.D. Her unwavering presence has been invaluable.

I would like to convey my gratitude to the IRCC, IIT Bombay, for their financial support, ensuring that I could pursue my research without placing a financial strain on my family.

In conclusion, my deepest thanks go to my family - the cornerstone of my life. To my dear parents and my brother, your belief and patience in me has been my guiding anchor. My achievements are as much theirs as they are mine.

Kunwar Abhikeern

November 08, 2024

IIT Bombay